MICROMECHANICS BASED FAILURE ANALYSIS OF HETEROGENEOUS MATERIALS

A Dissertation

Submitted to the Faculty

of

Purdue University

by

Hamsasew M. Sertse

In Partial Fulfillment of the

Requirements for the Degree

of

Doctor of Philosophy

December 2017

Purdue University

West Lafayette, Indiana

THE PURDUE UNIVERSITY GRADUATE SCHOOL
STATEMENT OF DISSERTATION APPROVAL

Dr. Wenbin Yu, Chair

School of Aeronautics and Astronautics

Dr. R. B. Pipes

School of Aeronautics and Astronautics

Dr. Pablo D. Zavattieri

School of Aeronautics and Astronautics

Dr. Michael D. Sangid

School of Aeronautics and Astronautics

Approved by:

Dr. Weinong Wayne Chen

Head of the School Graduate Program

I dedicated this work to my wife Sophia Teka and my daughters Nolawit and Amanawit Moges.

ACKNOWLEDGMENTS

First and for most, I would like to thank almighty God for energy and patience He provided me during all my studies. I also would like to take this opportunity to extend my heartfelt thanks to my advisor Professor Wenbin Yu for his encouragement, help and also constructive comments and suggestions during the course of my study and also preparation of this work. I also highly appreciate the external examiners of this work, Distinguished Professor R. Bryon Pipes, Professor Pablo D. Zavattieri, and Professor Michael Sangid, for their willingness to review my work. Special thanks goes to my wife Sophia Teka, and my twin daughters Nolawit Moges and Amanagwit Moges for the support and love they all offered me during my study. Without their support, it is impossible to be at this point right now. Thanks to my mother, brothers, sister and sister-in-law Ayida, and Amarech Sertse for all their thoughts for me and my family. I am also very thankful for my mother-in-law, recently passed away, and Zewdalem Dinkayehu for their endless support and prayers to my family. Last but not least, I love to express my thanks for all colleagues in multiscale structural mechanics research group for helpful discussions and unforgettable time we spent together.

TABLE OF CONTENTS

LIST OF TABLES

Table Page

LIST OF FIGURES

Figure Page

ABSTRACT

Sertse, Hamsasew M. PhD, Purdue University, December 2017. Micromechanics Based Failure Analysis of Heterogeneous Materials. Major Professor: Wenbin Yu.

In recent decades, heterogeneous materials are extensively used in various industries such as aerospace, defense, automotive and others due to their desirable specific properties and excellent capability of accumulating damage. Despite their wide use, there are numerous challenges associated with the application of these materials. One of the main challenges is lack of accurate tools to predict the initiation, progression and final failure of these materials under various thermomechanical loading conditions. Although failure is usually treated at the macro and meso-scale level, the initiation and growth of failure is a complex phenomena across multiple scales.

The objective of this work is to enable the mechanics of structure genome (MSG) and its companion code SwiftComp to analyze the initial failure (also called static failure), progressive failure, and fatigue failure of heterogeneous materials using micromechanics approach. The initial failure is evaluated at each numerical integration point using pointwise and nonlocal approach for each constituent of the heterogeneous materials. The effects of imperfect interfaces among constituents of heterogeneous materials are also investigated using a linear traction-displacement model. Moreover, the progressive and fatigue damage analyses are conducted using continuum damage mechanics (CDM) approach. The various failure criteria are also applied at a material point to analyze progressive damage in each constituent. The constitutive equation of a damaged material is formulated based on a consistent irreversible thermodynamics approach. The overall tangent modulus of uncoupled elastoplastic damage for negligible back stress effect is derived. The initiation of

plasticity and damage in each constituent is evaluated at each numerical integration point using a nonlocal approach. The accumulated plastic strain and anisotropic damage evolution variables are iteratively solved using an incremental algorithm. The damage analyses are performed for both brittle failure/high cycle fatigue (HCF) for negligible plastic strain and ductile failure/low cycle fatigue (LCF) for large plastic strain.

The proposed approach is incorporated in SwiftComp and used to predict the initial failure envelope, stress-strain curve for various loading conditions, and fatigue life of heterogeneous materials. The combined effects of strain hardening and progressive fatigue damage on the effective properties of heterogeneous materials are also studied. The capability of the current approach is validated using several representative examples of heterogeneous materials including binary composites, continuous fiber-reinforced composites, particle-reinforced composites, discontinuous fiber-reinforced composites, and woven composites. The predictions of MSG are also compared with the predictions obtained using various micromechanics approaches such as Generalized Methods of Cells (GMC), Mori-Tanaka (MT), and Double Inclusions (DI) and Representative Volume Element (RVE) Analysis (called as 3-dimensional finite element analysis (3D FEA) in this document).

This study demonstrates that a micromechanics based failure analysis has a great potential to rigorously and more accurately analyze initiation and progression of damage in heterogeneous materials. However, this approach requires material properties specific to damage analysis, which are needed to be independently calibrated for each constituent.

1. INTRODUCTION

1.1 Background and Motivation

In recent decades, heterogeneous materials are extensively used in various industries such as aerospace, defense, automotive and others due to their desirable specific effective properties and excellent capability of accumulating damage. Despite their wide use, there are numerous challenges associated with the application of these materials. One of the main challenges is lack of accurate tools to predict the initiation, progression and final failure of heterogeneous materials under various loading conditions.

Although failure is usually treated at the macro and meso-scale level, the initiation and growth of failure is a complex phenomenon significantly affected by local fields. During failure, materials locally undergo process of nucleation, coalescence and growth of micro cavity induced by large plastic deformation particularly for ductile materials. And materials can also experience an abrupt failure right after the inception of plastic strain, which is commonly observed in brittle materials. Various deterministic and probabilistic failure theories have been proposed and widely used to analyze failure of materials. However, there is a lack of a unified failure theory that consistently and accurately estimates the strength of materials for various loading conditions and different material behaviours.

In heterogeneous materials, failure is a multi-scale complex phenomenon which results from the interactions among various contributing factors such as the properties of the matrix, the fiber, the matrix-fiber interface, and the fiber volume fraction, and the loading conditions. The failure strength is also significantly influenced by the conditions of the interface among constituents of heterogeneous materials.

Generally speaking, the failure of a heterogeneous material is usually modeled using both macromechanical and micromechanical approaches. In a macromechanical approach, failure analyses are performed based on averaged/smeared properties of the heterogeneous materials. In this approach, for example, for composite laminates, each lamina may be treated as a pseudo homogeneous orthotropic material. Failure analysis using this approach is relatively simple for numerical analysis, but it can not accurately predict the failure strength of heterogeneous materials at the constituent level due to its inability to account for the disturbance of local fields. On the other hand, in a micromechanical approach, failure is analyzed based on the local fields in each constituent of the heterogeneous materials. In this case, failure may be analyzed based on the averaged local fields or based on the pointwise local fields in each constituent.

Various failure criteria have been proposed and widely used for homogeneous materials. It is usually noticed that the proposed failure criteria are modified to estimate failure strength of composite laminates. These modifications definitely add limitations or unnecessary assumptions to the failure criteria [1]. Moreover, the number of material constants required to perform the analysis may also increase due to the assumptions. However, all of material constants may not be accurately and uniquely obtained. Consequently, this can result in inconsistent prediction of the failure strength of the composite laminates. Recently, it is shown that predictive capabilities of various proposed failure theories are not able to sufficiently and consistently estimate the failure strength of continuous fiber-reinforced composites as reported in the world wide failure exercise (WWFE) [2, 3].

In the present work, failure of heterogeneous materials is analyzed based on the micromechanics approach using mechanics of structure genome (MSG) and its companion code SwiftComp. SwiftComp is a general-purpose multi-scale constitutive modeling code for composites which provides unified modeling for 1D (beams), 2D (plates/shells), or 3D composite structures. This is accomplished using the concept of structure genome (SG) that unifies structural mechanics and micromechanics. A

SG is the smallest mathematical building block (or a cell in biological contexts) of the structure containing many such building blocks. SwiftComp demonstrated excellent capability both in predicting effective properties and local fields for several examples of heterogeneous materials [4, 5]. Moreover, as MSG is a semi-analytical, it converses faster than 3D FEA. This makes MSG a more efficient approach. Thus, SwiftComp is a natural choice to perform failure analysis of heterogeneous materials using its accurate predictions of local fields.

The novelty of the current failure analysis approach is that it is not specific to any particular type of heterogeneous materials. There are no any further assumptions to be made to modify the failure criteria for a specific type of heterogeneous material. The number of strength constants are fewer and similar to the one used for constituents. Moreover, during analysis, the strength constants which are calibrated for one type of heterogeneous material can be used to analyze the failure in other types of heterogeneous materials with the same constituents. This analysis definitely helps to produce more reasonable failure predictions that may be used for design and analysis of composite structures.

1.2 Goal and Objectives of the Current Work

The goal of this work is to enable the MSG and its companion code SwiftComp to analyze the initiation, progression, and final failure of heterogeneous materials using pointwise and nonlocal micromechanics approach.

The specific objectives of the current work are to enable the MSG to estimate:

- Initial failure failure using various failure criteria.
- Progressive failure for various loading conditions.
- Fatigue failure and life prediction, and residual stiffness both for ductile and brittle heterogeneous materials.

- The effect of imperfect interface on the failure strength and effective properties of heterogeneous materials.

These analyses are conducted using the nonlocal approach, i.e., averaging the pointwise local fields within its neighborhood over a specific characteristic length. The progressive damage and fatigue life predictions are analyzed using continuum damage mechanics. Various failure criteria are also used to analyze the initiation of failure at the material point and also investigate the progressive damage in each constituent of heterogeneous materials.

2. LITERATURE REVIEW

2.1 Failure Theories and Criteria

2.1.1 Failure Theories

Numerous researchers have proposed various failure theories to analyze the complex failure behavior of materials at different levels of abstractions. These failure theories can be categorized as deterministic and probabilistic failure theories.

I. Deterministic Failure Theories

These theories are obtained using certain phenomenological constitutive equations. These can be energy based failure constitutive equations and generalized failure constitutive equations. In energy based approach, it is usually postulated that failure of materials occurs when the distortion and/or dilatation energies reach the critical value. Distortion energy is responsible for the change of shape of material while dilatation energy represents the change of volume of materials under any specified loading conditions. The energy in the material is casted in the form of constitutive equation to analyze initiation and/or final failure of materials. The most common constitutive equation based on the dilatation and distortional energies [6] may be expressed using polynomial expansion of invariants of strain/stress tensor as

$$\phi = \alpha I_1 + \beta I_1^2 + \gamma J_2 + .. \tag{2.1}$$

where α, β, and γ denote material dependent constants, I_1 denotes the first invariant of stress tensor and J_2 denotes the second invariant of the deviatoric stress tensor.

Micromechanics based constitutive models have been also widely used to model the growth and coalescence of voids in ductile materials [7–10]. These models are used

to perform failure analysis for specific finite void sizes and shapes. These models are not applicable for complex void shapes and cracks, and also for materials without voids or defects. On the other hand, the failure of ductile materials is also extensively analyzed using thermodynamic free energy. This approach is also used to predict the process of nucleation, coalescence and growth of micro cavity which is formulated based on a consistent thermodynamic framework called continuum damage mechanics [11–16].

For composite laminates, a general and comprehensive failure theory was proposed by Goldenblat and Kopnov [17]. In this approach, there is no a priori assumption made unlike many other failure criteria. However, there are certain principles adopted which are merely based on the nature of the phenomenon of failure. The generalized failure constitutive equation for the stress space can be expressed as

$$(\Sigma\Pi_{ik}\sigma_{ik})^{\alpha} + (\Sigma\Pi_{pqnm}\sigma_{pq}\sigma_{mn})^{\beta} + (\Sigma\Pi_{rstlnm}\sigma_{rs}\sigma_{tl}\sigma_{nm})^{\gamma} + ... \leq 1 \qquad (2.2)$$

where α, β, and γ denote material dependent constants, Π_{ik}, Π_{pqnm}, and Π_{rstlnm} denote components of symmetric second, fourth, and six-order strength tensors, σ_{ik} denote the components of the second-order stress tensor. In this theory, it was shown that the shear strength of the composite laminate is dependent on direction (sign) of the shear load which is observed to be consistent with experimental observation [17]. The main drawback of this approach is that it requires a large number of strength constants, which may not be easily quantifiable.

II. Probabilistic Failure Theories

Failure may be modeled using various probability functions among them the most common one is the Weibull's probabilistic approach [18–21]. This approach, usually referred as the weakest link theory, postulates that the failure strength of the structure is governed by the weakest point in the structure. This implies that larger structures are more susceptible to failure compared with smaller structures at the same stress level. This is mainly due to a higher probability of flaw in the larger structures. This

approach is extended to capture the location of failure and also to analyze the effect of loading history on the failure strength of composite laminates [22].

2.1.2 Failure Criteria

There are many failure criteria in the literature. Almost all of them are derived or modified from the two basic failure theories discussed in the previous section. Some of the criteria may require single constant while others may require up to 27 strength constants to analyze failure. The most common and widely used failure criteria are: Von Mises, Tresca, maximum principal stress/strain, Tsai-Hill, and Tsai-Wu.

I. Von Mises Failure Criterion

This failure criterion uses critical distortion energy to predict the failure of ductile isotropic materials. This criterion also gives smooth failure surface/envelope. It is derived from Eq. (2.1) by assuming the tensile and compressive strength of the material to be equal ($Y_T = Y_C$), and the allowable shear stress $Y_s = Y_T/\sqrt{3}$. By assuming that hydrostatic pressure does not cause failure, $\alpha = \beta = 0$, and $\gamma = 1$ in Eq. (2.1), the failure function of Von Mises criterion can be described as

$$f = \frac{1}{2}\left[(\sigma_{11} - \sigma_{22})^2 + (\sigma_{22} - \sigma_{33})^2 + (\sigma_{33} - \sigma_{11})^2 + 6(\sigma_{12}^2 + \sigma_{23}^2 + \sigma_{13}^2)\right] - Y^2 \quad (2.3)$$

where σ_{ij} denote multiaxial stresses $i, j = 1, 2, 3$ and σ_{ij}=σ_{ji}, Y is the failure limit of the material. The most general form of this criterion is also proposed by Hill [23] for ductile materials based on the directional dependency of yielding of materials.

II. Tresca Failure Criterion

Tresca criterion, also known as the maximum shear stress criterion, is based on the maximum shear stress in the material: the material fails when the maximum shear

stress of a material point exceeds the shear strength of the material. The failure function for the maximum shear stress criterion may be defined by [24]

$$f = \tau_{max} - \frac{Y}{2}, \tag{2.4}$$

where τ_{max} is the maximum shear stress, and $\frac{Y}{2} = Y_S$ denotes the shear strength or the failure limit of the material.

III. Maximum Principal Stress/Strain Failure Criteria

The maximum principal stress criterion, usually known as Rankine's criterion, postulates that failure begins at a given point where the maximum principal stress reaches a value equal to the tensile/compressive strength. The failure function can be expressed as [24]

$$f = \frac{\sigma_{max}}{Y_T} - 1 \quad if \quad \sigma_{max} > 0 \quad or \quad f = |\frac{\sigma_{max}}{Y_C}| - 1 \quad if \quad \sigma_{max} < 0, \tag{2.5}$$

where σ_{max} is the maximum principal stress, Y_T and Y_C are the tensile and compressive failure strength of the material, respectively. The maximum principal strain criterion is the same as the maximum principal stress criterion except the maximum principal stress is replaced by the maximum principal strain and the corresponding stress-based strength constant replaced by strain-based strength constant.

For non-isotropic materials, maximum stress or strain in the materials is used to analyze failure instead of principal stress or strain fields, the stress or strain in each direction is used to evaluate failure. This approach is commonly named as maximum stress or strain failure criterion.

IV. Tsai-Hill Failure Criterion

Tsai-Hill failure criterion requires both multiaxial normal and shear failure strength of the material to predict the failure in the material. For a three-dimensional

(3D) stress state, the failure function of the Tsai-Hill failure criterion can be expressed as [23, 25]

$$f = \sqrt{H(\sigma_{11}-\sigma_{22})^2 + F(\sigma_{22}-\sigma_{33})^2 + G(\sigma_{33}-\sigma_{11})^2 + 2(L\sigma_{23}^2 + M\sigma_{13}^2 + N\sigma_{12}^2)} - 1, \tag{2.6}$$

where

$$H = \frac{1}{2}\left(\frac{1}{X^2} + \frac{1}{Y^2} - \frac{1}{Z^2}\right), \qquad F = \frac{1}{2}\left(\frac{1}{Y^2} + \frac{1}{Z^2} - \frac{1}{X^2}\right), \qquad G = \frac{1}{2}\left(\frac{1}{Z^2} + \frac{1}{X^2} - \frac{1}{Y^2}\right), \tag{2.7}$$

$$2L = \frac{1}{R^2}, \qquad 2M = \frac{1}{S^2}, \qquad 2N = \frac{1}{T^2} \tag{2.8}$$

and X, Y and Z denote normal stress strength in 1, 2 and 3 directions, respectively, R, S and T denote shear stress strength in 2-3, 1-3 and 1-2 planes, respectively.

V. Tsai-Wu Failure Criterion

Tsai-Wu Failure criterion [26] assumes that the failure function can be expressed using a scalar form as

$$f = F_i\sigma_i + F_{ij}\sigma_i\sigma_j = 1, \qquad i, j = 1, 2, ..., 6 \tag{2.9}$$

where F_i and F_{ij} are second and fourth-order strength tensor, respectively. F_{ij} is symmetric. σ_i denote the compressed form of second-order stress tensor (σ_{rk} for r, k=1, 2, 3).

$$F_i = \begin{bmatrix} F_1 & F_2 & F_3 & F_4 & F_5 & F_6 \end{bmatrix}^T$$

and

$$F_{ij} = \begin{bmatrix} F_{11} & F_{12} & F_{13} & F_{14} & F_{15} & F_{16} \\ & F_{22} & F_{23} & F_{24} & F_{25} & F_{26} \\ & & F_{33} & F_{34} & F_{35} & F_{36} \\ & SYMM & & F_{44} & F_{45} & F_{46} \\ & & & & F_{55} & F_{56} \\ & & & & & F_{66} \end{bmatrix}$$

In this failure criterion, there are two constraints applied to Eq. (2.9). The first one is a stability condition which can be expressed for a multiaxial stress state for a general orthotropic material as

$$F_{11}F_{22}-F_{12}^2 \geq 0, \qquad F_{11}F_{33}-F_{13}^2 \geq 0, \qquad F_{22}F_{33}-F_{23}^2 \geq 0. \qquad F_{ij} > 0 \qquad for \qquad i = j \tag{2.10}$$

This condition ensures the positive semi-definiteness of the strength tensor to be consistent with physical condition. The second constraint is inadmissibility of hydrostatic failure. For this case, let equal magnitude of loads be applied in the three normal directions, i.e., $\sigma_1 = \sigma_2 = \sigma_3 = \sigma$. If failure is inadmissible for a hydrostatic stress loading condition, then Eq. (2.9) can be equated to α_1, for $\alpha_1 < 1$. This helps to simulate the condition that failure can not occur for the hydrostatic loading. Consequently, the components of F_i and F_{ij} can be related by

$$\sigma(F_1 + F_2 + F_3) + \sigma^2((F_{11} + F_{22} + F_{33}) + 2(F_{12} + F_{13} + F_{23})) < \alpha_1. \tag{2.11}$$

The components of strength tensors can be obtained for various loading cases as discussed in Ref. [26]. These components of strength constants for the unidirectional loading condition can be expressed as

$$F_1 = \frac{1}{X} - \frac{1}{X'} \qquad F_2 = \frac{1}{Y} - \frac{1}{Y'} \qquad F_3 = \frac{1}{Z} - \frac{1}{Z'} \tag{2.12}$$

$$F_4 = \frac{1}{R} - \frac{1}{R'} \qquad F_5 = \frac{1}{S} - \frac{1}{S'} \qquad F_6 = \frac{1}{T} - \frac{1}{T'} \tag{2.13}$$

$$F_{11} = \frac{1}{XX'} \qquad F_{22} = \frac{1}{YY'} \qquad F_{33} = \frac{1}{ZZ'} \tag{2.14}$$

$$F_{44} = \frac{1}{RR'} \qquad F_{55} = \frac{1}{SS'} \qquad F_{66} = \frac{1}{TT'} \tag{2.15}$$

where X/X', Y/Y' and Z/Z' denote axial tensile/compressive strength in direction $1, 2, 3$, respectively, and R/R', S/S' and T/T' denote the postive/negative shear strength of the material in 2–3, 1–3, and 1–2 planes, respectively. If we assume the shear strength is sign independent, we have $F_4 = F_5 = F_6 = 0$. The off-diagonal terms of F_{ij} can be obtained using various combined loading options, for instance,

for bidirectional tension in direction 1 and 2, let the load in both directions be equal and assumed to be σ, then F_{12} can be obtained using Eq. (2.9) as

$$F_{12} = \frac{1}{2\sigma^2}\left[1 - \sigma^2(F_{11} + F_{22}) - \sigma(F_1 + F_2)\right]. \tag{2.16}$$

It is clear to notice that for $F_1 = F_2 = 0$, the component of strength constant F_{12} can the same for tensile and compressive loading, which may not be necessarily true.

Tsai-Wu failure criterion can also be used to analyze failure in an isotropic materials by further simplify the failure function and taking certain assumptions. For instance, using Eq. (2.11), we can also obtain F_{12} for isotropic material with equal tensile and compression strength, $F_i = 0$, i=1,3, and for isotropic material, the components of strength tensor can be expressed as $F_{11} = F_{22} = F_{33}$, and $F_{12} = F_{13} = F_{23}$ and also by assuming $\alpha_1 \ll 1$, equation Eq. (2.11) can be approximated as

$$F_{12} \approx -F_{11}/2. \tag{2.17}$$

Similarly, using Eq. (2.17) and the decomposition of shear stress loading into its equivalent bidirectional normal loadings [26], one can obtain the shear components of strength tensor as

$$F_{44} = F_{55} = F_{66} = 2(F_{11} - F_{12}) = 3F_{11}. \tag{2.18}$$

Moreover, for an isotropic material with equal tensile and compressive strength, using Eq. (2.17), $F_{11} = F_{22} = F_{33}$, $F_{12} = F_{13} = F_{23}$, and $F_{44} = F_{55} = F_{66}$, it can be shown that Tsai-Wu failure criterion, Eq. (2.9), can be reduced to Eq. (2.19)

$$f = F_A((\sigma_{11} - \sigma_{22})^2 + (\sigma_{22} - \sigma_{33})^2 + (\sigma_{33} - \sigma_{11})^2) + F_B(\tau_{23}^2 + \tau_{13}^2 + \tau_{12}^2) - 1 \tag{2.19}$$

where $F_A = \frac{F_{11}}{2}$ and $F_B = F_{44}$. Using Eqs. (2.14) and (2.15), $F_A = \frac{F_{11}}{2} = \frac{1}{2XX'}$ and $F_B = F_{44} = \frac{1}{RR'}$, then Eq. (2.19) can be rewritten as

$$f = \frac{1}{2XX'}((\sigma_{11} - \sigma_{22})^2 + (\sigma_{22} - \sigma_{33})^2 + (\sigma_{33} - \sigma_{11})^2) + \frac{1}{RR'}(\tau_{23}^2 + \tau_{13}^2 + \tau_{12}^2) - 1 \tag{2.20}$$

This shows Tsai-Wu failure criterion in Eq. (2.9) can be rewritten as Eq. (2.20), which is the same as the Tsai-Hill failure criterion in Eq. (2.6). Thus, Tsai-Wu and

Tsai-Hill failure criteria yield the same predictions for an isotropic material with $H = F = G = \frac{1}{2X^2}$, $L = M = N = \frac{1}{2R^2}$ and equal tensile and compressive strength ($XX' = X^2$ and $RR' = R^2$). It can be noticed that Eq. (2.20) can be reduced to Eq. (2.3), Von Mises failure criterion, if the shear strength is approximated to be $R = \frac{Y}{\sqrt{3}}$ [6]. This shows that both Tsia-Wu and Tsai-Hill failure criteria can produce same prediction as Von Mises criterion for an isotropic material. Interested readers may refer to Ref. [26] for more details on Tsai-Wu failure criterion. The predictive capability of various failure criteria may also be obtained from Refs. [27–29].

VI. Other Failure Criteria

There are various failure criteria which are usually used to analyze composite laminates. Failure analysis of composite laminates is usually treated by assuming the constituent that controls the failure of the composite based on the material type and loading conditions. On this basis, failure analysis can be classified as matrix-controlled failure criterion and fiber-controlled failure criterion [6, 30–32]. However, it is also argued that this assumption may not be always valid as failure may be governed by all contributing factors like fiber, matrix, fiber-matrix interface and loading conditions [33]. There are also energy based failure criteria that can possibly be used to analyze failure in composites [34]. Moreover, micro plane theory is also commonly used to perform failure analysis. This theory assumes an idealized sphere at material point where the local field is projected on the surface of the sphere as vector projection. This projection is followed by decomposition of the projected fields into tangential and normal components on the surface of sphere. The fields further decomposed into volumetric and deviatoric part. The decomposed fields are then used for evaluating failure initiation and progression at the corresponding material point. This approach is also used to evaluate damage in composites [35–37]. Interested reader may refer to Refs. [29, 38] for failure analyses of composite laminates using various failure criteria.

2.1.3 Limitations of Failure Criteria

In isotropic homogeneous materials, failure can be analyzed using mainly Von Miss and Tresca criteria. It is usually observed that Von Mise criterion is mainly employed for ductile material while Tresca is used for brittle material. However, this classification may not be widely applicable for many other cases and loading conditions [6]. Consequently, several failure criteria are proposed to predict the failure strength of homogeneous materials and composite laminates including maximum principal stress criterion, maximum shear stress criterion, maximum principal strain criterion, Tsai-Hill criterion, Tsai-Wu criterion, and many others. The first three criteria are usually used to identify the failure modes in the material but they fail to capture the stress interactions for multiaxial stress state conditions. While Tsai-Wu and Tsai-Hill criteria incorporate multiaxial stress interactions but fail to capture the failure modes of the material.

In Ref. [23], Hill proposed failure criterion based on Von Mises's isotropic yield criterion. He generalized the isotropic yield criterion by adding material constants that denote directional dependency of yielding. Tsai-Hill failure criterion is derived from Hill criterion. This criterion is not applicable to materials with unequal tensile and compressive strength (Bauschinger effect). Tsai-Wu criterion [26] is the most comprehensive failure criterion that uses tensorial strength constants. The strength constant tensor has the advantage of rotational invariance, symmetric properties and it is also governed by tensor transformation laws. Tsai-Wu and Tsai-Hill failure criteria are usually used for analyzing failure in composite laminates. However, these criteria have certain limitations. For instance, the strength constants obtained under biaxial tensile loading are not uniquely and accurately obtained as pointed out by Hashin [32]. The number of strength constants required to analyze failure in the material is large particularly for Tsai-Wu criterion which requires 27 constants for a general anisotropic material. In Tsai-Wu criterion, it is usually assumed that shear loading is sign independent for composite laminates. This assumption is not consistent

with experimental observation of composite laminates under in-plane shear loading condition. For the detailed review of the limitations of these and other failure criteria, interested readers may refer to Ref. [25].

If these failure criteria can be applied at material points, some of their limitations can be easily resolved. For instance, if Tsai-Wu and Tsai-Hill failure criteria are applied at a material point, the number of strength constants required to analyze failure at lamina level are reduced at least for isotopic constituents and also the constants can be reasonably obtained. The approaches can be easily applicable for local multiaxial stress state which may give more reasonable estimates of failure strength of heterogeneous materials. By evaluating failure at a material point, it is also possible to disregard unnecessary assumptions made for composite laminate failure analysis such as sign independency of in-plane shear loading and failure modes for composite laminates under various loading conditions.

2.2 Failure Analysis Approaches in Heterogeneous Materials

In heterogeneous materials, failure is a multi-scale complex phenomenon which results from the interactions among various contributing factors such as the properties of the matrix, the fiber, the matrix-fiber interface, and the fiber volume fraction, and the loading conditions [39–41]. There are also numerous modes of failure in the heterogeneous materials including fiber fracture under tensile load, microstability (kinking) and shearing due to compressive load, matrix cracking, matrix ductile failure (without cracking), interfacial debonding, delamination and others [42]. It is extremely difficult to capture all these failure modes using any given failure criterion under various loading condition. Thus, it is critical to pay due attention to the local fields which play a vital role for the initiation and progression of failure in the material. The failure of heterogeneous materials is usually modeled using both macromechanical and micromechanical approaches.

2.2.1 Macromechanical Approach

In the macromechanical approach [43–45], failure analyses are performed based on the averaged/smeared properties of the heterogeneous materials. This approach fails to consider the local field disturbance in each constituent of heterogeneous materials. This can potentially affect the predictions of failure strength of the heterogeneous materials. Numerous researchers proposed various failure analysis approaches to treat initial and final failure/fracture of continuous fiber-reinforced composite. More than 19 failure criteria are analyzed in [2, 3, 46, 47]. It is noticed that all authors employed different assumptions and criteria for the fiber and the matrix. The majority of them used the homogenized lamina properties for predicting failure in the composite laminates. However, in some cases, the failure is analyzed by fictitiously assuming both fiber and matrix in a homogenized medium. Accordingly, both fiber and matrix failure criteria are employed depending on the loading conditions. Most of the approaches used classical lamination theory (CLT) to recover the stress/strain fields to analyze failure in the composite laminates, but CLT may not be rigourous enough to capture all fields, in particular, transverse shear and normal stress that play a significant role for delamination of composite laminates. Both linear and nonlinear analyses were suggested in many of these approaches to analyze initial and final failure of materials. Some of the models predicted final failure without analyzing the progressive damage in the material while others assumed constant or exponential stiffness degradation models.

It is also shown that the predictive capabilities of various proposed failure theories are not able to sufficiently and consistently estimate the failure strength of fiber-reinforced composites for different loading conditions as reported in the references. The main reason for inconsistent predictions of the proposed failure analysis approaches may be due to lack of using accurate local fields that significantly affect the failure of the composite. The assumptions made in formulating the failure approaches are also contributing for the ineffective analysis of failure in composite

laminates [1].

Moreover, all the proposed failure analysis approaches used for continuous fiber-reinforced composites are not applicable for other types of heterogeneous materials such as particle-reinforced composites, discontinuous fiber-reinforced composites and woven composites. This is because the assumptions are made to adopt the criteria only to continuous fiber-reinforced composites, although the predictions are still not good enough. If the failure approaches are developed based on the constituents of the heterogeneous material, particularly at a material point, the models may be reasonably used for other types of heterogeneous materials.

2.2.2 Micromechanical Approach

In a micromechanical approach, failure can be analyzed based on the constituents of the heterogeneous material. As discussed in Ref. [48], if failure happens locally, the load of a damaged part transfers to an undamaged part of the constituents. This process results in local and global load sharing through stress field. At a micro scale, failure can be analyzed using the local stress in the constituents and the local interfacial stresses or any combination of these. The local interactions determine the dominating factors that control the failure strength and behavior of the material. For example, the failure strength of silicon-carbide-fiber/titanium-matrix (SiC/T) composite is governed by the fiber volume fractions. For fiber volume fraction greater than 20%, the fiber mainly controls the failure of the composite otherwise the matrix governs the failure of SiC/T [49]. Dvorak and his co-workers [50] demonstrated that, for transversely loaded composites, matrix properties will mainly govern yielding conditions whereas for longitudinally loaded composites, the ratio of the Young's moduli of the constituents controls the failure of the composite. Hence, it is of great importance to critically investigate initial and final failure of the heterogeneous materials at a micro scale level. In a micromechanics approach, failure can be analyzed

using the local fields at three different levels: phase averaged, averaged subcell and pointwise fields (material points).

I. Phase Averaged Fields

In phase averaged based analysis, failure is estimated based on the average field in each constituent [51–54]. As discussed in WWFE [2, 3], various failure models such as Chamis, Puck, Hart-Smith and others used micromechanics approach to estimate failure strength of composite laminates. Chamis [55] uses homogenized properties however there is a stress concentration factor that is considered for the stress disturbance around a circular hole. Puck [30, 31] adopts phenomenological failure analysis approach. In this work, different failure modes are assumed based on the loading conditions. The failure of the composite was evaluated based on the average fields in the fiber and matrix for longitudinal and transverse loading conditions, respectively. Similarly, Hart-Smith [42] also used the averaged field in each constituent to evaluate failure.

Phase averaged based failure analysis approach may reasonably predict failure strength of a heterogeneous material compared to macromechanical approach. However, it is clear to notice that this approach cannot capture the effect of local field disturbance in a heterogeneous material. Thus, failure analysis, using phase averaged field, might considerably overestimate the overall strength of the material.

II. Averaged Subcell Fields

This approach uses the averaged local fields in each subcell to analyze the failure in a heterogeneous material. In Refs. [27, 56, 57], the method of cells (MOC) is employed to predict the failure strength, the initial and subsequent yield surfaces of continuous fiber-reinforced composite. Bednarcky and Arnold [49] also used the generalized method of cells (GMC) to predict the failure of viscoelastic material using the Curtin fiber breakage model and evolving complaint interfacial (ECI) model.

MOC and GMC can better predict the failure strength of composite based on the local fields. However, in MOC and GMC, the local stresses and strains are estimated by averaging local stresses and strains over each subcell, and moreover they inherently lack axial-shear coupling effect, i.e, only the normal local stresses and strains are fairly approximated. These factors can make these methods to insufficiently recover the local stress field in the constituents of heterogeneous materials for various loading conditions [4,5]. Consequently, MOC and GMC might inadequately predict the failure strength of heterogeneous materials.

III. Pointwise Fields

In this case, failure is analyzed using a material point or a pointwise numerical integration point. Scida and his co-workers [58] analyzed failure in a woven composite using a pointwise lamination approach. This approach adopts the classical lamination theory to recover the local stresses in the woven composite. This method cannot provide a good approximation for the local fields which in turn affects the prediction of failure. Choi and Tamma [59] used FEA to analyze the damage initiation in a woven composite using stiffness degradation approach for the normal and shear loading conditions. FEA is also used to analyze failure at each numerical integration point for approximating failure strength of fiber-reinforced composite [60, 61]. This approach can be reasonable for critically analyzing failure at constituent level. However, it may underestimate the failure strength of composite when defects exist in the material. These defects may be stress singularity risers such cracks and small holes. The presence of the defects may significantly affect the accurate predictions of failure strength of the composite. Moreover, the predictions of this approach are highly mesh dependent. However, if this approach is employed with the nonlocal approach that is weighted averaged field in the neighborhood of a critical point. The pointwise failure analysis can better predict failure strength of heterogeneous materials independent of mesh and at the presence of various forms of defects.

2.3 Benchmarking Study for Failure Analysis

With the increasing of the number of failure analysis approaches and tools available, the practitioner must determine which tool(s) provides the most reasonable predictions for strength related problems based on their budget, time and resource constraints. To data, two main benchmarking examples were performed to assess the technical feasibility of the state of the art of the failure analysis approaches in the composite laminates. These are: worldwide failure exercises (WWFE) and progressive damage analysis performed by Air Force Research Laboratory (AFRL).

In WWFE, 19 failure criteria were used to estimate the failure strength and stress-strain curve of composite laminates. Each approach has its own unique assumptions in terms of analyzing the initiation and progression of damage, despite a strong similarity with regard to the scale at which failure is evaluated. Some of failure criteria did not account for the progression of damage in the material. A Few representative failure criteria are briefly described here. Interested readers can refer to Ref. [62] for more.

The Eckold criterion basically used the maximum stress or strain failure criteria along with failure mode of the composite laminates. The criterion is developed based on some practical considerations, i.e., composite structural test. The approach does not consider post failure analysis, i.e., damage propagation. In this approach, failure occurs when

$$\begin{aligned} \sigma_{22} &= Y_T \quad \text{for} \quad \sigma_{22} > 0 \quad \text{and} \\ \sigma_{22} &= Y_C \quad \text{for} \quad \sigma_{22} < 0 \end{aligned} \tag{2.21}$$

$$\begin{aligned} \epsilon_{22} &= \epsilon_{22T} \quad \text{for} \quad \epsilon_{22} > 0 \quad \text{and} \\ \epsilon_{22} &= \epsilon_{22C} \quad \text{for} \quad \epsilon_{22} < 0 \end{aligned} \tag{2.22}$$

where ϵ_{22T} and ϵ_{22C} denote the failure strain.

Hart-Smith failure criterion is similar to the Eckold except that Eckold works better for for strain ($\epsilon_{22} \leq 0.001$). Both Eckold and Hart-Smith do not account for degradation after initial failure.

Puck failure criterion was developed primarily for analyzing continuous fiber-reinforced composites. This theory is formulated based on the physical mode of deformation that captures the phenomenon of failure. In this theory, various modes of failure of the composite laminates are considered by introducing physically independent failure criterion for different modes of failure. In this approach, two independent failure criteria, one for fiber failure and the other for matrix named as inter fiber failure, are evaluated at the same time at the same point. Following the result of the evaluations, the initiation of failure for a specified mode of failure will be identified.

In this approach, it is assumed that fiber is in combined state of stress. It is also implicitly assumed that the fiber carries the load for unidirectional composite loaded in longitudinal direction. Thus, for example, for composite lamina, the stress in the unidirectional composite loaded in longitudinal direction is assumed to equal to the stress in the fiber. On this basis, the failure can be initiated when the stress in the fiber reaches critical limit and this can be expressed as

$$\begin{aligned} \sigma_{f11} &= X_{fT} \quad \text{for} \quad \sigma_{f11} > 0 \quad \text{and} \\ \sigma_{f11} &= X_{fC} \quad \text{for} \quad \sigma_{f11} < 0 \quad \text{and} \end{aligned} \tag{2.23}$$

where X_{fT} and X_{fC} denote the tensile and compressive strengths of the fiber. For a linear elastic material, one can write the tensile/compressive strengths of composite laminate as

$$\begin{aligned} X_{fT} &= \tfrac{X_T}{E_1} E_{f1} = \epsilon_{T11} E_{f1} \quad \text{and} \\ X_{fC} &= \tfrac{X_C}{E_1} E_{f1} = \epsilon_{C11} E_{f1} \end{aligned} \tag{2.24}$$

where E_1 and E_{f1} denote longitudinal elastic moduli of composite and the fiber, respectively, X_T and X_C denote tensile and compressive strengths of the unidirectional composite composite. For loading conditions of $\sigma_{11} = 0$ and $\sigma_{22} > 0$, the effect of this type of loading on the fiber can be obtained by applying elasticity equation $\epsilon_f = S^f \sigma$ along with a factor that helps to approximate the transverse stress in the fiber using

the transverse stress in the composite σ_{22}. The total strain in the fiber can then be quantified as

$$\epsilon_{f11} = \frac{\sigma_{f11}}{E_{f1}} - \frac{\nu_{f12}}{E_{f1}} m_{\sigma f} \sigma_{22} \quad \text{for} \quad \sigma_{f11} > 0 \tag{2.25}$$

where ν_{f12} denotes Poisson's ratio of the fiber, $m_{\sigma f}$ denotes stress magnification effect caused by the different moduli of fibers and matrix in direction 2. It is also suggested that for carbon fiber and glass fiber, $m_{\sigma f} = 1.1$, and $m_{\sigma f} = 1.3$, respectively. For perfectly bonded interface between the fiber and the matrix, the strain in the fiber is assumed to be the strain the composite, i.e., $\epsilon_{f11} = \epsilon_{11}$. Then, one can use Eq. (2.25) to find the stress in the fiber as

$$\sigma_{f11} = \epsilon_{11} E_{f1} + \nu_{f12} m_{\sigma f} \sigma_{22} \tag{2.26}$$

This indicates that when the stress level in the composite, σ_{11}, exceeds the stress level in the fiber, σ_{f11}, the failure of the composite initiates for unidirectional lamina loaded in longitudinal direction. Under combined loading conditions $(\sigma_{f11}, \sigma_{f22})$ of the fiber, one can use Eq. (2.25), $\epsilon_{f11} = \epsilon_{11}$, and maximum strain criterion to obtain the conditions for the failure of the fiber as

$$\begin{aligned} \frac{1}{\epsilon_{T11}} \left(\epsilon_{11} + \frac{\nu_{f12}}{E_{f1}} m_{\sigma f} \sigma_{22} \right) = 1 \quad \text{for} \quad (...) > 1 \\ \frac{1}{\epsilon_{C11}} \left(\epsilon_{11} + \frac{\nu_{f12}}{E_{f1}} m_{\sigma f} \sigma_{22} \right) = 1 \quad \text{for} \quad (...) < 1 \end{aligned} \tag{2.27}$$

The failure for other combination of loading conditions and modes of failure including transverse matrix cracking can be obtained from Ref. [62]. This failure criterion uses the global or macromechanical stress/strain fields, except $m_{\sigma f}$ factor that is assumed to account for the stress increase in the fiber. But this factor is not enough to sufficiently capture the stresses in the fiber. Thus the result may not be good enough for all loading conditions at least due to the inaccurate stresses used for the evaluation of failure. Puck failure criterion accounts for degradation of stiffness by using degradation factor which varies with stress.

Chamis and Edge have similar criteria but the stress field used of the model is different. For examples, the combined transverse tension and shear that trigger the initiation of failure in matrix can be evaluated using

$$\left(\frac{\sigma_{22}}{Y}\right)^2 + \left(\frac{\tau_{12}}{S_{12}}\right)^2 = 1 \tag{2.28}$$

Chamis uses Y and S_{12} of the constituents using micromechanical analysis while Edge uses the lamina strength for both paramters.

Other failure criteria can be discussed but it is not found to be necessary. A brief survey of all the failure criteria can be obtained from Ref. [62]. In general, almost all the failure criteria used in the WWFE adopt global fields for failure analysis, which may not be accurate enough to capture the initiation and progression of damage. The results obtained from this benchmarking study showed that the failure strengths are not consistently well predicted using a given failure criteria except that one criterion shows better for one case and may be bad for the other cases. This can be possibly solved using a micromechanics approach, which the local fields for each material point and each constituent can be used to analyze the initiation and progression of failure.

The other benchmarking work was performed by Air Force Research Laboratory (AFRL). AFRL performed a benchmarking study on the progressive and fatigue failure of composite laminates. In the AFRL report, the predictions of various tools are incorporated and validated with experimental data. In this work, first, blind predictions of static failure/failure strength of the composite and fatigue life were performed. Second, the test data were provided to refine material constants, and then run the test cases again [63] to further investigate the performance of the approaches.

The main goal is to study the technical feasibility of the state of the art of damage analysis models and approaches that can provide a reasonable prediction of damage in composite laminate. This work was intended to be applied for analyzing composite structure, F-16 unitized horizontal tail strcurctres, using damage tolerant design. In the evaluation study, various tool providers and users are participated. These are: Autodesk's ASCA, AlphaSTAR's GENOA, Multiscale design system's MDS-C, and NASA Glenn's MAC/GMC, University of Michigan's enhanced Schapery theory

(EST) and N-phase cylinder (NCYL), University of Dayton Research Institute's BSAM software, Global Engineering and Materials, Inc's X-FEM software (DCN), Vanderbilt Universitys reduced-order space-time homogization software usually called eigen deformation-based reduced order homogenization method (EHM).

All the tools uses different approaches to analyze damage in composite laminates. For example, MDS-C is a multiscale approach. It uses micromechanics approach to analyze failure of composite laminates. In this approach, first, the composite laminates are modeled using lamina properties. Each material point is linked to the smaller scale, i.e., fiber and matrix with a given fiber volume fractions. During each loading step, the global field at each material point is transferred to microscale to analyze the initiation of failure using a unit cell or representative volume element (RVE) analysis. MSD-C uses a fourth order damage tensor with all the off diagonal terms are equal to zero. The growth of damage is assumed to take a linear form. The failure initiation is evaluated based on the local averaged strain in each constituents. The damage is evaluated locally based on the principal strain direction.

GMC is also in cooperated with FEA analysis, called as FEA MAC, to perform damage analysis in composite laminates. In this approach, the nonlinear response of the matrix is captured using J_2 plasticity. While the fiber remains to be elastic until failure, i.e., no plasticity in the fiber. The initiation of failure in the matrix is evaluated using maximum strain failure criterion. In this case also, failure is performed using a multiscale approach. Composite laminates are modeled using a lamina properties. Each material point is linked to a microscale RVE where the initiation of failure is analyzed at each subcell. For fiber, the maximum strain criterion was used to evaluate failure at each subcell. Once the failure criterion is met, and the longitudinal elastic modulus of subcell that corresponds to the fiber is eliminated. While for matrix, plasticity will be in place for further analyses.

NCYCL [64] is a micromechanics based model to compute nonlinear responses of unidirectional composites. In this approach, the RVE is modeled using a fiber matrix concentric cylinder as a basic repeating unit. The composite laminates are

generated using homogenized properties. The micromechanics is used to link the applied composite global strain to the fiber and matrix strains using a six by six transformation matrix. The micro damage in the matrix is captured as a nonlinear stress verse strain response. The nonlinearity of the matrix is modeled using a modified J_2 theory of plasticity. In composite laminate analysis, each point is represented by a subscale or microscale. The microscale is modeled assuming a fiber matrix concentric cylinder. The analysis at microscale is performed using a closed form solution. The average local fields in each constituent are then used to analyze the initiation and progression of failure.

Schapery Theory (ST) is developed based on principles of thermodynamics, where the work potential theory on the basis of thermodynamics are employed to model micro cracking in the matrix. The mode of failure is assumed during this analysis. Fiber breaks as mode of failure I and matrix cracks as mode of failure II. The initiation of failure is evaluated using Hashin-Roten criterion. EST also analyzes the softening of materials using a crack band model with the linear traction-displacement law. The damage constants for the analysis are obtained from +/-45 laminate.

In Global Engineering and Materials X-FEM software (DCN), failure is analyzed using three different approaches. These are: continuum damage mechanics approach along with nonlocal approach, discrete damage approach performed by introducing a finite crack at the material point where failure is initiated, and fiber aligned mesh approach where fiber orientation dependent matrix cracking is analyzed. In all of the three cases, failure is initiated when the local field reach a critical limit. While progression of failure is assumed to be driven using local energy release due to damage or fracture. During the analysis, if failure is initiated in a given ply, a finite crack is inserted along fiber directions for the three approaches. The differences between the three approaches are the critical for initiation and growth of the cracks.

BSAM essentially analyzes failure by introduction of true displacement discontinuities which is independent of mesh orientation. The failure between the plies are analyze using cohesive model. Failure analysis in this model will require to perform

thermomechanical analysis for estimating residual stress in the composite laminates. Following the thermomechanical analysis, a pre-stressed composite laminates will be subjected to incremental loading to validate the strength of the laminates. During this analysis, if failure criterion is met in the matrix, a finite crack is introduced. The process continues as the introduced crack keeps on increasing its length until the full domain breaks.

EHM uses a computational homogenization theory that adopts multiple length scales. This approach uses transformation field analysis (localization operators) to quantify the microstructural responses. As this approach is computationally prohibitive, a reduced order model is adopted by diving the model into few number of parts using a coarse mesh. This assumption will provide a smaller system of equations over a given domain. The progression of damage was analyzed by using isotropic damage. The damage potential is defined using trigonometric function.

MSD-C, GMC and NCYCL approaches use multiscale approach by linking the local to global. These approaches are good to perform failure analysis, but the use of average field at microscale cannot yield reasonable predictions particularly for MSD-C and NCYCL. For GMC, average subcell field may not able to provide a good estimate of the local fields due to lack of axial shear coupling and also type of discretization of RVE, i.e., subcells (cuboidal subcells). EHM can provide reasonable estimate but the local fields may not be well captured due to the coarse mesh. EST, DCN and BSAM used lamina properties to model and analyze failure. This approach cannot reasonable estimate local field to investigate the initiation and progression of failure.

The results of this analysis indicated that, for blind predictions, the average static strength was approximated within 20% of the test data. The predictions were improved to 10% after calibrating material constants with the test data. For fatigue case, the average blind predictions were found to be within 40% of the test data. This was improved to be within 20% after calibration. These results can potentially be improved if the a pointwise micromechanics approach is used to analyze the problem.

2.4 Interface Analysis

The failure strength of heterogeneous materials is highly influenced by the conditions of the interface among their constituents [49]. Numerous efforts have been devoted to develop constitutive models that adequately capture the effect of imperfect interface on the effective properties and the failure strength of these materials. The most common interfacial model is linear interface model, where the interfacial traction is proportional to the displacement jumps across the interface [65]. This hypothesis is adopted by numerous researchers to formulate the imperfect interface using continuum model [49, 66]. Interfacial analysis is also performed by adopting different assumptions including stress and displacement gradients jumps across the interface [67]. The interfacial analysis is commonly used to analyze the interfacial jumps in grain boundary. The jump in a grain boundary can be analyzed using displacement gradient jump, where both displacement and traction across the interface remain to be continuous. The jump is assumed to be negligible for purely elastic conditions. The effect of the jump is accounted when the material is under plastic deformation. A brief review of this approach can be obtained from Refs. [68, 69].

Needleman [70–72] proposed a cohesive zone model that exponentially relates interfacial traction with displacement jump across the interface. The normal traction increases with displacement jump, reaches maximum, and then finally drops to vanish at the complete debonding of the interface. In these works, it has also been demonstrated that the tangential traction shows a periodic function with displacement jump along the interface plane. These models do not explicitly indicate a finite traction value that initiates the debonding in the fiber-matrix interface. Lissenden [73] proposed a three dimensional (3D) polynomial traction-displacement model. This model incorporates the effect of friction between the debonded fiber and matrix in the interface.

It is also demonstrated that imperfect interface significantly affects the effective properties of heterogeneous materials [74,75]. Hashin [76] used a thin elastic interface, as an imperfect fiber-matrix interface, to obtain the effective properties of the particle-reinforced composite using a variational approach. The variational approach can better predict the upper and lower bounds of elastic effective properties with imperfect interface [67, 77]. However, the predicted bounds may be too wide for practical use. Moreover, this method can not rigorously obtain the local fields in the heterogeneous materials with complex microstructure. Thus, the effect of imperfect interface may not be sufficiently captured.

Andrianova and co-workers [78] analyzed interfacial debonding of continuous fiber-reinforced composites under the axial shear loading condition. In this work, a thin elastic bond with finite volume and rigidity is introduced between the fiber and the matrix, and the asymptotic limit for the ratio of the rigidity and volume is used for the prediction of the interfacial debonding using a linear interfacial model. Liu and Sun [79] analyzed the effect of imperfect fiber-matrix interface in a particle-reinforced composite by adopting the Eshelby's micromechanical approach. This approach cannot effectively capture the local stress fields in the composite either. Thus, the prediction may not be performed adequately. Tvergaard [80] used a linear model to analyze the imperfect interface and whiskers breakage in the discontinuous fiber-reinforced composite using cell-model analysis approach. Aboudi [66] and Lissenden [73] used MOC to analyzing the effect of imperfect interface by adopting the linear model and polynomial traction displacement model, respectively. The MOC may not sufficiently recover the local fields which mainly affect the debonding of the interface.

In Refs. [20, 49], GMC is employed to predict the interfacial debonding in the continuous fiber-reinforced composite under transverse loading condition. In these works, various traction displacement models such as flexible interfacial model, evolving interfacial model, statistical interfacial model and Needleman cohesive zone model are incorporated in GMC to predict interfacial decohesion in the composite.

GMC can better predict the interfacial debonding. However, this method may not sufficiently approximate the local stress field due to axial-shear coupling problem and also the local stresses are obtained by averaging over each subcell. Hence, the approach might inadequately predict the interfacial debonding in the heterogeneous material.

In Refs. [81–83], FEA is used to analyze the effect of imperfect fiber-matrix interface and fiber breakage of various composites by adopting linear traction displacement model. This approach can give a reasonable predictions for the interfacial debonding and also the failure strength. This is because in the FEA, the local fields can be rigorously predicted in the heterogeneous materials. This, in turn, helps to predict the effect of imperfect interface. However, in the FEA, interpenetration of interface element due to applied global load are found to be one of the major problems [82].

2.5 Types of Failure in Heterogeneous Materials

The failure analysis may be categorized in different ways but for the current study failure may be classified in three main types: initial failure, progressive failure, and fatigue failure.

2.5.1 Initial failure

Initial failure indicates the inception of failure for ductile materials, but for brittle materials the initial failure may also represent the final failure due to sudden fracture of the material immediately after the inception of the initial failure. This assumption is used in various failure analysis models [2, 60].

2.5.2 Progressive failure

In progressive failure, a material undergoes a gradual deterioration which results in final fracture. The progressive failure of a composite laminate can be characterized by: (i) initiation, (ii) growth/accumulation, (iii) stable or slow propagation of damage (up to a critical amount), and (iv) unstable or very rapid propagation [6]. Thus, failure is not usually one time process particularly in ductile materials. These processes of failure can be simulated using various models [2, 3, 84, 85]. In brittle materials, the process of gradual degradation is highly localized and may be assumed to be negligible.

Various forms of degradation models have been proposed and widely used to analyze the progressive failure of heterogeneous materials at different levels. Some models assume the matrix property to vanish at the end of initial failure while others degrade the matrix properties exponentially or with fixed constant values. These models introduce various constants that help to predict the stiffness reduction of the constituents of heterogeneous materials. The constants are commonly obtained by curve fitting with experiment data. In Ref. [86], the progressive damage of a lamina is analyzed by assuming cracking as the mode of failure for matrix and interface, and brittle fracture for fiber. The delamination of a composite laminate can also be simulated using damage analysis approach by adopting a linear traction-displacement model [87]. Various types of failure criteria including Hashin and strain-invariant approaches are commonly used in progressive damage analysis. The failure criteria are used for intimation of failure followed by the different damage evolution approaches to account for progressive damage in the fiber, the matrix and the interfaces [**?**, 88–91]. The average local field in each constituent of heterogeneous material may not provide a good estimate of local field that help analyze failure in various loading conditions.

Moreover, the damage in the progressive failure can be systematically captured and quantified using a consistent irreversible thermodynamic approach called

continuum damage mechanics (CDM) [13]. The damage propagation is estimated using isotropic or anisotropic damage variables.

2.5.3 Fatigue Failure

The evolution of permanent damage under cyclic loading can be studied using fatigue analysis. W*ö*hler [92] is a pioneer in conducting a systematic experimental investigation of fatigue failure. He experimentally illustrated the fatigue behaviour of materials using the stress-life (S-N) curve and endurance limit, i.e., the stress limit under which the material does not experience failure for an infinite number of cyclic load. In fatigue analysis, there may be two forms of failure: brittle failure when the material fail without significant plastic strain usually called high cycle fatigue (HCF) and ductile failure when the material undergoes excessive plastic strain before final failure usually described as low cycle fatigue (LCF). The fatigue life of materials is commonly presented in the stress-life (S-N) or strain-life (ϵ-N) curves based on a specified cyclic load. The experimental analysis of fatigue life is expensive, time consuming and it is also very difficult to run for complex and large components. Consequently, various approaches have been proposed and widely used to characterize the fatigue behaviour of various materials. These approaches can be classified as: total life approach and fracture mechanics. As the name indicates, the total life approach estimates the fatigue life of a material that includes the initiation, growth and final fracture of the material under cyclic loading, whereas fracture mechanics approach is commonly used to estimate fatigue life based on the crack growth rate. It requires initial macroscopic crack with finite length and its location to perform the analysis. This approach can not estimate the number of cyclic load up to the initiation of finite crack length.

The total life approach can be classified in two basic approaches: stress-life and strain-life approaches. Stress-life approach adopts stress loading mainly applicable for low stress amplitude dominated with elastic strain. The well-known Basquin's rule is

used to analyze the fatigue life for constant amplitude. This model includes the effect of mean stress on fatigue life. There are also various mean stress models including Goodman, Gerber, Soderberg and Morrow models widely used in fatigue life analysis [93]. Strain-life approach is mainly used for high strain amplitude dominated with plastic strain. Strain-life approach such as Manson-Halford, Smith-Watson-Topper are widely adopted for fatigue life analysis particularly for ductile materials. Both mean stress and strain models do not take into account the local material degradation and variable amplitude loading. The effect of variable amplitude may be analyzed using the Miner's rule that assumes linear accumulation of damage but it does not account for different load sequences [92].

Recently, a new energy based fatigue life analysis is proposed to analyze fatigue life based on both elastic and plastic energy in the material. This approach correlates the energy in the material with fatigue life [94, 95]. Interested reader may refer to Refs. [96, 97] for various similar fatigue models.

Continuum damage mechanics (CDM) is a typical phenomenological method that is extensively used in damage and fatigue life analysis of both homogeneous and heterogeneous materials [12, 14–16]. This approach uses the residual stiffness to predict the fatigue damage both in ductile and brittle materials.

A great deal of efforts have been devoted to analyze fatigue failure in homogeneous materials. However, the direct use of this approach to heterogeneous materials may not lead to reasonable predictions due to significant stress variations in the heterogeneous materials. Fatigue damage and life prediction analyses of heterogeneous materials can be performed using both macromechanical [98–103] and micromechanical [104, 105] approaches. Fatigue failure leads to sudden fracture of the material before inducing large elastic strain specifically for brittle material. The material fails to due to the applied load before the average stress or strain in each constituent reach a failure limit, particularly, for the safe life design criterion. Thus, both macromechanical and phase averaged micromechanical approaches may not

rigorously predict the fatigue damage in brittle material. The effect of fatigue damage can be better captured by the pointwise approach.

A. Fatigue Failure in Ductile Materials

Ductile materials are usually characterized by undergoing excessive plastic deformation [9,10]. Accordingly, various models have been proposed to analyze ductile damage in the heterogeneous materials using CDM. Voyiadjis and Deliktas [106] proposed anisotropic damage model for inelastic response of heterogeneous materials for both rate-independent and rate-dependent constituents. Maire and Chaboche [107] analyzed ductile damage in composite laminates with a local micro closure effect. Fish and his coworkers [108] estimated fatigue life of heterogeneuous materials using mathematical homogenization approach. This analysis is performed using CDM by adopting nonlocal isotropic damage parameter. Chaboche and his coworkers [109] also examined damage propagation in plastically deformed composites using micromechanical approaches including the Mori-Tanaka method, and the Eshelby method.

According to Ref. [33], it is experimentally observed that both fiber and matrix can experience a ductile failure for any loading direction. It is also further noticed that fiber, matrix and interface independently or all together determine the failure of the composite laminate based on the stress level in the composite. In Refs. [16, 110–114], CDM is adopted to analyze fatigue of ductile materials for various loading conditions.

B. Fatigue Failure in Brittle Materials

In CDM, it is commonly postulated that failure in brittle materials is dominated with dissipative mechanisms where viscous, thermal or other non-mechanical effects are not taken into account and moreover the plastic strain is assumed to be negligible compared with the elastic strain. These assumptions lead to elastic damage analysis for predicting fatigue damage and fatigue life prediction of brittle

materials with isotropic or anisotropic damage parameters [115–117]. On the other hand, it is hypothesized that brittle material undergoes the process of nucleation, void formation and coalescence at micro scale, which implies that the material yields plastic strain locally while the majority of the part remains elastic. On this basis, Lemaitre [118] proposed a two-scaled approach assuming that brittle materials experience a localized plastic strain. The local stress and strain fields approximated using Eshelby-Kröner localization law. Desmorat and his coworkers [119] extended the two-scaled approach for complex thermomechanical loading conditions. Doudard and his coworkers also analyzed the fatigue life of homogeneous materials using the two-scaled based probabilistic approach [120]. For detailed numerical implementation of the two-scaled approach, interested readers may refer to Ref. [121].

2.6 Residual Stiffness and Strength

In a cyclic loading, the gradual deterioration of constituents of heterogeneous materials gives rise to loss of both effective properties and strength of the materials. The residual stiffness is experimentally obtained by applying small static load after a certain specified number of cyclic load. The applied load and the displacement of the test coupon will be then used to predict the effective properties of the material. But for residual strength, the applied static load increases unit final failure [122]. The final load at which failure occurs is taken to be the residual strength of the material. It is also reasonable to assume that fatigue failure can occur when the maximum applied stress/strain is equivalent to the residual strength of the material. Both residual stiffness and strength are modeled using various deterministic and probabilistic approaches [123–125]. All of these models require accurate identification of different constants which may not be easily quantified.

2.7 Basics of Continuum Damage Mechanics (CDM)

The accurate representations of microscopic properties of a material enhance better descriptions of the macroscopic response of the material. Kachanov [126] introduced the damage variable that relates the extent of micro defects in a material to macroscopic response of the material during modeling of creep rupture. In this hypothesis, the effective cross sectional area, or loading carrying capacity, decreases as the load applied increases. If a given material is loaded, it undergoes both reversible and irreversible change internally. The irreversible part of the change signifies the damage in the material. These changes are mathematically described using damage variable that can be casted as a scalar, vector and tensor. A consistent thermodynamic framework is employed to represent the process of damage initiation, progression, and their corresponding damage variable in the form of a scalar, vector, and tensor [11–13]. The damage variable is incorporated in various constitutive equations to simulate the effect of damage in the macroscopic response of various materials. The damage variable represents the effects of distributed cavities and microdefects in the material. This concept gave rise to the concept of CDM. CDM provides a systematic approach to describing the mechanical behavior of damaged materials in a unified fashion with the concept of stiffness degradation.

2.7.1 Damage Variable

Zeroth-Order Tensor: Scalar Damage Variable

The distributions of defects in the materials, in a simplified way, can be assumed to be uniform. If these defects can have an equal effect on the materials in all directions, then the damage variable can be represented using a scalar value based on the level of damage, and it is usually expressed as an isotropic damage. This assumption is adopted for many applications where characterization of damage in all directions may be easily quantified. However, it is also argued that damage in isotropic materials

can require more than one parameter to fully describe the properties of damaged materials [127, 128]. The scalar representation of damage has limited applications as in many cases the effect of loading in one direction can possibly have different effects on different directions.

First-Order Tensor: Vector Damage Variable

In this case, the damage in a material is represented in a vector form. This looks more reasonable to assume different damage values in different directions particularly based on loading. As the area reduction hypothesis assumes, the effective area carrying the load varies depending on the damage. This approach signifies the anisotropy of the damage but limited to vector representations.

Higher-Order Tensor Damage Variable

Using higher-order tensors, damage variable can be represented using second-order and higher-order tensors. In this case, the magnitude of damage is different in all directions based on the type of loading and material properties. Thus the damage can be described using fully populated tensors. But it is very difficult to obtain all components of a fully populated damage tensor.

2.7.2 Hypothesis of Mechanical Equivalence

The degradation of material properties can be described using effective stress in a material. The effective stress is the stress obtained using a net undamaged part of the damage material. This can obtained using damage variable and mechanical equivalence between the damaged and undamaged part of the materials. This can be mathematically stated as

$$\tilde{\boldsymbol{\sigma}} = f(\boldsymbol{D})\boldsymbol{\sigma} \tag{2.29}$$

where $\tilde{\sigma}$ denotes effective stress, and $f(\boldsymbol{D})$ denotes the damage effect tensor, and $\boldsymbol{D}$ denote damage in the material which can be described using a scalar, vector or tensor. There are different forms of damage effect tensors. Interested readers can refer to Ref. [129].

With the hypothesis of mechanical equivalence between the damaged and undamaged material, the mechanical behavior of a damaged material is commonly obtained by using the concept of effective stress. Figure 2.1 shows the two representations, the first one (a) is a damaged material where mechanical properties can potentially be expressed using actual fields (stress $\boldsymbol{\sigma}$, strain $\boldsymbol{\varepsilon}$) and the damaged compliance tensor $\boldsymbol{S}(\boldsymbol{D})$ and damage variable $\boldsymbol{D}$, and the second one (b) represents a fictitiously undamaged material with compliance tensor $\boldsymbol{S_o}$, which assumes damage free material but the effect of damage is accounted within the effective stress.

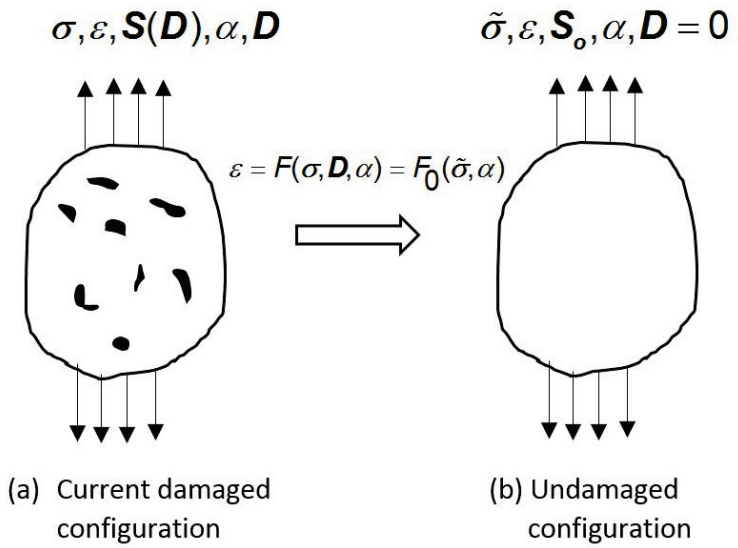

Figure 2.1. Schematic representation of strain equivalence hypothesis

The two representations are usually used to assume various hypotheses to obtain their idealized equivalency. The equivalency can be formulated based on any field and/or quantity that help to create strong relation between the two representations.

Hypothesis of Strain Equivalence

In this case, the constitutive equation of undamaged part may be expressed as a function of effective stress and damage parameters as shown in Eq. (2.30). It is hypothesized that both damaged and a fictitiously undamaged material experience the same strain

$$\varepsilon = F_0(\tilde{\boldsymbol{\sigma}}, \alpha) = F(\boldsymbol{\sigma}, \boldsymbol{D}, \alpha) \tag{2.30}$$

where $\boldsymbol{\sigma}$ denotes stress in damaged material, $\boldsymbol{D}$ denotes damage in the material, α denotes damage strengthen parameter. This approach produces asymmetric stiffness matrix that may not satisfy the requirements. The asymmetricity of stiffness matrix can be resolved by applying various approaches of symmetrization of asymmetric matrix [129].

Hypothesis of Energy Equivalence

For this case, both strain energy and complementary energy are commonly used to create equivalence between the two representations. The strain energy in both representations (damaged and undamaged) are assumed to be the same. Unlike the strain equivalence, in this case, the assumption helps to obtain symmetric stiffness matrix during damage analysis. Moreover, total energy equivalence is also commonly used to analyze damage in materials.

2.7.3 Drawbacks of Continuum Damage Mechanics (CDM)

The process of damage in a material can be captured using damage variables. These variables are easily incorporated in any finite element analysis code to simulate the initiation and progression of damage or crack. However, there are numerous issues that can be raised in this continuum damage analysis approach. The main drawbacks of CDM for numerical implementations are its pathological mesh dependency and improper convergence which originated from strain localization due

to strain softening, damage localization and stress singularity at crack tip. Numerous researchers proposed possible solutions to resolve these problems [130–132]. The common methods to solve the mesh dependency problems are nonlocal damage [133, 134], gradient method [135, 136] and viscous regularization [137]. The nonlocal approach described in Refs. [130, 133] proposed averaging weighted local field at integration points within its vicinity. The weighting value is a function of characteristic length which may be expressed using the Gaussian weighting function.

2.8 Basic of Micromechanics

The properties of any material depend on the length scale that one uses to characterize it. For instance, metals, at nano-scale, show anisotropic properties and, yet at micro and global scale, metal exhibits isotropic properties. Whereas composites show anisotropic properties both at micro and global scale due to their inherent heterogeneity particularly at micro scale. Thus, composites require very fine micro structural details for performing direct numerical simulation using FEA. However, it is nearly impossible to capture of all the details using a fine mesh and it is also computationally demanding due to large number of degrees of freedom for FEA analysis. Thus, it is a common practice to use the concept of homogenization to obtain the effective properties of composites. This concept helps to idealize composite with all its heterogeneities (for instance, fiber and matrix) to its equivalent homogeneous material properties. This approach also helps to perform dehomogenization of the local fields (stress and strain) of the composite for an arbitrary global load applied on a macro structure. The homogenization of an imaginary heterogeneous material to its equivalent homogeneous material properties is performed by using micromechanics as a tool. According to Yu and Tang [138], a typical micromechanics approach consists of the following steps:

1. investigate the microstructure of a composite and identify the periodically (at least locally) repeating unit cell (UC) or representative volume element (RVE);

2. compute the effective properties of the composite from the constitutive modeling of the UC, or to say, homogenize the composite;

3. assign the effective properties to the macroscopic structure to determine the global response;

4. substitute the global response into the UC and recover the local (displacement, strain, and stress) fields, or to say, dehomogenize the composite.

Various micromechanics models or approaches have been proposed and widely used for homogenization of heterogeneous materials. These models range from pure analytical approaches to numerical approach such as RVE analysis, usually performed using 3D finite element analysis, named as 3D FEA in this work. The most common micromechanics models are: rules of mixtures, Hashin-Shtrikman bounds, and mean field approaches such as Mori-Tanaka method, self-consistent method, generalized self-consistent method, and the method of cells and its variants, and others such as mathematical homogenization theories, mechanics of structure genome and RVE analysis.

Mean Field Approaches

The hypothesis of Eshelby's inclusion problems has made a significant contribution for the development of mean field approaches (Mori-Tanaka method, self-consistent method, generalized self-consistent method and others). Mean field approaches are semi-analytical in their formulation, and the effective properties of a heterogeneous materials are obtained based on the average fields in each constituent. The local averaged fields in each constituent are also approximated from the global load using stress/strain concentration tensor proposed by Hill [139]. The mean field approaches (MFA) can better predict the effective properties particularly the elastic modulus compared with rules of mixtures, but the predictions of shear moduli are not good enough compared with the predictions obtained from the RVE analysis. Moreover,

MFA inherently assume uniform fields in each constituent which results in inaccurate prediction of local fields. This, in turn, makes the approaches not rigorous enough to analyze failure and damage in heterogeneous materials.

Methods of Cells (MOCs)

The methods of cells and its invariants generalized method of Cells (GMC) and high fidelity generalized methods of cells (HFGMC) are proposed by Aboudi and his co-workers [140–142] to solve micromechanics problems. The basic concept of these approaches is subdividing the UC into numerous cuboid subcells, and solving for the average strain and stress over each subcell by imposing displacement and traction continuities among the adjacent subcell, and also periodic conditions on the opposite sides of the UC. The predictions of the effective properties are then obtained based on the estimates of averaged local fields of each subcell. GMC has an inherent axial-shear coupling problem due to constant displacement in subcell obtained from assumed displacement expansion. Thus, the predictions of the local fields are not accurate. HFGMC resolved the issue of axial shear coupling problem but it achieves better predictions of local fields at the expense of computing time. The MOCs and its variants solve the problems to a certain extent compared with the mean field approach but they suffer two major drawbacks. First, the use of cuboid subcells introduces domain approximation errors. Second, the use of average local fields may not rigorous enough to predict local fields variation in the microstructure at least compared with 3D RVE analysis.

Mechanics of Structure Genome (MSG)

MSG is a recently developed general approach for constitutive modeling of composites. It is a framework by carrying out an asymptotic analysis of the variational statement, synthesizing the merits of both variational methods and asymptotic methods. MSG is aimed to minimize the information loss between the

original heterogeneous material and the imaginary homogenous representations. MSG based micromechanics approach has the advantages of analytical micromechanics approaches and the versatile modeling capability of the RVE analysis. A more detailed insight of MSG is presented in the next section. Unlike other micromechanics approach, there is no ad hoc assumptions including the shape of inclusions that are considered in MSG. MSG is proven to have an outstanding capability of predicting both the effective properties and local stress fields of a heterogeneous material [5,143]. This makes MSG preferable to analyze damage and failure in heterogeneous materials.

Finite Element Analysis Based Micromechanics

This approach always require a 3D microstructure or representative volume element (RVE) to perform micromechanical analysis. It is the most common approach to obtain effective properties of the heterogenous materials. The RVE problem is analyzed by solving well posed boundary value problems, formulated using equilibrium equation without body force along with homogeneous traction or displacement boundary conditions. In this analysis, homogenous displacement, homogenous traction or periodic boundary conditions are commonly used to obtain the effective properties. In this case, a complete set of the effective properties of a given microstructure is obtained by applying boundary conditions for 6 different loading conditions. This makes RVE analysis based micromechanics approach to be inefficient compared with MSG [143].

Predictive Capabilities of Micromechanics Approaches

Various micromechanics approaches have been developed and widely used to predict the effective properties and local fields of heterogeneous materials. In order to support practitioners and researchers to select the suitable approach or tools based on their available resources, numerous analyses were performed to compare the prediction capabilities and efficiency of the developed micromechanics

approaches. In Ref. [144], the predictive capabilities of various analytical and mean field micromechanics approaches were analyzed for discontinuous fiber-reinforced composites. The effective properties and local field predictions of heterogenous materials with various microstructure were analyzed using several micromechanics approaches in Ref [4, 5, 143]. The extensive study was also conducted to critically evaluate the capabilities and also efficiency of various state of the art micromechanics approaches [143]. The evaluation showed that MSG is as accurate as 3D RVE analysis and yet more efficient.

3. MATHEMATICAL MODELING

3.1 Damage Variable

The concept of CDM is first formulated based on the hypothesis of Kachanov [126] which postulates the gradual deterioration of the effective cross-sectional area that sustains the applied load. Thus, the damage variable can be expressed as

$$d = \frac{A - \tilde{A}}{A} \tag{3.1}$$

where A denotes total cross sectional area, $\tilde{A}$ denotes effective cross-sectional area. The value of d shows the level of damage in the material when $d = 0$ shows undamage states (no damage) and, if $d = 1$ shows a complete failure. Generally, $d \leq D_c$, D_c is the critical damage level beyond which the material cannot sustain any load. The damaged constitutive model is usually expressed as

$$\boldsymbol{C}(d) = (1 - d)\boldsymbol{C} \tag{3.2}$$

where $\boldsymbol{C}$ denotes the stiffness of undamaged material. This formulation holds only for the isotropic damage. However, in most cases, the damage may not be necessarily isotropic. Thus, in general, the damage may be better expressed using a second-order tensor which considers the directional dependency of the damage parameter.

First, let $\boldsymbol{d}$ and $\boldsymbol{\mathcal{D}}$ denote the second-order and fourth-order damage tensors, respectively. Let $\boldsymbol{d}$ be symmetric, and expressed as

$$\boldsymbol{d} = \begin{bmatrix} d_{11} & d_{66} & d_{55} \\ d_{66} & d_{22} & d_{44} \\ d_{55} & d_{44} & d_{33} \end{bmatrix} \tag{3.3}$$

then mapping $\boldsymbol{d}$ in to the fourth-order tensor $\boldsymbol{\mathcal{D}}$ which can be written as

$$\boldsymbol{\mathcal{D}} = \sum_{i=1}^{3}\sum_{j=1}^{3} d_{ij} e_i \otimes e_j \otimes e_i \otimes e_j \tag{3.4}$$

The damage effect tensor $\boldsymbol{\mathcal{M}}$ can be expressed as

$$\boldsymbol{\mathcal{M}} = \boldsymbol{\mathcal{I}} - \boldsymbol{\mathcal{D}} \tag{3.5}$$

where $\boldsymbol{\mathcal{I}}$ denotes the fourth-order identity tensor. Based on the elastic strain energy equivalence of the damaged and undamaged material, the stiffness of the damaged material may be expressed as [129]

$$\boldsymbol{C}(\boldsymbol{d}) = \boldsymbol{\mathcal{M}} : \tilde{\boldsymbol{C}} : \boldsymbol{\mathcal{M}} \tag{3.6}$$

where $\boldsymbol{C}(\boldsymbol{d})$ denotes the fourth-order damaged elasticity tensor of the material, and $\tilde{\boldsymbol{C}}$ denotes the fourth-order undamaged elasticity tensor of the material.

Second, let the damage only affect the diagonal terms of compliance tensor of the material then the damaged compliance tensor can be expressed as

$$\boldsymbol{\mathcal{S}}(\boldsymbol{d}) = \begin{bmatrix} \frac{S_{1111}}{1-d_{11}} & S_{1122} & S_{1133} & S_{1123} & S_{1113} & S_{1112} \\ & \frac{S_{2222}}{1-d_{22}} & S_{2233} & S_{2223} & S_{2213} & S_{2212} \\ & & \frac{S_{3333}}{1-d_{33}} & S_{3323} & S_{3313} & S_{3312} \\ & & & \frac{S_{2323}}{1-d_{44}} & S_{2313} & S_{2312} \\ & SYMM & & & \frac{S_{1313}}{1-d_{55}} & S_{1312} \\ & & & & & \frac{S_{1212}}{1-d_{66}} \end{bmatrix} \tag{3.7}$$

Using the strain equivalence approach, the stress in the damaged and undamaged configuration can be related as

$$\tilde{\boldsymbol{\sigma}} = \boldsymbol{\mathcal{M}}^{-1} : \boldsymbol{\sigma}, \quad \boldsymbol{\mathcal{M}}^{-1} = \boldsymbol{\mathcal{S}}^{-1} : \tilde{\boldsymbol{\mathcal{S}}} \tag{3.8}$$

where $\tilde{\boldsymbol{\mathcal{S}}}$ denotes effective compliance tensor in the undamaged material, and $\boldsymbol{\mathcal{S}}$ denotes compliance in the damaged material. It should be noted that $\boldsymbol{\mathcal{M}}$ in Eq. (3.5) and Eq. (3.8) are different.

3.2 Basics of Thermodynamics

3.2.1 State Variables

In the general thermomechanical problems, the phenomena of elasticity, plasticity, and the thermal effects may be modeled using irreversible thermodynamics formulation. Any thermodynamic system can be characterized by a set of variables that describe the state of a given system. The thermodynamic state variables may be classified based on their observability as external variables and internal variable. The external variables are measured from outside while internal variables are not [129, 145]. The thermomechanical response of a given material can be adequately captured by selecting appropriate external and internal state variables.

3.2.2 Thermodynamic Free Energy

The damage/fracture in a given material can be related to various thermodynamic external and internal state variables. These external/observable state variables can be second-order elastic strain tensor $\boldsymbol{\epsilon}^e$ and temperature T with their associated variables second-order stress tensor $\boldsymbol{\sigma}$ and entropy S, respectively. The internal variables could be accumulated plastic strain r with its associated variable R and kinematic hardening variable or back stress $\boldsymbol{\alpha}$ with its associated variable $\boldsymbol{A}$, respectively. On this basis, let the Helmholtz free energy be expressed as a function of the given state variables as

$$\psi = \psi(\boldsymbol{\epsilon}^e, T, r, \boldsymbol{\alpha}, V_k) \quad (k = 1, 2, ..., n) \tag{3.9}$$

where ψ denotes energy per unit mass of the material, V_k denote other internal variables depending on the physical phenomena in the system. Similarly, the Gibbs free energy can also be expressed using the Helmholtz free energy as

$$\Gamma(T, \boldsymbol{\sigma}, V_k) = \psi - \frac{1}{\rho}\boldsymbol{\sigma} : \boldsymbol{\epsilon} \tag{3.10}$$

The Gibbs free energy is usually used to model a given thermomechanical system in stress space while the Helmholtz free energy is for strain space.

The effect of kinematic harding is observed to be negligible for large plastic strain such as in a fatigue analysis and progressive damage [11, 129]. On this basis, let accumulated plastic strain r, the second-order damage tensor $\boldsymbol{d}$ and damage hardening parameter β, be the internal variables. Moreover, let the material exhibit uncoupled plastic and damage behaviour. Thus, the Helmholtz free energy for isothermal process can be written as

$$\psi = \psi_e(\boldsymbol{\epsilon^e}, \boldsymbol{d}) + \psi_p(r) + \psi_d(\beta) \tag{3.11}$$

where ψ_e denotes the Helmholtz free energy for elastic part of the material, $\psi_p(r)$ for plastically deformed part of the material, and $\psi_d(\beta)$ for damaged part of the material.

3.2.3 Dissipation Potential Approach (DPA)

The energy is dissipated during the process of damage occurrence. The dissipation potential can then obtained as follows. Substituting Eq. (3.11) into the Clausius-Duhem inequality, one can obtain a general form of the dissipation potential as

$$(\boldsymbol{\sigma} - \rho\frac{\partial\psi}{\partial\boldsymbol{\epsilon}^e}) : \dot{\boldsymbol{\epsilon}}^{\boldsymbol{e}} + \boldsymbol{\sigma} : \dot{\boldsymbol{\epsilon}}^p - \rho\frac{\partial\psi}{\partial r}\dot{r} - \rho\frac{\partial\psi}{\partial\boldsymbol{d}} : \dot{\boldsymbol{d}} - \rho\frac{\partial\psi}{\partial\beta}\dot{\beta} \geq 0 \tag{3.12}$$

This inequality must be satisfied for any values of $\dot{\boldsymbol{\epsilon}}^{\boldsymbol{e}}$, $\dot{\boldsymbol{\epsilon}}^p$, $\dot{r}$, $\dot{\boldsymbol{d}}$ and $\dot{\beta}$. If damage $\boldsymbol{d}$ and plastic strains $\boldsymbol{\epsilon^p}$ do not exist in the material, then the inequality can be satisfied only for $\boldsymbol{\sigma} = \rho\frac{\partial\psi}{\partial\boldsymbol{\epsilon}^e}$ which gives the elastic constitutive equation. Moreover, let $\boldsymbol{y}$ and B be thermodynamic conjugate force variables and damage hardening parameter, respectively. These variables can be related to the Helmholtz free energy as

$$R \equiv \rho\frac{\partial\psi_p}{\partial r}, \qquad \boldsymbol{y} \equiv -\rho\frac{\partial\psi_e}{\partial\boldsymbol{d}}, \qquad B \equiv \rho\frac{\partial\psi_d}{\partial\beta} \tag{3.13}$$

where R accounts for the plastic energy release rate due to accumulated plastic strain. Using Eq. (3.12) and (3.13), dissipation potential per unit volume can be described as

$$\Phi = \boldsymbol{\sigma} : \dot{\boldsymbol{\epsilon}}^p - R\dot{r} + \boldsymbol{y} : \dot{\boldsymbol{d}} - B\dot{\beta} \geq 0 \tag{3.14}$$

For uncoupled plasticity and damage behaviour, the dissipation potential per unit volume Φ can decomposed into dissipation due to plasticity and damage as

$$\Phi = \Phi_p + \Phi_d \tag{3.15}$$

where

$$\Phi_p = \boldsymbol{\sigma} : \dot{\boldsymbol{\epsilon}}^p - R\dot{r} \qquad \text{and} \qquad \Phi_d = \boldsymbol{y} : \dot{\boldsymbol{d}} - B\dot{\beta} \tag{3.16}$$

3.2.4 Yield and Damage Criteria

The initiation of yielding in a material occurs when the material reaches its maximum elastic limit beyond which the material experiences plastic strain. Similarly, damage occurs when a material undergoes small deformation up to its elastic limit for brittle material but for ductile material, damage occurs after the material experiences excessive plastic strain. Thus, the yield and damage criteria can then be expressed, respectively, as

$$f_p(\boldsymbol{\sigma}, R) \leq 0 \qquad \text{and} \qquad f_d(\boldsymbol{y}, B) \leq 0 \tag{3.17}$$

One can assume a pseudo-plastic and damage potential to be $F_p(\boldsymbol{\sigma}, R)$ and $F_d(\mathbf{d}, \beta)$, respectively. Based on the dissipation mechanism, the flow rule for uncoupled plasticity and damage can be expressed using two independent multipliers, $\dot{\lambda}_p$ and $\dot{\lambda}_d$, such that the plastic and damage evolution rate can be written independently as [129]

$$\dot{\boldsymbol{\epsilon}}^p = \dot{\lambda}_p \frac{\partial F_p}{\partial \boldsymbol{\sigma}}, \qquad \dot{r} = -\dot{\lambda}_p \frac{\partial F_p}{\partial R}, \qquad \dot{\boldsymbol{d}} = \dot{\lambda}_d \frac{\partial F_d}{\partial \boldsymbol{y}}, \qquad \dot{\beta} = -\dot{\lambda}_d \frac{\partial F_d}{\partial B} \tag{3.18}$$

Once ψ, F_p, f_p, F_d, and f_d are known, the two independent multipliers can be uniquely determined.

Plasticity

For plastically deformed part of the material, it should be noted that plastic deformation can only occur in the effective stress space, i.e., undamaged part. Thus, Hill's yield criterion can be used to analyze yield surface of the undamaged part [11, 129].

$$f_p(\boldsymbol{\sigma}, R) = \sigma_{eq} - R - \sigma_y \leq 0, \qquad \sigma_{eq} = \sqrt{\frac{3}{2}(\tilde{\boldsymbol{\sigma}})' : \mathcal{H} : (\tilde{\boldsymbol{\sigma}})'} \tag{3.19}$$

where f_p denotes yield function, R denotes isotropic hardening (due to plastic strain), and σ_y denotes stress threshold, $\mathcal{H}$ denotes a positive semi-definite tensor of the fourth-order characterizing the yield condition of orthotropic materials, $()'$ denotes deviatoric part of the field. Let R be expressed using Voce hardening law as [129,145]

$$R = Q[1 - e^{(-br)}] \tag{3.20}$$

where Q and b denote isotropic hardening parameters and also let the plastic flow obey the associative flow rule, i.e., $F_p = f_p$. The loading and unloading conditions of Eq. (3.18) can be obtained using Kuhn-Tucker conditions.

$$\dot{\lambda}_p \geq 0, \quad f_p \leq 0, \quad \dot{\lambda}_p f_p = 0 \tag{3.21}$$

Then, independent multiplier of plasticity in Eq (3.18) can be uniquely obtained from consistency equation $\dot{f}_p = 0$.

$$\dot{f}_p = \frac{\partial f_p}{\partial \tilde{\boldsymbol{\sigma}}} : \dot{\tilde{\boldsymbol{\sigma}}} + \frac{\partial f_p}{\partial R}\frac{\partial R}{\partial r}\dot{r} \tag{3.22}$$

The rate equation of effective stress space for decoupled plastic damage can be written as

$$\dot{\tilde{\boldsymbol{\sigma}}} = \boldsymbol{C}(\boldsymbol{d}) : (\dot{\boldsymbol{\epsilon}} - \dot{\boldsymbol{\epsilon}}^p) \tag{3.23}$$

Substituting Eq. (3.23) into Eq. (3.22) and using Eq. (3.18) and Eq. (3.19), after a few algebraic manipulations, one obtains

$$\dot{\lambda}_p = \left(\frac{\frac{\partial f_p}{\partial \tilde{\boldsymbol{\sigma}}} : \boldsymbol{C}(\boldsymbol{d}) : \dot{\boldsymbol{\epsilon}}}{\frac{\partial f_p}{\partial \tilde{\boldsymbol{\sigma}}} : \boldsymbol{C}(\boldsymbol{d}) : \frac{\partial f_p}{\partial \tilde{\boldsymbol{\sigma}}} + \frac{\partial R}{\partial r}} \right), \qquad \dot{r} = \dot{\lambda}_p \tag{3.24}$$

Then, the evolution of plastic strain $\dot{\epsilon}^p$ in Eq. (3.18) can be written using Eq. (3.24) as

$$\dot{\boldsymbol{\epsilon}}^p = \left(\frac{\frac{\partial f_p}{\partial \tilde{\boldsymbol{\sigma}}} : \boldsymbol{C}(\boldsymbol{d}) : \dot{\boldsymbol{\epsilon}}}{\frac{\partial f_p}{\partial \tilde{\boldsymbol{\sigma}}} : \boldsymbol{C}(\boldsymbol{d}) : \frac{\partial f_p}{\partial \tilde{\boldsymbol{\sigma}}} + \frac{\partial R}{\partial r}} \right) \frac{\partial f_p}{\partial \tilde{\boldsymbol{\sigma}}} \tag{3.25}$$

Damage

For damaged part, it is assumed that there exists the damage potential $F_{\boldsymbol{d}}$, such that $F_{\boldsymbol{d}} = f_{\boldsymbol{d}} = 0$, in the space of the thermodynamic conjugate force $\boldsymbol{y}$ and B, such that the convex surface of the damage criterion may be expressed as [146]

$$f_d(\boldsymbol{y}, \boldsymbol{d}, B) = Y_{EQ} - (B_o + B) = 0 \tag{3.26}$$

where $Y_{EQ} = \left[\frac{1}{2}\boldsymbol{y} : \boldsymbol{\mathcal{L}}(\boldsymbol{d}) : \boldsymbol{y}\right]^{1/2}$ denotes equivalent damage energy release rate, B_o denotes damage threshold (material dependent value). $\boldsymbol{\mathcal{L}}(\boldsymbol{d})$ denotes the fourth-order damage tensor function which can be expressed using index notation as [146]

$$\boldsymbol{\mathcal{L}}_{ijkl} = \frac{1}{2}(\delta_{ik}\delta_{jl} + \delta_{il}\delta_{jk}) + \frac{1}{2}c^d(\delta_{ik}d_{jl} + d_{ik}\delta_{jl} + \delta_{il}d_{jk} + d_{il}\delta_{jk}) \tag{3.27}$$

where c^d denotes a material constant. Using the damage potential, damage evolution rate and the rate of change of damage parameter can be expressed as

$$\dot{\boldsymbol{d}} = \dot{\lambda}_d \frac{\partial f_d}{\partial \boldsymbol{y}}, \qquad \text{and} \qquad \dot{\beta} = -\dot{\lambda}_d \frac{\partial f_d}{\partial B} \tag{3.28}$$

where $\dot{\boldsymbol{d}}$ denotes the rate of damage flow, $\frac{\partial f_d}{\partial y}$ denotes the direction of flow of damage. Let $\rho\psi_d(\beta)$ be expressed as [129, 145]

$$\rho\psi_d(\beta) = \frac{S^2}{2Lo}, \quad S = L(1 - e^{-o\beta}) \tag{3.29}$$

Substituting Eq. (3.29) into Eq. (3.13), one can obtain

$$B = L(1 - e^{-o\beta}) \tag{3.30}$$

where L and o are constant to be obtained from curve fitting with experimental data for monotonic loading. The loading and unloading conditions of Eq. (3.28) can be obtained using Kuhn-Tucker conditions.

$$\dot{\lambda}_d \geq 0, \quad f_d \leq 0, \quad \dot{\lambda}_d f_d = 0 \tag{3.31}$$

where $\dot{\lambda}_{\boldsymbol{d}}$ is obtained from consistency conditions $\dot{f}_d = 0$ as [129]

$$\dot{f}_d = \frac{\partial f_d}{\partial \boldsymbol{y}} : \dot{\boldsymbol{y}} + \frac{\partial f_d}{\partial B}\frac{\partial B}{\partial \beta}\dot{\beta} + \frac{\partial f_d}{\partial \boldsymbol{\mathcal{L}}}\frac{\partial \boldsymbol{\mathcal{L}}}{\partial d} : \dot{\boldsymbol{d}} = 0 \tag{3.32}$$

From Eq. (3.13) and using Eq. (3.11), one can write

$$\dot{\boldsymbol{y}} = \frac{\partial \boldsymbol{y}}{\partial \boldsymbol{\epsilon^e}} : \dot{\boldsymbol{\epsilon}}^{\boldsymbol{e}} + \frac{\partial \boldsymbol{y}}{\partial \boldsymbol{d}} : \dot{\boldsymbol{d}} \tag{3.33}$$

Using Eq. (3.26), one can obtain $\frac{\partial f_d}{\partial B} = -1$, and from Eq. (3.28), $\dot{\beta} = \dot{\lambda}_d$ can be obtained, then using Eq. (3.28), Eq. (3.32) can be rewritten as

$$\dot{f}_d = \frac{\partial f_d}{\partial \boldsymbol{y}} : \left(\frac{\partial \boldsymbol{y}}{\partial \boldsymbol{\epsilon^e}} : \dot{\boldsymbol{\epsilon}}^{\boldsymbol{e}} + \frac{\partial \boldsymbol{y}}{\partial \boldsymbol{d}} : \dot{\boldsymbol{d}}\right) - \frac{\partial B}{\partial \beta}\dot{\lambda}_d + \frac{\partial f_d}{\partial \boldsymbol{\mathcal{L}}}\frac{\partial \boldsymbol{\mathcal{L}}}{\partial d} : \dot{\boldsymbol{d}} = 0 \tag{3.34}$$

Using $\dot{\boldsymbol{d}}$ from Eq. (3.28) and $\frac{\partial f_d}{\partial \boldsymbol{y}} = \frac{\boldsymbol{\mathcal{L}}:\boldsymbol{y}}{2Y_{EQ}}$, Eq. (3.34) can be simplified as

$$\dot{f}_d = \frac{1}{2Y_{EQ}}\boldsymbol{y} : \boldsymbol{\mathcal{L}} : \left(\frac{\partial \boldsymbol{y}}{\partial \boldsymbol{\epsilon^e}} : \dot{\boldsymbol{\epsilon}}^{\boldsymbol{e}}\right) + \mathbf{L}\dot{\lambda}_d = 0 \tag{3.35}$$

where $\mathbf{L} = -\frac{1}{2Y_{EQ}}\left(\boldsymbol{y} : \boldsymbol{\mathcal{L}} : \left(\frac{\partial \boldsymbol{y}}{\partial d} : \frac{\partial f_d}{\partial \boldsymbol{y}}\right)\right) - \frac{1}{4Y_{EQ}}\left(\boldsymbol{y} : \left(\frac{\partial \boldsymbol{\mathcal{L}}}{\partial \boldsymbol{d}} : \boldsymbol{y}\right) : \frac{\partial f_d}{\partial \boldsymbol{y}}\right) + \frac{\partial B}{\partial \beta}$. Then, the damage evolution rate can be expressed as

$$\dot{\lambda}_d = \frac{\frac{1}{2Y_{EQ}}\boldsymbol{y} : \boldsymbol{\mathcal{L}} : \left(\frac{\partial \boldsymbol{y}}{\partial \boldsymbol{\epsilon^e}} : \dot{\boldsymbol{\epsilon}}^{\boldsymbol{e}}\right)}{\mathbf{L}} \tag{3.36}$$

The two damage models described in Eq. (3.6) and (3.7) can be considered in this study. However, the first damage model does not give the predictions of thermodynamic conjugate force $\boldsymbol{y}$ consistent with the dissipation potential Φ_d in Eq (3.16) that require $\boldsymbol{y} \equiv -\rho\frac{\partial \psi_e}{\partial \boldsymbol{d}} \geq 0$. For instance, for uniaxial global loading, the model gives $y_{22} < 0$ and $y_{33} < 0$ while $y_{11} > 0$. Moreover, as one obtains large value of damage in axial direction and small values for all other damage, all components of

$\boldsymbol{y} < 0$. This problem is partly due to the effect of Poisson's ratio. For unidirectional loading, there will be deformation particularly contractions in transverse direction. Thus, the effect of the transverse strain yields $y_{22} < 0$ and $y_{33} < 0$. However, the problem may not be encountered for multi-directional loadings. It is also noticed that many fourth-order damage effect tensors with zero off-diagonal terms also suffer a similar problem.

For the second damage model, thermodynamic conjugate force $\boldsymbol{y}$ can alteratively be obtained from Gibbs free energy from Eq (3.10) or complementary energy $\boldsymbol{G}$ using the proposed damage model, Eq (3.7), as [100]

$$\boldsymbol{y} = \frac{\partial \boldsymbol{G}}{\partial \boldsymbol{d}}, \qquad \boldsymbol{G} = \frac{1}{2}\sigma : \boldsymbol{S}(\boldsymbol{d}) : \sigma \tag{3.37}$$

3.3 Elasto-Plastic Constitutive Equation

The uncoupled elastoplastic constitutive equation of the damaged material is derived as follows. From additive decompositions of strain one can have

$$\boldsymbol{\epsilon} = \boldsymbol{\epsilon}^e + \boldsymbol{\epsilon}^p \tag{3.38}$$

The rate equation for effective stress can be written as

$$\dot{\tilde{\boldsymbol{\sigma}}} = \frac{\partial \tilde{\boldsymbol{\sigma}}}{\partial \boldsymbol{\epsilon}_e} : \dot{\boldsymbol{\epsilon}}_e + \frac{\partial \tilde{\boldsymbol{\sigma}}}{\partial \boldsymbol{d}} : \dot{\boldsymbol{d}} \tag{3.39}$$

Ductile Failure

For ductile failure, it can be postulated that the material undergoes excessive plastic deformation before failure occurs. Thus, using Eq. (3.38), Eq. (3.39) can be rewritten as

$$\dot{\tilde{\boldsymbol{\sigma}}} = \boldsymbol{C}(\boldsymbol{d}) : (\dot{\boldsymbol{\epsilon}} - \dot{\boldsymbol{\epsilon}}^p) + \frac{\partial \tilde{\boldsymbol{\sigma}}}{\partial \boldsymbol{d}} : \dot{\boldsymbol{d}} \tag{3.40}$$

Substituting Eq (3.25) into Eq (3.40) and using Eq (3.36) and (3.28) and $\frac{\partial \tilde{\boldsymbol{\sigma}}}{\partial \boldsymbol{d}} = \frac{\partial \boldsymbol{C}(\boldsymbol{d})}{\partial \boldsymbol{d}} : \boldsymbol{\epsilon}$, the rate equation for uncoupled damaged elastoplastic constitutive equation can be expressed for small incremental loading as

$$\delta\tilde{\boldsymbol{\sigma}} = \mathcal{C}^{epd} : \delta\boldsymbol{\epsilon} \tag{3.41}$$

where $\mathcal{C}^{epd}$ denotes damaged elastoplastic tangent stiffness tensor and it can be expressed as

$$\mathcal{C}^{epd} = \boldsymbol{C}(\boldsymbol{d}) - \frac{\left(\boldsymbol{C}(\boldsymbol{d}) : \frac{\partial f_p}{\partial \tilde{\boldsymbol{\sigma}}}\right) \otimes \left(\frac{\partial f_p}{\partial \tilde{\boldsymbol{\sigma}}} : \boldsymbol{C}(\boldsymbol{d})\right)}{\frac{\partial f_p}{\partial \tilde{\boldsymbol{\sigma}}} : \boldsymbol{C}(\boldsymbol{d}) : \frac{\partial f_p}{\partial \tilde{\boldsymbol{\sigma}}} + \frac{\partial R}{\partial r}} + \frac{1}{Y_{EQ}\,\mathbf{L}} \left(\frac{\partial \boldsymbol{C}(\boldsymbol{d})}{\partial \boldsymbol{d}} : \boldsymbol{\epsilon}\right) \left(\frac{\partial f_d}{\partial \boldsymbol{y}} \otimes (F_{Ly\epsilon})\right) + C_{pd} \tag{3.42}$$

where $F_{Ly\epsilon} = \boldsymbol{y} : \boldsymbol{\mathcal{L}} : \frac{\partial \boldsymbol{y}}{\partial \boldsymbol{\epsilon}^e}$, and

$$C_{pd} = -\frac{1}{Y_{EQ}\,\mathbf{L}} \left(\frac{\partial \boldsymbol{C}(\boldsymbol{d})}{\partial \boldsymbol{d}} : \boldsymbol{\epsilon}\right) \left(\frac{\partial f_d}{\partial \boldsymbol{y}} \otimes (F_{Ly\epsilon})\right) \left(\frac{\frac{\partial f_p}{\partial \tilde{\boldsymbol{\sigma}}} \otimes \left(\frac{\partial f_p}{\partial \tilde{\boldsymbol{\sigma}}} : \boldsymbol{C}(\boldsymbol{d})\right)}{\frac{\partial f_p}{\partial \tilde{\boldsymbol{\sigma}}} : \boldsymbol{C}(\boldsymbol{d}) : \frac{\partial f_p}{\partial \tilde{\boldsymbol{\sigma}}} + \frac{\partial R}{\partial r}}\right) \tag{3.43}$$

where the first term in Eq (3.42) represents elastic case, the second term for plastic case, the third term is for damage, and the fourth term represents the combined effect of both plasticity and damage.

Brittle Failure

For brittle failure, it is assumed that the plastic strain is negligible. Thus, the constitutive law for elastic damage analysis for a small incremental load can be obtained from Eq (3.42) for $\boldsymbol{\epsilon}^p \approx 0$ and $\boldsymbol{\epsilon} \approx \boldsymbol{\epsilon}^e$ as

$$\mathcal{C}^{epd} = \boldsymbol{C}(\boldsymbol{d}) + \frac{1}{Y_{EQ}\,\mathbf{L}} \left(\frac{\partial \boldsymbol{C}(\boldsymbol{d})}{\partial \boldsymbol{d}} : \boldsymbol{\epsilon}^e\right) \left(\frac{\partial f_d}{\partial \boldsymbol{y}} \otimes (F_{Ly\epsilon})\right) \tag{3.44}$$

3.4 Failure Criteria Approach (FCA)

This approach is similar to the first-ply type failure analysis approach [29], which commonly used to analyze failure in composite laminate. The difference is in FCA

approach, failure is analyzed at material point, while the first-ply approach, failure is analyzed at lamina level, i.e. macromechanical approach. The current approach also uses stiffness degradation method. Thus, we can use the second-order damage tensor in Eq (3.3) and also the damaged compliance tensor in Eq (3.7). In this case, a material point is evaluated using a given failure criterion and a specified damage value is assigned. This can be analyzed as follows.

First, failure is evaluated at each numerical integration point using any given failure criterion in all directions, i.e., analyzing failure for all normal and shear stresses/strains using the corresponding strengths. Second, if failure occurs in any direction, the stiffness in the corresponding direction will be set to be negligible/small. That is, the value of d_{ij} in the corresponding direction set to be close to unit value so that the stiffness is sufficiently degraded. This can be seen by using Eq (3.7). For instance, if the failure happens in direction 1, then $d_{11} \approx 0.99999$ while others $d_{ij} << d_{11}$. The loading increment continues until sufficient number of material points are degraded. Based on the global response of the SG, the number of material points sufficient to create final failure are iteratively calibrated using experimental data. It can be calibrated as follows. First, assume if 10% of the total material points fail, the whole SG will fail, and perform the analysis, and compare the result with experiment. If the predicted strength is above the experimental data, reduce it to 5% and try again, but if the predicted strength is less than the experimental data and increase to 15% and try again. The volume of material points which better match with the experimental data is then selected.

3.5 nonlocal Approach

The pathological mesh dependency of local continuum damage mechanics can be solved using various nonlocal approaches. The nonlocal field can be obtained by smearing damage variable or local fields over the entire material or constituents. However, in damage analysis, where localized material degradations play a major role

for gradual or sudden failure of a component, it is more reasonable to consider the weighted average local field computed within its proximity than smearing over the whole material domain. The weighted averaged local field for a given point can be obtained as [130, 133, 134]

$$\langle f \rangle = \frac{\int_v w f \, dv}{\int_v w dv} \tag{3.45}$$

where $\langle f \rangle$ denotes weighted averaged local fields (strains/stresses) at integration point, $w(l)$ denotes Gaussian weighting functions expressed as $w(l) = e^{-(\alpha_w l/\lambda_w)^2}$. The parameter λ_w denotes characteristic length for averaging the local field, v denotes the domain occupied by λ_w, l denotes the location of points from a point of interest and should not be greater than the λ_w. The smallest domain could be averaging within an element, and α_w denotes weighing function. The damage potential surface (threshold), damage evolution rate, elastic energy release rate, damage parameter can then be expressed using the pointwise nonlocal fields designated as $\bar{f}_{\boldsymbol{p}}$, $\bar{f}_{\boldsymbol{d}}$, $\bar{\lambda}_{\boldsymbol{d}}$, $\overline{\boldsymbol{y}}$ and $\overline{\beta}$, respectively.

3.6 Interfacial Constitutive Model

Various models have been proposed and widely used to analyze the effect of imperfect interface on the properties of heterogeneous materials [49]. These models may be categorized as linear and nonlinear interfacial models. For the present study, let the interfaces among the different constituents be subjected to infinitesimal displacement jumps across the interface. The linear traction displacement model can then be adopted to analyze the effect of imperfect interface on the effective properties and failure strength of these materials. The linear traction displacement model may be expressed as [147]

$$T_i = \overline{D}_{ij}[u_j], \qquad [u_j] = u^1 - u^2, \tag{3.46}$$

where T_i denote interfacial traction, and $[u_j]$ denote displacement jumps cross the interface between constituent 1 and 2, and $\overline{D}_{ij}$ denote the second-order interface constitutive tensor (interface stiffness with unit (Pa/m)). The interfacial displacement

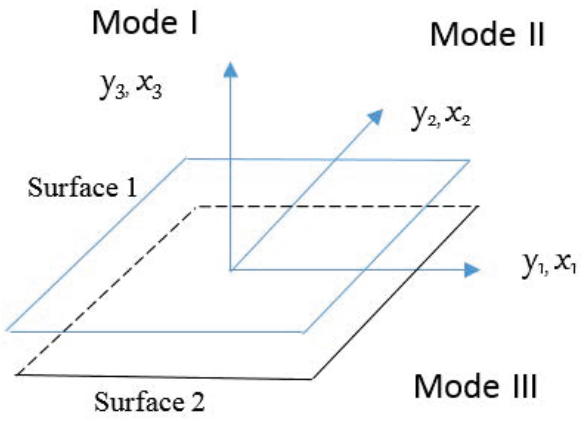

Figure 3.1. Interface failure modes between two surfaces

jump or failure can be expressed by three modes. Let the displacement jump normal to the interface be represented as Model I failure with the corresponding interfacial stiffness, $\overline{D}_I$, and let the two displacement jumps in the plane of the interface be presented as Mode II and Mode III failures with the corresponding interfacial stiffness $\overline{D}_{II}$ and $\overline{D}_{III}$, respectively, as shown in Figure 3.1. The two surfaces are attached to each other initially, i.e., the interface has zero thickness with a specified stiffness. The displacement of the surface 1 and 2 can be, respectively, discretized as

$$u_i^1(x_j, y_k) = S^1(y_k)V_i^1(x_j) \quad \text{and} \quad u_i^2(x_j, y_k) = S^2(y_k)V_i^2(x_j) \tag{3.47}$$

where x and y denote the macro and micro variables, u_i^p denote displacement vector on the surface p in direction i, S^p denote the shape function and V_i^p denote the nodal displacement vector on the surface p. Then, the displacement jump across the interface can be written using a matrix notation as

$$[u] = [S]\,V \quad \text{where } [u] = u^1 - u^2, \quad [S] = \begin{bmatrix} S^1 & -S^2 \end{bmatrix}, \quad V = \begin{Bmatrix} V^1 \\ V^2 \end{Bmatrix} \tag{3.48}$$

Let the displacement jumps in all directions are decoupled, i.e, tangential displacement in one direction does not affect the other tangential and/or the normal displacement jump. Thus, Eq. (3.46) can be casted as

$$\left\{ \begin{array}{c} T_1 \\ T_2 \\ T_3 \end{array} \right\} = \left[\begin{array}{ccc} \overline{D}_{III} & 0 & 0 \\ 0 & \overline{D}_{II} & 0 \\ 0 & 0 & \overline{D}_{I} \end{array} \right] \left[\begin{array}{cc} S^1 & -S^2 \end{array} \right] \left\{ \begin{array}{c} V^1 \\ V^2 \end{array} \right\} \tag{3.49}$$

For a 3D SG, we can have a four-noded interface element. The displacement vector and the shape function of the interface element can be expressed as

$$V^p = \left\{ \begin{array}{cccccccccccc} u_1^{p1} & u_2^{p1} & u_3^{p1} & u_1^{p2} & u_2^{p2} & u_3^{p2} & u_1^{p3} & u_2^{p3} & u_3^{p3} & u_1^{p4} & u_2^{p4} & u_3^{p4} \end{array} \right\}^T \tag{3.50}$$

and

$$S^p = \left[\begin{array}{cccccccccccc} N_1 & 0 & 0 & N_2 & 0 & 0 & N_3 & 0 & 0 & N_4 & 0 & 0 \\ 0 & N_1 & 0 & 0 & N_2 & 0 & 0 & N_3 & 0 & 0 & N_4 & 0 \\ 0 & 0 & N_1 & 0 & 0 & N_2 & 0 & 0 & N_3 & 0 & 0 & N_4 \end{array} \right] \tag{3.51}$$

where u_i^{pk} denote the displacement in the local coordinate y_i direction for surface p at the node k, S^p denote the shape function for surface p, and N_k denote the components of shape function at node k. Similarly, for a 2D SG, we can have two-noded interface element. The displacement vector and the shape function can be expressed as

$$V^p = \left\{ \begin{array}{cccccc} u_1^{p1} & u_2^{p1} & u_3^{p1} & u_1^{p2} & u_2^{p2} & u_2^{p2} \end{array} \right\}^T \tag{3.52}$$

and

$$S^p = \left[\begin{array}{cccccc} N_1 & 0 & 0 & N_2 & 0 & 0 \\ 0 & N_1 & 0 & 0 & N_2 & 0 \\ 0 & 0 & N_1 & 0 & 0 & N_2 \end{array} \right]. \tag{3.53}$$

For a 1D SG, the displacement vector and the shape function of the interface element can be expressed

$$V^p = \left\{ \begin{array}{ccc} u_1^{p1} & u_2^{p1} & u_3^{p1} \end{array} \right\}^T \tag{3.54}$$

and

$$S^p = \begin{bmatrix} 1 & 0 & 0 \\ 0 & 1 & 0 \\ 0 & 0 & 1 \end{bmatrix} \tag{3.55}$$

and consequently, Eq. (3.49) can be expressed for 1D as

$$\begin{bmatrix} T_1 \\ T_2 \\ T_3 \end{bmatrix} = \begin{bmatrix} \overline{D}_{III} & 0 & 0 \\ 0 & \overline{D}_{II} & 0 \\ 0 & 0 & \overline{D}_{I} \end{bmatrix} \begin{bmatrix} 1 & 0 & 0 & -1 & 0 & 0 \\ 0 & 1 & 0 & 0 & -1 & 0 \\ 0 & 0 & 1 & 0 & 0 & -1 \end{bmatrix} \begin{Bmatrix} u_1^{11} \\ u_2^{11} \\ u_3^{11} \\ u_1^{22} \\ u_2^{22} \\ u_3^{22} \end{Bmatrix} \tag{3.56}$$

One of the basic and necessary assumption in the homogenization of heterogeneous materials is that the exact solutions of the field variables have volume averages over the SG. For example, if u_i are the exact displacements within the SG, there exist v_i such that

$$v_i = \frac{1}{\Omega}\int_\Omega u_i d\Omega \equiv \langle u_i \rangle, \tag{3.57}$$

where Ω denotes the domain occupied by a SG and also its volume, and $\langle\cdot\rangle$ denotes the volume average over Ω. Using this equation, it is common to express the exact solution u_i as a sum of the volume average v_i and the difference, such that

$$u_i(x,y) = v_i(x) + w_i(x,y), \tag{3.58}$$

where $w_i(x,y)$ usually called fluctuating function. It is clear that $\langle w_i \rangle = 0$ according to Eq. (3.57). Interested readers may refer to Ref. [148–150] for more details. In the view of Eq. (3.58), the displacement jump $[u]$ in Eq. (3.46) and (3.48) can be rewritten as

$$[u] = [w], \tag{3.59}$$

Using Eqs. (3.48), (3.49) and (3.59), the strain energy due to interfacial displacement jumps can be expressed as

$$W_{int} = \frac{1}{2}\int_\gamma [w]^T \overline{D}\,[w]\, d\gamma \;= \frac{1}{2}\int_\gamma V^T \overline{D}^* V\, d\gamma \tag{3.60}$$

where W_{int} denotes interfacial strain energy and γ denotes interface area in side SG, V denotes displacement vector of the interface, V depends on the dimension of SG as described above, and $\overline{D}^*$ denote a interfacial stiffness which may be expressed as

$$\overline{D}^* = [S]^T \overline{D}[S] \tag{3.61}$$

3.7 Mechanics of Structure Genome (MSG)

MSG provides a general-purpose micromechanics theory when it is applied to constitutive modeling of 3D structures. The term genome is used to emphasize the fact that it contains all the constitutive information needed for a structure the same fashion as the genome contains all the intrinsic information for an organisms growth and development. For 3D bodies, A SG serves a similar role as a RVE or unit cell (UC) concept in micromechanics (see Figure 3.2). However, they are different. For example, for a structure made of composites featuring 1D heterogeneity (e.g. binary composites made of two alternating layers, see Figure 3.2(a), the SG will be a straight line with two segments denoting corresponding different layers. A 3D SG for 3D structures represents the most similar case to RVE. However, boundary conditions in terms of displacements and tractions indispensable in RVE-based models are not needed for SG-based models. Interested reader can refer to Yu [151] for more details on MSG. The properties of heterogeneous materials vary with scale and also in view of the fact that the size of SG is much smaller than the overall size of the macroscopic structure, we introduce a set of micro coordinates $y_i = x_i/\epsilon$ with ϵ being a small parameter to describe the SG. This basically enables a zoom-in view of the SG at the size similar as the macroscopic structure. If the SG is 1D, only y_3 is needed; if the SG is 2D, y_2 and y_3 are needed; if the SG is 3D, all three coordinates y_1, y_2, y_3 are needed.

In multiscale structural modeling, it is postulated that all the information can be obtained from the SG in combination with the macroscopic structural model. In other words, a field function of the original heterogeneous structure can be generally written as a function of the macro coordinates x_k which remain in the macroscopic

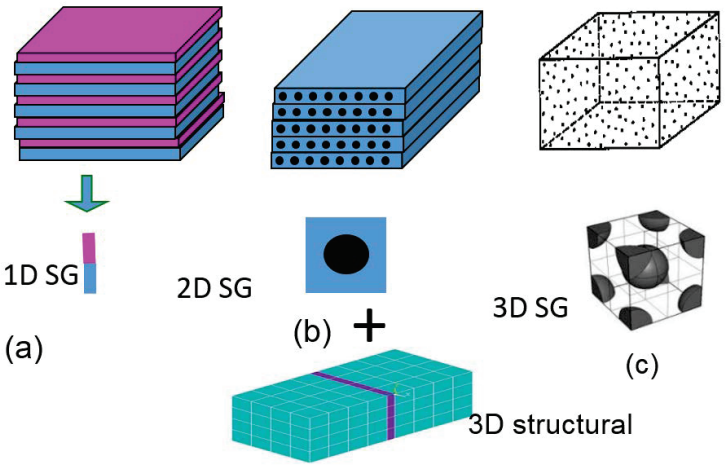

Figure 3.2. SG for different dimensions

structural model and the micro coordinates y_j. The partial derivative of a function $f(x_k, y_j)$ can be expressed as

$$\frac{\partial f(x_k, y_j)}{\partial x_i} = \frac{\partial f(x_k, y_j)}{\partial x_i}|_{y_j=\text{const}} + \frac{1}{\epsilon}\frac{\partial f(x_k, y_j)}{\partial y_i}|_{x_k=\text{const}} \equiv f_{,i} + \frac{1}{\epsilon}f_{|i} \tag{3.62}$$

The deformed and undeformed configurations of structure of any type can be expressed using position vector based on the type of the structure we have, i.e., beam, plate/shell, 3D structure. Interested readers can get details of this method in Ref. [151]. The governing equation can be expressed using the following variational statement

$$\delta U = \overline{\delta W} \tag{3.63}$$

δ is the usual Lagrangean variation, U is the strain energy and $\overline{\delta W}$ is the virtual work of applied loads. The bars over variations are used to indicate that the virtual quantity needs not be the variation of a functional. For a linear elastic material characterized using a 6×6 stiffness matrix D and assuming imperfect interface among the constitutes of the heterogeneous materials, the strain energy can be written as

$$U = \frac{1}{2}\int\frac{1}{\omega}\left\langle\Gamma^T D\Gamma\right\rangle \mathrm{d}\Omega + \frac{1}{2}\int\frac{1}{\omega}\int_\gamma([u]^T\overline{D}[u])\mathrm{d}\gamma\mathrm{d}\Omega, \tag{3.64}$$

where Ω is the volume of the domain spanned by x_k remaining in the macroscopic structural model, ω denotes the volume of the domain spanned by y_k corresponding

to the coordinates x_k, remaining in the macroscopic structural model and $[u]$ denotes the interfacial jump across the interface of the constituents, $\overline{D}$ denotes second-order interfacial constitutive tensor (interfacial stiffness) and γ denotes the area domain spanned by the interface, Γ denotes 3D strain field which can be written as

$$\Gamma = \Gamma_h w + \Gamma_\epsilon \bar{\epsilon} \tag{3.65}$$

where $\Gamma = \lfloor \Gamma_{11} \;\; \Gamma_{22} \;\; \Gamma_{33} \;\; 2\Gamma_{23} \;\; 2\Gamma_{13} \;\; 2\Gamma_{12} \rfloor^T$, $w = \lfloor w_1 \;\; w_2 \;\; w_3 \rfloor^T$, $\bar{\epsilon}$ is a column matrix containing the generalized strain measures for the macroscopic structural model, $\bar{\epsilon} = \lfloor \epsilon_{11} \;\; \epsilon_{22} \;\; \epsilon_{33} \;\; 2\epsilon_{23} \;\; 2\epsilon_{13} \;\; 2\epsilon_{12} \rfloor^T$ with ϵ_{ij}. Γ_h is an operator matrix which depends on the dimensionality of the SG. Γ_ϵ is an operator matrix, which is 6×6 identity matrix for 3D Model. By using the variational statement in Eq. (3.63), the strain energy in Eq. (3.64) and (3.60) and also using Eq. (3.59), the first approximation of variational statement obtained in Ref. [152] can be modified, for imperfect interface among the constituents, as

$$\delta \frac{1}{2} (\langle (\Gamma_h w + \Gamma_\epsilon \bar{\epsilon})^T D (\Gamma_h w + \Gamma_\epsilon \bar{\epsilon}) \rangle + \langle [w]^T \overline{D} [w] \rangle^*) = 0. \tag{3.66}$$

where $\langle \cdot \rangle^*$ denotes integrating over interface area domain. For very simple cases, this variational statement can be solved analytically, while for general cases we need to use numerical techniques such as the finite element method for solution which has been implemented in the computer code SwiftComp.

3.7.1 Analytical Solution

For layered composites (see Figure 3.2(a)), Eq. (3.66) can be analytically solved to obtain the exact solution. In this case, the heterogeneity only occurs through the thickness along y_3 as shown in the Figure and, in $y_1 - y_2$ plane, each layer is homogeneous. Thus, w_i are functions of y_3 only, that is, the partial derivatives of the fluctuation functions $w_{i,j}$ vanish except for $w_{i,3}$. Similarly, the interface is assumed to have uniform traction and displacement jumps. The minimization

problem for micromechanical analysis of layered composites with imperfect interface can be restated using a matrix form as

$$\Pi = \frac{1}{2}\left\langle \Gamma^T D \Gamma \right\rangle + \frac{1}{2}\left\langle [w]^T \bar{D}[w] \right\rangle^* \tag{3.67}$$

with $\Gamma = \begin{bmatrix} \bar{\varepsilon}_{11} & \bar{\varepsilon}_{22} & \bar{\varepsilon}_{33} + \frac{\partial w_3}{\partial y_3} & 2\bar{\varepsilon}_{23} + \frac{\partial w_2}{\partial y_3} & 2\bar{\varepsilon}_{13} + \frac{\partial w_1}{\partial y_3} & 2\bar{\varepsilon}_{12} \end{bmatrix}^T$ as the microscopic strain field. The microscopic stress field within SG can be obtained as

$$\sigma = D\Gamma \tag{3.68}$$

with $\sigma = \begin{bmatrix} \sigma_{11} & \sigma_{22} & \sigma_{33} & \sigma_{23} & \sigma_{13} & \sigma_{12} \end{bmatrix}^T$ holding the six components of the stress tensor. Using constraints on the fluctuation functions

$$\langle w_i \rangle = 0, \quad \left\langle w_{(i,j)} \right\rangle = 0 \tag{3.69}$$

and by applying the normal procedures of calculus of variations and enforcing the constraints using Lagrange multipliers, one can obtain three Euler-Lagrangain equations as

$$\frac{\partial}{\partial y_3}\left(\sigma_{13} - D_{22}[\chi_1]\right) = 0, \quad \frac{\partial}{\partial y_3}\left(\sigma_{23} - D_{33}[\chi_2]\right) = 0, \quad \frac{\partial}{\partial y_3}\left(\sigma_{33} - D_{11}[\chi_3]\right) = 0. \tag{3.70}$$

Similarly, one can also derive the following conditions relating the transverse stresses at the boundary points of SG

$$\sigma_{i3}\left(y_1, y_2, -\frac{h}{2}\right) = \sigma_{i3}\left(y_1, y_2, \frac{h}{2}\right). \tag{3.71}$$

The three stress continuity conditions on each interface of the layers can be expressed as

$$[\sigma_{i3}] = 0 \tag{3.72}$$

Using Eq. (3.70) and (3.72), one can obtain the relationship between the stress and displacement jumps as

$$\sigma_{13} - D_{II}[\chi_1] = 0, \quad \sigma_{23} - D_{III}[\chi_2] = 0, \quad \sigma_{33} - D_I[\chi_3] = 0. \tag{3.73}$$

Following the procedures described in Yu [149, 153] and using Eq. (3.69) and Eqs. (3.71)-(3.73), one can solve the problem analytically. It should be noted that only unique/representative layers are to be used for the analysis. For instance, if two layers of different material properties are repeated to generate the layered composite with n number of layers, only the 2 unique layers would be used for the analysis. First, for the simple case of two isotropic layers, the effective properties of layered composite with imperfect interface can then be obtained as

$$E_1 = E_2 = \phi_1 E^{(1)} + \phi_2 E^{(2)} + \frac{\phi_1 \phi_2 E^{(1)} E^{(2)} (\nu^{(1)} - \nu^{(2)})^2}{\phi_1 E^{(1)} (1 - \nu^{(2)^2}) + \phi_2 E^{(2)} (1 - \nu^{(1)^2})} \tag{3.74}$$

$$G_{12} = \frac{\phi_1 E^{(1)}}{2(\nu^{(1)} + 1)} + \frac{\phi_2 E^{(2)}}{2(\nu^{(2)} + 1)} \tag{3.75}$$

$$G_{13} = \frac{D_{III}^2 \phi_1 E^{(1)} E^{(2)^2} (1+\nu^{(1)})^2 (\frac{1}{2}+\frac{1}{2}\nu^{(2)}) + D_{III} E^{(1)^2} E^{(2)} (E^{(2)} (\frac{1}{4}+\nu^{(1)} (\frac{1}{4}+\frac{1}{4}\nu^{(2)}) + \frac{1}{4}\nu^{(2)}))}{M_{III}} + \frac{D_{III}^2 \phi_2 E^{(1)^2} E^{(2)} (\frac{1}{2}+\frac{1}{2}\nu^{(1)})(1+\nu^{(2)})}{M_{III}} \tag{3.76}$$

$$G_{23} = \frac{D_{II}^2 \phi_1 E^{(1)} E^{(2)^2} (1+\nu^{(1)})^2 (\frac{1}{2}+\frac{1}{2}\nu^{(2)}) + D_{II} E^{(1)^2} E^{(2)} (E^{(2)} (\frac{1}{4}+\nu^{(1)} (\frac{1}{4}+\frac{1}{4}\nu^{(2)}) + \frac{1}{4}\nu^{(2)}))}{M_{II}} + \frac{D_{II}^2 \phi_2 E^{(1)^2} E^{(2)} (\frac{1}{2}+\frac{1}{2}\nu^{(1)})(1+\nu^{(2)})}{M_{II}} \tag{3.77}$$

$$\nu_{12} = \frac{\phi_1 E^{(1)} \nu^{(1)} (\nu^{(2)^2} - 1) + \phi_2 E^{(2)} \nu^{(2)} (\nu^{(1)^2} - 1)}{\phi_1 E^{(1)} (\nu^{(2)^2} - 1) + \phi_2 E^{(2)} (\nu^{(1)^2} - 1)} \tag{3.78}$$

$$\nu_{13} = \nu_{23} = \frac{(\nu^{(1)} \nu^{(2)} - \phi_1 \nu^{(1)} - \phi_2 \nu^{(2)})(\phi_1 E^{(1)} (1 + \nu^{(2)}) + \phi_2 E^{(2)} (1 + \nu^{(1)}))}{\phi_1 E^{(1)} (\nu^{(2)^2} - 1) + \phi_2 E^{(2)} (\nu^{(1)} - 1)} \tag{3.79}$$

where $M_\alpha = K_v \big(-\frac{1}{2} E^{(1)} E^{(2)} + D_\alpha \left(\phi_1 E^{(1)} (1 + \nu^{(2)}) - \phi_2 E^{(2)} (1 + \nu^{(1)}) - E^{(1)} (1 + \nu^{(2)})\right)\big)^2$, $K_v = (1 + \nu^{(1)})(1 + \nu^{(2)})$, $\alpha = III \ or \ II$, with ϕ_i denotes the volume fraction or thickness fraction of layer i, $E^{(i)}$ and $\nu^{(i)}$ elastic modulus and Poisson's ratio of layer i. The explicit exact solution of E_3 is very lengthy, thus it is not shown here, but it is observed to be affected by D_I. Eqs. (3.74)-(3.75), (3.78) and (3.79) can be reduced to the ones obtained by Yu [149] for a perfectly bonded interface. Eqs. (3.74)-(3.75), (3.78) and (3.79) show that the effective elastic modulus E_1 and E_2, the shear modulus G_{12}, all Poisson's ratios $(\nu_{12}, \nu_{13}, \nu_{23})$ are independent of interfacial stiffness, while G_{13} and G_{23} are dependent on the interfacial stiffness, D_{III} and D_{II}, respectively, as shown in Eq. (3.76) and Eq. (3.77).

Second, for more general case, let the properties of layers be monoclinic. The effective properties of the layered composite can be expressed as

$$\begin{bmatrix} C_{11}^* & C_{12}^* & C_{13}^* & 0 & 0 & C_{16}^* \\ & C_{22}^* & C_{23}^* & 0 & 0 & C_{26}^* \\ & & C_{33}^* & 0 & 0 & C_{36}^* \\ & & & C_{44}^* & C_{45}^* & 0 \\ & SYMM & & & C_{55}^* & 0 \\ & & & & & C_{66}^* \end{bmatrix} \tag{3.80}$$

For the special case of a composite made of two monoclinic layers, the components of the stiffness tensor can be obtained as

$$\begin{aligned}
&C_{11}^* = \langle C_{11}\rangle + C_{11}^E(C^{(1)}, C^{(2)}, D_I), \qquad C_{12}^* = \langle C_{12}\rangle + C_{12}^E(C^{(1)}, C^{(2)}, D_I) \\
&C_{16}^* = \langle C_{16}\rangle + C_{16}^E(C^{(1)}, C^{(2)}, D_I), \qquad C_{26}^* = \langle C_{26}\rangle + C_{26}^E(C^{(1)}, C^{(2)}, D_I) \\
&C_{22}^* = \langle C_{22}\rangle + C_{11}^E(C^{(1)}, C^{(2)}, D_I), \qquad C_{23}^* = \frac{D_I(C_{23}^{(2)}C_{33}^{(1)}\phi_2 + C_{23}^{(1)}C_{33}^{(2)}\phi_1)}{(C_{33}^{(2)}\phi_1 + C_{33}^{(1)}\phi_2)D_I + C_{33}^{(2)}C_{33}^{(1)}} \\
&C_{33}^* = \frac{D_I C_{33}^{(1)}C_{33}^{(2)}}{(C_{33}^{(2)}\phi_1 + C_{33}^{(1)}\phi_2)D_I + C_{33}^{(2)}C_{33}^{(1)}}, \qquad C_{13}^* = \frac{D_I(C_{13}^{(2)}C_{33}^{(1)}\phi_1 + C_{13}^{(1)}C_{33}^{(2)}\phi_2)}{(C_{33}^{(2)}\phi_1 + C_{33}^{(1)}\phi_2)D_I + C_{33}^{(2)}C_{33}^{(1)}} \\
&C_{36}^* = \frac{D_I(C_{36}^{(2)}C_{33}^{(1)}\phi_2 + C_{36}^{(1)}C_{33}^{(2)}\phi_1)}{(C_{33}^{(2)}\phi_1 + C_{33}^{(1)}\phi_2)D_I + C_{33}^{(2)}C_{33}^{(1)}}, \qquad C_{44}^* = \frac{D_{II}C_{44}^{(2)}C_{44}^{(1)}}{(C_{44}^{(2)}\phi_1 + C_{44}^{(1)}\phi_2)D_{II} + C_{44}^{(2)}C_{44}^{(1)}} \\
&C_{55}^* = \frac{D_{III}C_{55}^{(2)}C_{55}^{(1)}}{(C_{55}^{(2)}\phi_1 + C_{55}^{(1)}\phi_2)D_{III} + C_{55}^{(2)}C_{55}^{(1)}}, \qquad C_{66}^* = C_{66}^{(1)}\phi_1 + C_{66}^{(2)}\phi_2 = \langle C_{66}\rangle \\
&C_{45}^* = \frac{D_{III}D_{II}(C_{44}^{(2)}C_{45}^{(1)}C_{55}^{(2)}\phi_1 + C_{44}^{(1)}C_{45}^{(2)}C_{55}^{(1)}\phi_2)}{((C_{55}^{(2)}\phi_1 + C_{55}^{(1)}\phi_2)D_{III} + C_{55}^{(2)}C_{55}^{(1)})((C_{44}^{(2)}\phi_1 + C_{44}^{(1)}\phi_2)D_{II} + C_{44}^{(2)}C_{44}^{(1)})}
\end{aligned} \tag{3.81}$$

where C_{ij}^E are symbols introduced to save space for some lengthy formulas. It appears that all components of the tensor are affected by interfacial stiffness except C_{66}^*. It is also clear that C_{45}^* is affected by both D_{II} and D_{III}, while all others are affected by only one interfacial stiffness D_I, or, D_{II}, or D_{III}. It can easily be verified that as the

interfacial stiffness goes to large value, all the components of effective stiffness tensor converge to the result obtained by Yu [149] for perfect interface.

3.7.2 Numerical Solution

To obtain numerical solution, one needs to express w using shape functions defined over SG as

$$w(x_k, y_j) = S(y_j)V(x_k) \tag{3.82}$$

where S represents the shape functions and V denotes a column matrix of the nodal values of the fluctuating functions. Substituting Eq.(3.82) into Eq.(3.66) and using Eq.(3.61), we obtain the the following discretized version of the strain energy functional

$$U = \frac{1}{2}\left(V^T E V + 2V^T D_{h\epsilon}\bar{\epsilon} + \bar{\epsilon}^T D_{\epsilon\epsilon}\bar{\epsilon} + V^T \overline{D}_{int} V\right) \tag{3.83}$$

where

$$E = \left\langle (\Gamma_h S)^T D (\Gamma_h S) \right\rangle \quad D_{h\epsilon} = \left\langle (\Gamma_h S)^T D \Gamma_\epsilon \right\rangle \quad D_{\epsilon\epsilon} = \left\langle \Gamma_\epsilon^T D \Gamma_\epsilon \right\rangle \quad \overline{D}_{int} = \left\langle \overline{D}^* \right\rangle^* \tag{3.84}$$

Minimizing U in Eq. (3.83) subject to the constraints, gives us the following linear system

$$(E + \overline{D}_{int})V = -D_{h\epsilon}\bar{\epsilon} \tag{3.85}$$

It is clear that V will linearly depend on $\bar{\epsilon}$, and the solution can be symbolically written as

$$V = V_0\bar{\epsilon} \tag{3.86}$$

Substituting Eq. (3.86) back into Eq. (3.83), we can calculate the strain energy storing in the SG as the first approximation as

$$U = \frac{1}{2}\bar{\epsilon}^T \left(V_0^T D_{h\epsilon} + D_{\epsilon\epsilon}\right)\bar{\epsilon} \equiv \frac{\omega}{2}\bar{\epsilon}^T \bar{D}\bar{\epsilon} \tag{3.87}$$

where $\bar{D}$ is the effective stiffness to be used in the macroscopic structural model. The local fields within the original heterogeneous structure can also be obtained as described in Ref. [151].

4. NUMERICAL EXAMPLES

In this section, the prediction results of initial failure load, initial failure envelop, progressive damage and fatigue life for heterogeneous materials are presented. Several representative examples of heterogeneous materials including binary composite, continuous fiber-reinforced composite, particle-reinforced composite, discontinuous fiber-reinforced composite and woven composites are used to demonstrate the capability of the current approach to predict failure in heterogeneous materials.

4.1 Initial Failure Predictions

In this section, the predictions of initial failure and initial failure envelope of heterogeneous materials are performed using various micromechanics approaches such as mean field approach, i.e, Mori-Tanaka (MT) [144, 154] and Double Inclusions (DI) [155], generalized methods of cells (GMC), high fidelity generalized methods of cells (HFGMC) [156], SwiftComp and 3D FEA. These approaches employ different methods of analyzing failure in heterogeneous materials. In the mean field approach, failure is generally assumed to occur when the average stress/strain in one of the constituents reaches failure point. The outputs of MT and DI are obtained using DIGIMAT 5.1.1 software from MSC Software and e-Xstream engineering. In GMC and HFGMC, failure is assumed to be initiated when the local stress/strain averaged over the subcell reaches its limiting point. The results of GMC and HFGMC are obtained using micromechanics analysis code MAC/GMC 4.0 developed by NASA Glenn Research Center [157]. The in-built failure analysis of this approach supports only maximum stress/strain and Tsai-Hill failure criteria. For SwiftComp and 3D FEA, failure is assumed to be initiated when the stress/strain at a numerical integration point (Gauss Point) reaches its maximum limiting value based on the

failure criterion. SwiftComp is also used to predict initial failure using a nonlocal approach, i.e., weighted averaged local field, at numerical integration points denoted as SwiftComp*. In this case, characteristic length, λ_w, and the parameter, α_w, are assumed to be 10% of the shortest dimensional side of the SG and $\lambda_w^2/2$, respectively. The results of 3D FEA are obtained using ANSYS by employing periodic boundary conditions. The in-built failure analysis of ANSYS uses maximum stress failure criterion, maximum strain failure criterion, Tsai-Wu failure criterion and Tsai-Hill failure criterion for evaluating failure. All failure analyses are performed using material properties listed in Table 4.1. It is assumed that the tensile and compressive strengths are equal.

Table 4.1. Material properties for failure analysis (Refs. [60,158])

Type	Material	E (GPa)	ν	Strength (GPa)	Shear strength (GPa)	Allowable normal strains
1	Fiber	130	0.30	2.800	-	0.0215
	Matrix	3.50	0.35	0.070	-	0.0200
2	Fiber	86	0.22	4.800	2.400	0.0553*
	Matrix	4.30	0.34	0.083	0.040	0.0198*

* Approximated based on maximum stress failure criteria.

The predictions of initial failure strength are performed using several representative examples of composites such as continuous fiber-reinforced composite, particle-reinforced composite, discontinuous fiber-reinforced composite, and woven composite. The initial failure strength and envelope are analyzed using various failure criteria such as maximum normal/shear stress criterion, Tsai-Hill criterion, Tsai-Wu criterion, maximum shear stress criterion, and maximum normal strain criterion. Finally, the predictions of SwiftComp are compared with the predictions of mean field approach, GMC, HFGMC, and 3D FEA for all examples of composites.

4.1.1 Continuous Fiber-Reinforced Composite

The SG of continuous fiber-reinforced composite is generated by assuming that a circular fiber is embedded in a square matrix. Let the local Cartesian coordinate be introduced at the center of SG as $y = (y_1, y_2, y_3)$ with y_1 is parallel to the fiber direction as depicted in Figure 4.1. A in-built 26×26 subcell grid is used for GMC

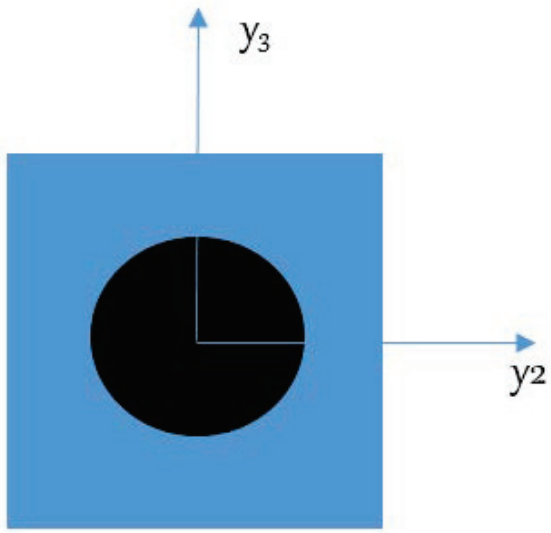

Figure 4.1. SG for continuous fiber-reinforced composite

and HFGMC, and a mesh of 4500 8-noded quadrilateral and SOLID95 elements are used for SwiftComp and 3D FEA, respectively. First, let the material properties listed in Table 4.1 (type 1) and the fiber volume of 63% be used to predict the initial failure strength of the composite. Table 4.2 shows that all approaches except HFGMC show good agreements for maximum normal stress criterion. However, the current predictions are observed to be greater than the predictions obtained from Ref. [60] as shown in Table 4.2. The difference of these predictions may be due to the failure evaluation method. In Ref. [60], failure is evaluated at central integration points of each element, which is obviously diferent from analyzing failure based on average local fields. The other factor may be mesh size and element type used in the reference (not described). For transverse strength, except for the mean field approaches, the other

approaches predict relatively closer to the predictions obtained from Ref. [60]. The predictions obtained using nonlocal approach, SwiftComp*, are close to SwiftComp and 3D FEA, which suggests that there are moderate stress gradients in the matrix.

Table 4.2. Axial and transverse failure strength of continuous fiber-reinforced composite using the maximum normal stress failure criterion

Strength	MT	DI	GMC	HFGMC	SwiftComp*	SwiftComp	FEA	Ref. [60]
Axial (GPa)	1.64	1.60	1.62	1.76	1.61	1.60	1.60	1.31
Transverse (MPa)	89.36	140.91	40.26	41.16	35.47	34.10	34.21	37.44

The predictions of the axial and transverse failure strengths are also analyzed for material property of type 2 using maximum normal stress and Tsai-Hill failure criteria. Tables 4.3 and 4.5 show that the axial strength of the composite increases with fiber volume fraction for both failure criteria. On the contrary, except for the mean field approaches and HFGMC, the transverse strength decreases for maximum stress failure criterion, see Table 4.4. In the transverse direction, failure is mainly governed by matrix and the stress gradient at the fiber-matrix interface. The increase of fiber volume fraction will increase the stress gradient thereby increases the chance of failure of the composite. But this is not observed to be the same for Tsai-Hill failure criterion, see Table 4.6. It shows that Tsai-Hill criterion predicts the failure strength with slight difference irrespective the change of volume fraction from 1% to 60%. Generally, all approaches produce close prediction of axial failure strength for relatively lower fiber volume fractions for both failure criteria, but the predictions of transverse failure strength are found to be significantly different, see Tables 4.4 and 4.6. It is also clear that the mean field approaches poorly estimate both the axial and transverse failure strengths particularly for larger fiber volume fractions. The main reason for the poor predictions of the failure strength may be due to the fact that in these approaches, failure is evaluated based on the average stress in the matrix and the fiber. The approaches fail to accurately recover the local stress and strain fields

within the matrix, the fiber and particularly in the fiber-matrix interface where large stress/strain gradient is most likely to occur. The predictions of GMC and HFGMC are better compared with the mean field approaches as the failure is evaluated at subcell level, except unreasonable prediction of HFGMC for 60% of fiber volume fractions for both failure criteria and failure strengthes. However, the predictions obtained from these approaches are also observed to be different from the predictions obtained based on a pointwise stress, i.e., SwiftComp and 3D FEA. This may be due to the approximation of local fields in the approaches, i.e., averaging of the local fields over sub cell. The predictions obtained from SwiftComp* are slightly greater than the SwiftComp and 3D FEA for both axial and transverse strengths, which indicates slight stress gradients in the composite. It is clear that the micromechanics based failure analysis has a remarkable potential to predict the initial failure strength of the composite.

Table 4.3. Axial failure strengths of continuous fiber-reinforced composite using the maximum normal stress failure criterion

	Axial strength (MPa)						
Vof(%)	MT	DI	GMC	HFGMC	SwiftComp*	SwiftComp	3D FEA
1	99.00	98.92	100.00	100.00	98.35	95.37	95.36
20	339.11	393.98	392.00	440.00	391.72	389.19	389.17
60	1001.5	956.43	970.00	1200.00	973.07	963.26	963.55

The initial failure envelopes are also generated using maximum normal stress and Tsai-Hill failure criteria. Figure 4.2 indicates that GMC slightly overpredicts the initial failure limit of the composite for the combined loading conditions, i.e, the axial and transverse loading conditions, compared with the predictions of 3D FEA, while SwiftComp shows an excellent agreement with 3D FEA. Please note that failure envelopes data are normalized using σ_{110} and σ_{220}, which denote the failure strength of the composite in uniaxial and transverse directions, respectively. For Tsai-Hill

Table 4.4. Transverse failure strengths of continuous fiber-reinforced composite using the maximum normal stress failure criterion

	Transverse strength (MPa)						
Vof(%)	MT	DI	GMC	HFGMC	SwiftComp*	SwiftComp	3D FEA
1	83.64	83.76	74.88	74.00	68.19	51.51	51.66
20	90.16	92.79	56.94	82.00	55.38	52.26	52.27
60	103.91	146.1	50.70	170.00	45.42	44.20	44.19

Table 4.5. Axial failure strength of continuous fiber-reinforced composite using the Tsai-Hill failure criterion

	Axial strength (MPa)						
Vof(%)	MT	DI	GMC	HFGMC	SwiftComp*	SwiftComp	3D FEA
1	98.89	98.89	100.00	100.00	98.71	97.59	97.32
20	402.26	402.26	399.00	440.00	397.51	395.60	395.28
60	1047.7	1073.00	1022.00	1200.00	1002.04	999.08	998.76

Table 4.6. Transverse failure strength of continuous fiber-reinforced composite using the Tsai-Hill failure criterion

	Transverse strength (MPa)						
Vof(%)	MT	DI	GMC	HFGMC	SwiftComp*	SwiftComp	3D FEA
1	85.69	85.69	77.60	77.60	75.51	67.98	67.98
20	102.84	105.96	69.30	96.00	69.65	67.51	67.82
60	124.95	178.72	74.70	269.5	77.64	73.11	73.09

failure criterion, Figure 4.3, GMC predicts well except slight deviation from 3D FEA. The initial failure envelope generated by SwiftComp agrees well with the prediction of 3D FEA. The prediction of mean field approaches (MT and DI) are not presented,

because DIGIMAT does not support bidirectional stress load loading option. The predictions obtained from SwiftComp* are close to the predictions of SwiftComp and 3D FEA as depicted in the figures for both failure criteria.

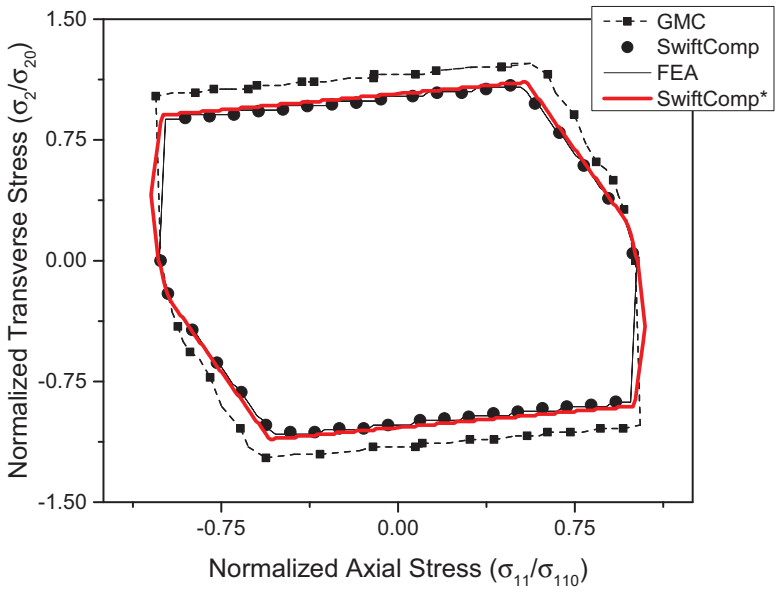

Figure 4.2. Initial failure envelope of continuous fiber-reinforced composite (maximum normal stress failure criterion for 60% vof)

The shear failure strength is also predicted using axial and transverse shear loading conditions. In this case, the Tsai-Hill and maximum shear stress failure criteria are used to predict the strength of the composite. The material properties listed in Table 4.1 (type 2) are used for this analysis. Please note that the current version of DIGMAT 5.1.1 does not support shear loading option, thus the results of mean field approaches are omitted. Table 4.7 shows that the predictions of shear failure strength, similar to the transverse normal loading, are dependent on stress disturbance that decreases with fiber volume fractions. The composites with higher fiber volume fractions sustain lower shear load. In this prediction, it is observed that the axial shear failure strength of GMC is close to the predictions of SwiftComp and 3D FEA for relative larger fiber volume fraction while the predictions of HFGMC are

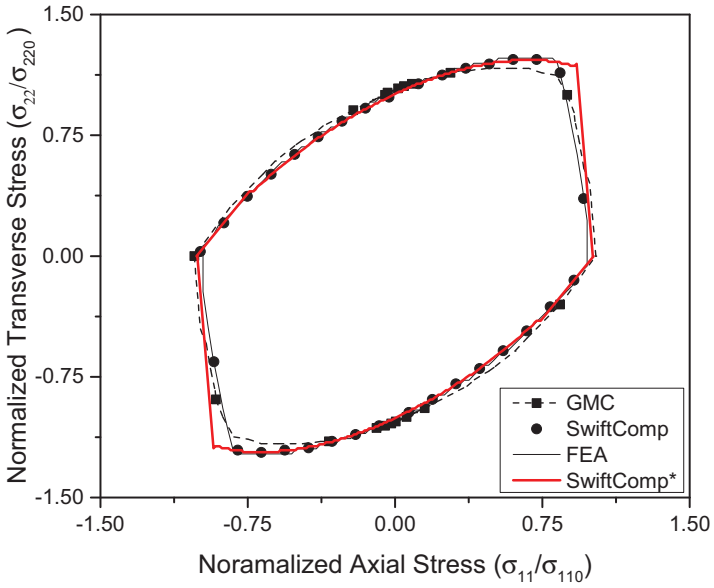

Figure 4.3. Initial failure envelope of continuous fiber-reinforced composite (Tsai-Hill failure criterion for 60% vof)

significantly different. The predictions of transverse shear failure strength of GMC remains to be same for all fiber volume fractions. On the other hand, HFGMC predicts the transverse shear strength fairly well compared with 3D FEA. On the contrary, SwiftComp shows excellent agreements with the predictions of 3D FEA. It is also noticed that maximum shear stress and Tsai-Hill failure criteria produce very close predictions. For this reason only Tsai-Hill failure criterion is presented in Table 4.7. The predictions obtained from SwiftComp* are slightly greater than the predictions of SwiftComp and 3D FEA for both axial and transverse shear stress particularly for higher fiber volume fraction, but it shows large difference for lower volume particularity for 1% which may result from higher stress gradient near the interface that decay within short distance. Moreover, the combined shear loading conditions, i.e., axial and transverse shear, can be used to generate the initial failure envelope of the continuous fiber-reinforced composite. The outputs of mean field approaches, GMC, and HFGMC are also omitted as the corresponding codes do not

Table 4.7. Axial and transverse shear failure strength of continuous fiber-reinforced composite using the Tsai-Hill failure criterion

	Axial shear strength (MPa)					Transverse shear strength (MPa)				
Vof(%)	GMC	HFGMC	SwiftComp*	SwiftComp	3D FEA	GMC	HFGMC	SwiftComp*	SwiftComp	3D FEA
1	36.62	33.95	32.27	25.52	25.52	40.02	34.92	37.53	34.04	34.06
20	27.30	37.20	26.51	24.60	24.61	40.02	28.13	32.04	31.84	31.85
60	21.85	68.60	23.24	22.10	22.09	40.02	30.07	31.31	28.23	28.18

provide options for this type of loading conditions. Figure 4.4 shows that the initial failure envelope of SwiftComp and 3D FEA show excellent agreement, while the predictions obtained from SwiftComp* shows slight deviations from 3D FEA, which results from the gradients of local stress.

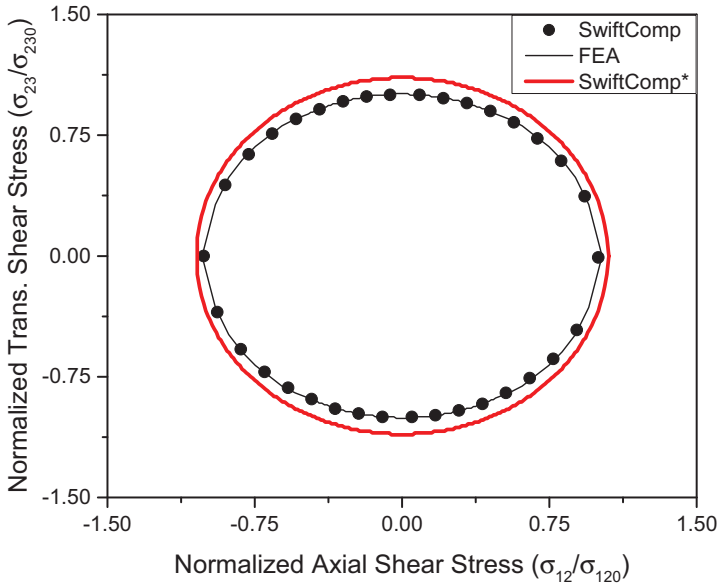

Figure 4.4. Initial failure envelope of axial and transverse shear of continuous fiber-reinforced composites (for 60% vof)

Finally, maximum normal strain failure criterion is employed to predict the strength of the continuous fiber-reinforced composite using strain or displacement loading conditions. In this case, an interesting result is observed for the axial

failure strain. All approaches including SwiftComp* and 3D FEA produce the same predictions of axial failure strain approximated to be 0.019 for the material property (type 2) irrespective of the fiber volume fractions. However, this is not observed to be the same for the transverse failure strain prediction. Table 4.8 shows that the mean field approaches and HFGMC overpredict the transverse failure strain compared to 3D FEA. Moreover, Figure 4.5 shows that mean field approaches overpredict the initial failure envelope nearly by more than 2.7 times compared to 3D FEA. GMC shows a better prediction of the envelope, although not as good as SwiftComp compared with 3D FEA. The predictions of nonlocal approach, i.e., SwiftComp*, SwiftComp and 3D FEA show excellent agreement. ε_{220} and ε_{330} represent the failure strain for longitudinal and transverse directions, respectively.

Table 4.8. Transverse shear failure strength of continuous fiber-reinforced composites using the maximum normal strain failure criterion

Vof(%)	MT	DI	GMC	HFGMC	SwiftComp*	SwiftComp	3D FEA
1	0.019	0.019	0.0173	0.0174	0.0165	0.0149	0.0149
20	0.016	0.016	0.0103	0.0155	0.0100	0.0095	0.0098
60	0.009	0.009	0.0037	0.0152	0.0034	0.0033	0.0033

The nonlocal approach can also be used to predict the initial failure strength of the composite with stress singularity risers such as cracks and small holes. In this study, let two artificial finite length cracks (7.34% of the SG length) be introduced at the fiber-matrix interface as shown in Figure 4.6 and also let the fiber volume fraction be 50%. The mesh at the crack point is locally refined four times while the global mesh remains the same. The initial failure strengths of the SG are predicted for each local mesh refinement. Figures 4.7 and 4.8 indicate that for the pointwise local stress field, i.e., SwiftComp and 3D FEA, the predictions of initial failure strength of the composite are severely affected by the local mesh refinements, while for the nonlocal

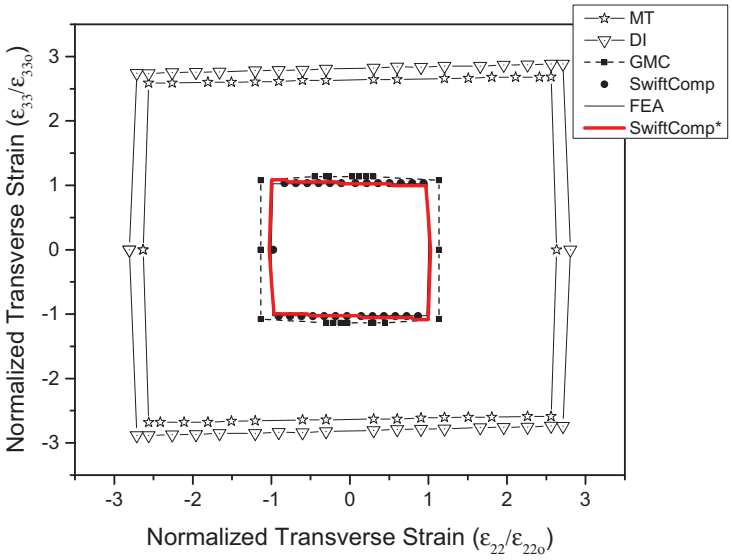

Figure 4.5. Initial failure envelope of continuous fiber-reinforced composite using maximum normal strain failure criterion (for 60% vof)

approach, i.e., SwiftComp*, the initial failure strength is consistently predicted for various local mesh refinement and also the prediction is slightly greater than 3D FEA and SwiftComp for normal loading, which results from averaging the large stress at the crack tip. However, for the transverse shear loading, the predictions of initial failure strength are observed to be significantly different. This is due to higher stress gradient, i.e., singularity, at the crack tips. As these stresses are numerical artifacts, their effects are partially smoothed out by averaging over the characteristic length.

In another example, let a rectangular fiber be used to demonstrate a contact point in SG as shown in the Figure 4.9. Let the fiber volume be 50%. In this case also, for different local mesh refinements, the initial failure strengths are evaluated at numerical integration points using SwiftComp and 3D FEA. However, the predictions are found to be mesh dependent, while the nonlocal approach,

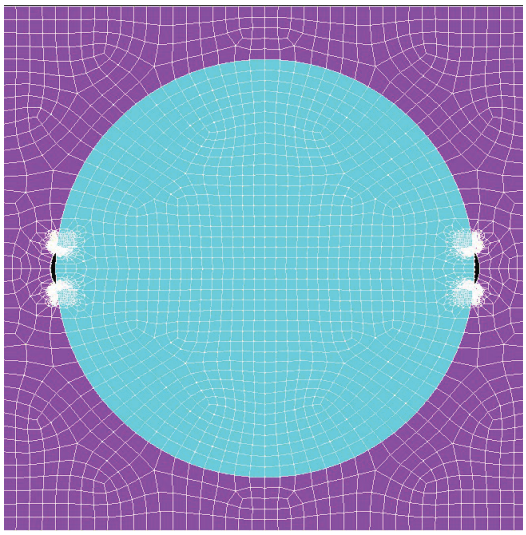

Figure 4.6. SG with finite length artificial cracks

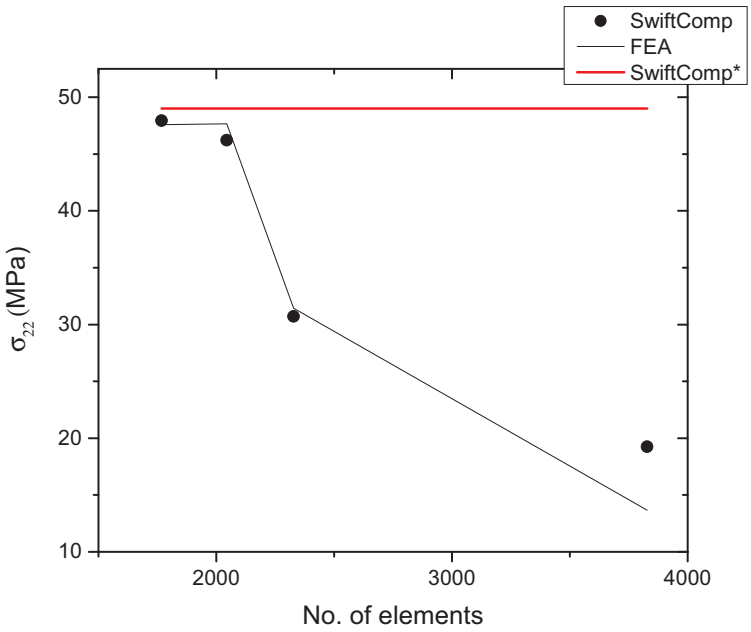

Figure 4.7. Prediction of σ_{22} using the maximum normal stress failure criterion

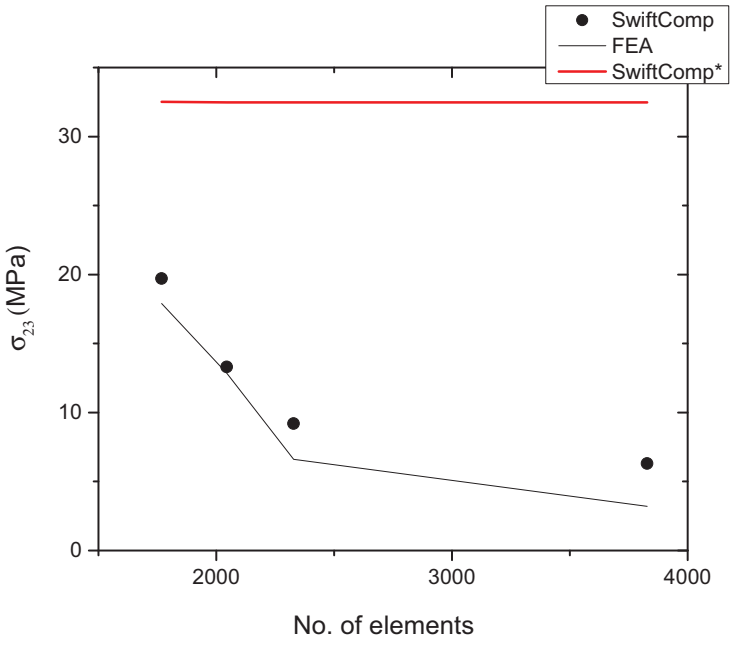

Figure 4.8. Prediction of σ_{23} using the Tsai−Hill failure criterion

SwiftComp*, predicts the initial failure strength without being significantly affected by local mesh refinements as shown in Figure 4.10.

4.1.2 Particle-Reinforced Composite

In this case, let a spherical inclusion with a desired fiber volume fraction be embedded at the center of cuboidal matrix to be used as the SG for a particle-reinforced composite. Let the local Cartesian coordinates be set at the center of sphere. The material properties of fiber and the matrix listed in the Table 4.1 (type 2) are used here by assuming that the particle takes the properties of the fiber. For the mean field approaches (MT and DI), an in-built model in DIGIMAT is used, and for GMC, an in-built spherical particle-reinforced model with 343 elements, in MAC/GMC4.0 is used. Further refining of the mesh does not have any significant improvement on the outputs of GMC. The current version of MAC/GMC 4.0 does not support 3D analysis for HFGMC, thus the predictions of HFGMC are omitted for

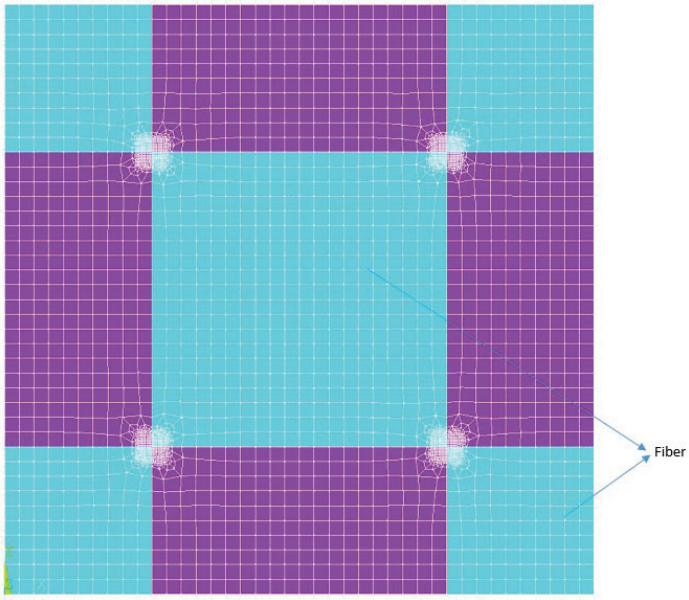

Figure 4.9. SG with contact points

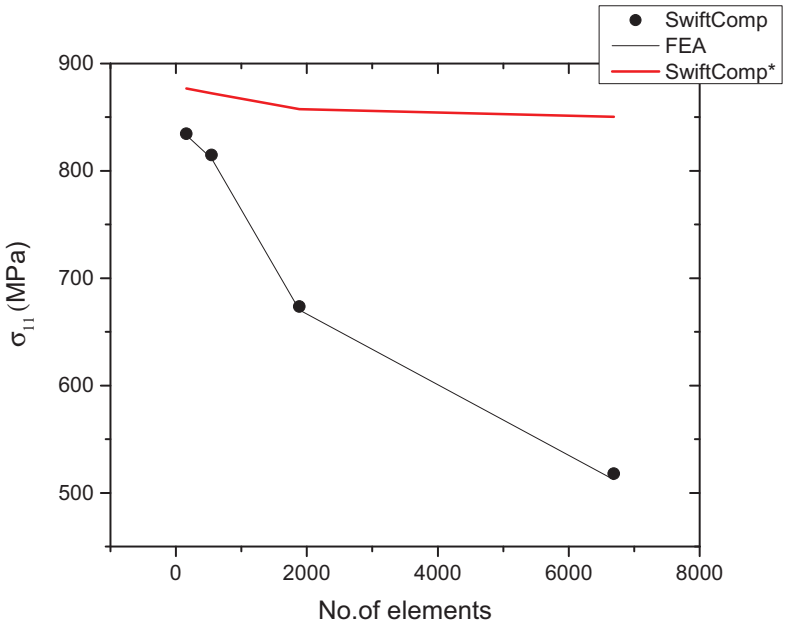

Figure 4.10. Prediction of σ_{11} using the Tsai−Hill failure criterion

all 3D SG cases. A cuboidal SG with 7776 elements is used for SwiftComp and 3D FEA. The results of 3D FEA analysis are obtained by using SOLID95 elements. The initial failure strength of the particle-reinforced composite is predicted using mean field approaches, GMC, SwiftComp, 3D FEA and SwiftComp* for different particle volume fractions.

Table 4.9. Normal failure strength using the maximum normal stress failure criterion

Vof (%)	MT	DI	GMC	SwiftComp*	SwiftComp	3D FEA
10	90.00	91.00	42.50	40.90	39.02	39.20
20	96.96	99.96	36.00	35.87	33.89	33.63
40	109.96	127.47	29.10	23.64	21.76	21.89
50	116.51	148.81	24.40	14.30	12.02	11.28

For maximum normal stress failure criterion, Table 4.9 shows that mean field approaches significantly overestimate the normal failure strength of the particle-reinforced composite approximately by more than 9 times compared with 3D FEA for 50% particle volume. GMC also significantly overpredicts compared with 3D FEA, while SwiftComp shows an excellent agreement. The prediction using the nonlocal approach, SwiftComp*, is also observed to be greater than SwiftComp and 3D FEA, which shows the presence of higher local field gradient in the matrix. For the Tsai-Hill failure criteria, Table 4.10, the mean field approaches significantly overpredict the normal failure strength of the composite approximately by more than 4 to 5 times, particularly for large particle volume fraction. GMC slightly overpredicts compared to 3D FEA using the Tsai-Hill failure criterion while SwiftComp shows excellent agreements. It is noticed that as particle volume increases, the initial failure strength also decreases for GMC, SwiftComp, 3D FEA and SwiftComp* for both maximum stress and Tsai-Hill failure criteria. This is due to the fact that as particle size increases, the stress gradient also increases which may lead to the failure of the composite. However, this is not true for the mean field approaches, because the approaches are inherently incapable of predicting the local stress gradients which mainly contribute to the failure of the composite. The overprediction of GMC might be due to that fact that GMC does not accurately recover the local stress field [4, 5]. The prediction of SwiftComp* for the Tsai-Hill failure criterion appears to be greater than SwiftComp and 3D FEA compared to the maximum stress failure criterion. This indicates that there may be higher multiaxial stress state in the composite due to the interactions between the particle and the matrix.

The initial failure envelope, for multidirectional loading condition, is also generated using the maximum normal stress failure criterion. Figure 4.11 shows that GMC significantly overestimates the initial failure envelope while SwiftComp shows an excellent agreement with 3D FEA. GMC provides a better estimate for the initial failure envelope using the Tsai-Hill failure criterion as shown in Figure 4.12 in comparison to its own predictions using the maximum normal stress failure criterion.

Table 4.10. Normal failure strength of particle-reinforced composite using the Tsai-Hill failure criterion

Vof (%)	MT (MPa)	DI (MPa)	GMC (MPa)	SwiftComp* (MPa)	SwiftComp (MPa)	3D FEA (MPa)
10	91.80	92.91	47.00	48.02	46.50	45.54
20	100.41	104.32	42.50	41.96	39.97	40.12
40	117.84	138.23	36.50	39.17	34.67	34.88
50	126.98	164.48	31.20	29.00	24.89	23.53

The predictions of SwiftComp* are observed to be slightly greater than the predictions of SwiftComp and 3D FEA.

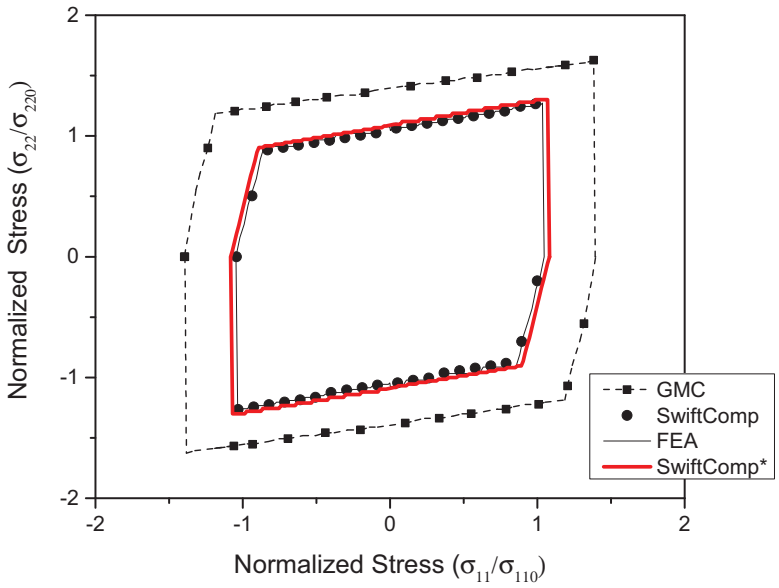

Figure 4.11. Initial failure envelope for normal multidirectional loading condition (maximum normal stress failure criterion for 40% vof)

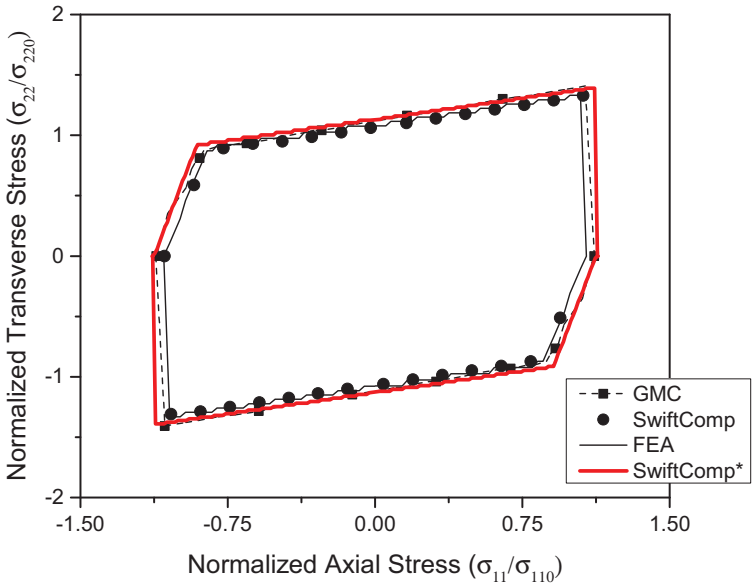

Figure 4.12. Initial failure envelope for normal multidirectional loading condition (Tsai-Hill failure criterion for 40% vof)

4.1.3 Discontinuous Fiber-Reinforced Composite

Two variants of discontinuous fiber-reinforced composites are considered for predicting the initial failure strength of the composite. The first one is an aligned-regular array, where all the fibers are arranged in an aligned pattern. The second one is an aligned-staggered array, where fibers are arranged in an offset pattern. To generate the SG, first, let a quarter of circular fiber be embedded at the two opposite corners of a rectangular shape SG. Let the SG be symmetric with respect to its width and height. This arrangement produces rectangular shape array with circular fiber at the center and quarter circular fibers at the four corners of the SG as shown in Figures 4.13 and 4.16. Second, let the rectangular area of the SG be generated based on the common relation, $a = \beta b$, where a is the width and b the height of the SG and $\beta = \sqrt{3}$ for hexagonal array. Moreover, let the local Cartesian coordinate be introduced as $y = (y_1, y_2, y_3)$ at the center of SG, where y_1 is defined

in the fiber direction. The fibers are generally shorter compared to the SG in y_1 direction. For the detailed geometric constructions of discontinuous fiber-reinforced composites, interested reader may refer to Ref. [159]. In this failure analysis, the fiber volume fraction and fiber aspect ratio (length/diamater) are assumed to be 40% and 5, respectively. For 3D FEA, the SG is first modeled using plane element (Mesh200) in 2D model and then, the corresponding 3D model is generated by extrusion of the 2D model based on the type of materials in SG. SwiftComp uses the mesh used for 3D FEA. The failure analysis is conducted using material properties listed in Table 4.1 (type 2) for both types of discontinuous fiber-reinforced composites.

Aligned-Regular Array

For this example, a $3 \times 44 \times 42$ (y_1, y_2, y_3) subcell grid is used for GMC, and 20-noded elements are used for SwiftComp and 3D FEA. GMC and 3D FEA have 5,544 and 39,600 elements, respectively. The large difference in the element numbers is due to the modeling nature of SG for GMC: it may have only three elements in the y_1 direction and further refining of the mesh in this direction does not improve the output of GMC. SwiftComp and 3D FEA have equal number of elements. Figure 4.13 shows the SG of SwiftComp and 3D FEA. The initial failure prediction of the composite is conducted using various failure criteria and loading conditions. Table 4.11 indicates that GMC underestimates the axial failure strength for the maximum normal stress and Tsai-Hill failure criteria compared with the prediction of SwiftComp and 3D FEA. GMC also shows poor agreement for transverse failure strength using maximum normal stress criterion as shown in Table 4.12. However, the transverse failure predictions of GMC show good agreement for the Tsai-Hill failure criterion. The predictions of SwiftComp agree with the results of 3D FEA for both axial and transverse loading conditions using both failure criteria, except for the deviation of normal failure strain, see Tables 4.11 and 4.12. However, SwiftComp can produce both the axial and transverse normal failure strains equivalent to 3D FEA

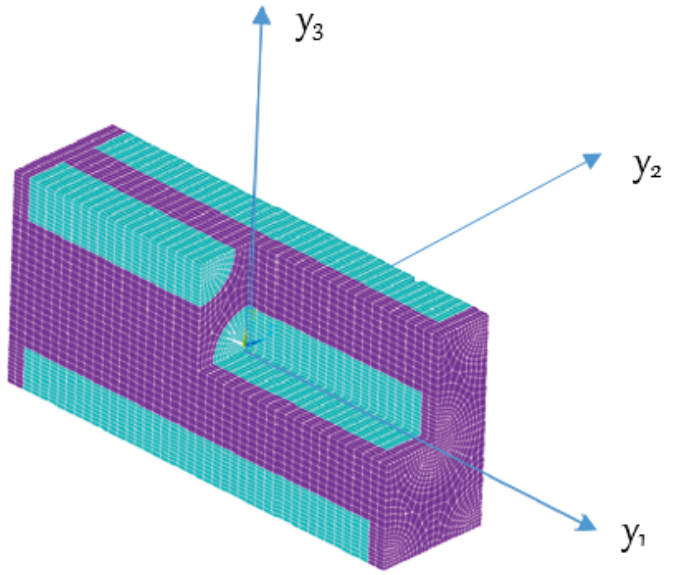

Figure 4.13. SG of an aligned regular array discontinuous fiber-reinforced composite

if maximum principal strain is employed in 3D FEA. The prediction of SwiftComp* shows larger deviation from SwiftComp and 3D FEA for all failure criteria compared with continuous fiber-reinforced composites. This shows that there is larger local field gradients in the constituent of discontinuous fiber-reinforced composites in all three loading directions. It is also noted that the prediction of maximum normal stress failure criteria is found to be conservative compared with other failure criteria.

Table 4.11. Axial aligned regular array discontinuous fiber-reinforced composite

	Axial failure strength strength			
Approach	GMC	SwiftComp*	SwiftComp	3D FEA
Max. Normal Stress (MPa)	41.28	55.51	49.59	50.09
Tsai-Hill (MPa)	50.92	86.93	77.66	78.30
Max. Normal Strain	0.0025	0.0031	0.0021	0.0016

Figures 4.14-4.15 show that initial failure envelopes, using different loading conditions. GMC poorly predicts the failure strength for both maximum normal stress

Table 4.12. Transverse failure strength of aligned regular array discontinuous fiber-reinforced composite

	Transverse strength 2				Transverse strength 3			
Failure Criteria	GMC	SwiftComp*	SwiftComp	3D FEA	GMC	SwiftComp*	SwiftComp	3D FEA
Max.Normal Stress (MPa)	63.70	66.78	56.65	57.42	49.50	51.41	45.69	44.38
Tsai-Hill (MPa)	58.10	77.83	58.15	59.00	57.54	60.03	56.65	57.62
Max. Normal Strain	0.0087	0.0075	0.0045	0.0035	0.0062	0.0063	0.0042	0.0032

and Tsai-Hill failure criteria. On the contrary, the predictions of SwiftComp show very good agreement with 3D FEA for both failure criteria and loading conditions. The poor predictions of GMC might be due to its poor capability of predicting local fields that results from the lack of axial-shear coupling. The predictions of SwiftComp* for bidirectional loading are also observed to be greater than other approaches, which result from higher local stress gradients in the constituents of the composite.

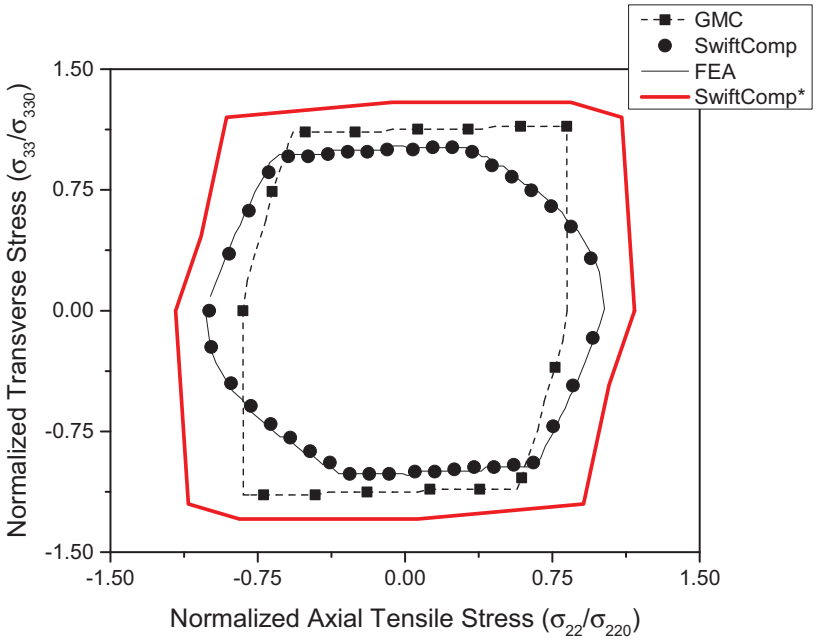

Figure 4.14. Initial failure envelope for axial and transverse loading (Maximum normal stress failure criterion for 40% vof).

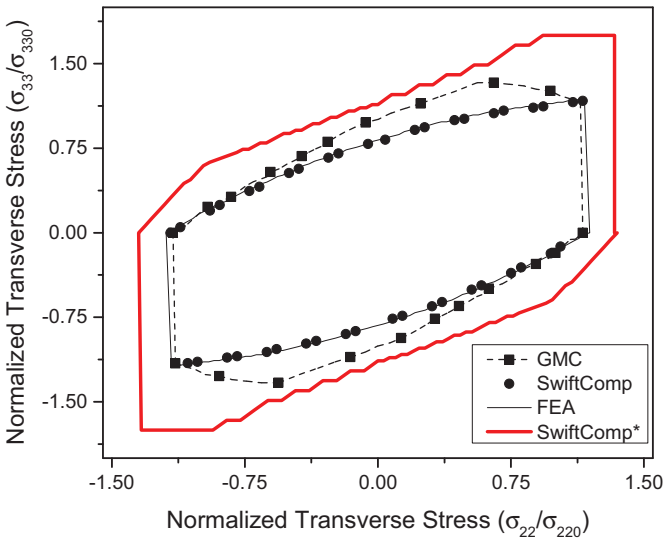

Figure 4.15. Initial failure envelope for axial and transverse loading (Tsai-Hill failure criterion for 40% vof).

The axial shear strengths S_{12} and S_{13}, and the transverse shear strength S_{23} are also analyzed using Tsai-Hill failure criterion. Table 4.13 shows that GMC predicts well for S_{12} but poorly estimates S_{13} and S_{23} compared with SwiftComp and 3D FEA. The predictions of SwiftComp* are found to be greater than the predictions of SwiftComp and 3D FEA. This result is expected due to local stress disturbances in the constitutes of the composite.

Table 4.13. Axial and transverse shear failure strengths of aligned regular array discontinuous fiber-reinforced composite (40% of vof).

Approaches	S_{12}	S_{13}	S_{23}
GMC	26.19	33.12	38.80
SwiftComp*	27.39	24.29	32.42
SwiftComp	27.02	19.83	20.80
FEA	27.39	19.95	20.93

Aligned-Staggered Array

Aligned staggered array type of discontinuous fiber-reinforced composite is similar to the regular aligned array but, in this case, the fibers in the SG are arranged in a staggered pattern, i.e., fibers overlap within the SG. Let 76% of fiber length overlaps within the SG for this analysis. A $6 \times 42 \times 42$ (y_1, y_2, y_3) subcell grid is used for GMC, 34,608 20-noded elements are used for SwiftComp and 3D FEA. The SG of FEA/SwiftComp is shown in Figure 4.16. GMC has a similar SG with cuboidal meshing pattern.

The predictions of initial failure strengths are performed using different failure criteria. Table 4.14 indicates that GMC insufficiently approximates the axial failure strength using all failure criteria. The predictions of SwiftComp unexpectedly show much deviation from 3D FEA although they are better than GMC. This difference may be due to the difference between the maximum normal strain and maximum principal strain. For this case, it shows their the difference of the two strains is higher. Failure is evaluated using principal strain in SwiftComp and maximum normal strain in 3D FEA. The predictions of GMC for the transverse failure strength show relatively better agreements with 3D FEA. While the prediction of SwiftComp shows an excellent agreement for transverse failure strength as shown in Table 4.15. The prediction of SwiftComp* is significantly greater than the predictions of SwiftComp and 3D FEA, which show significant local stress variations in each constituent of the composite.

Table 4.14. Axial and transverse failure strengths of aligned staggered array discontinuous fiber-reinforced composite

	Axial strength 1			
Failure Criteria	GMC	SwiftComp*	SwiftComp	FEA
Max. Normal Stress (MPa)	49.50	97.61	67.96	61.56
Tsai-Hill (MPa)	59.40	115.11	87.36	79.81
Max. Normal Strain	0.0046	0.0039	0.0027	0.0018

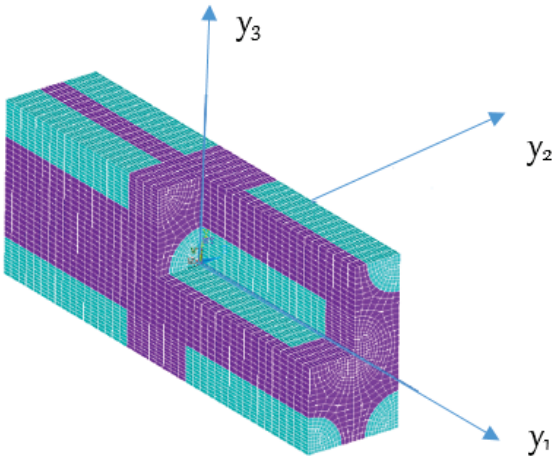

Figure 4.16. SG of aligned staggered array discontinuous fiber-reinforced composite.

Table 4.15. Transverse failure strengths of aligned staggered array discontinuous fiber-reinforced composite

	Transverse strength 2				Transverse strength 3			
Approach	GMC	SwiftComp*	SwiftComp	FEA	GMC	SwiftComp*	SwiftComp	FEA
Max. Normal Stress (MPa)	53.35	60.58	47.29	47.50	48.00	60.92	43.97	44.50
Tsai-Hill (MPa)	61.38	76.99	56.40	57.66	56.84	63.9	57.52	57.60
Max. Normal Strain	0.0073	0.0060	0.0041	0.0034	0.0058	0.0055	0.0052	0.0039

The initial failure envelop is also generated for combined loading conditions. Figures 4.17 and 4.18 show that GMC well predicts the initial failure envelopes for both cases except for the large deviation for larger values of opposing loads for maximum normal stress failure criterion. The predictions of SwiftComp agree well with 3D FEA, while the predictions of SwiftComp* are greater than the predictions of SwiftComp and 3D FEA for all the cases. This is due to the higher local stress gradients in each constituent of discontinuous fiber-reinforced composites particularly in the axial direction.

The shear failure strength prediction of GMC, Table 4.16, is observed to be overpredicted using Tsai-Hill failure criterion compared with SwiftComp and 3D FEA, for S_{13} and S_{23}, while it slightly underpredicts for S_{12}. On the contrary, SwiftComp

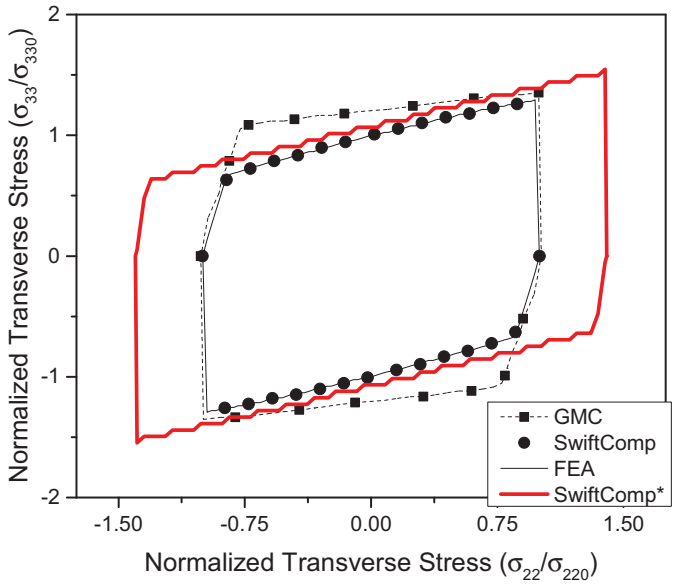

Figure 4.17. Initial failure envelope for transverse loading (maximum normal stress criteria vof 40%)

shows excellent agreements with the predictions of 3D FEA for axial shear failure strength. However, SwiftComp* overpredict all the transverse shear failure strengths approximately by 40% compared with 3D FEA. This shows the extent of the variations of local fields in each constituent of the composite.

Table 4.16. Shear failure strength of aligned staggered array discontinuous fiber-reinforced composite using the Tsai-Hill failure criterion (40% of vof)

Approaches	S_{12}	S_{13}	S_{23}
GMC	29.70	32.67	35.28
SwiftComp*	31.76	31.55	31.45
SwiftComp	24.51	23.74	22.93
FEA	24.99	24.59	22.25

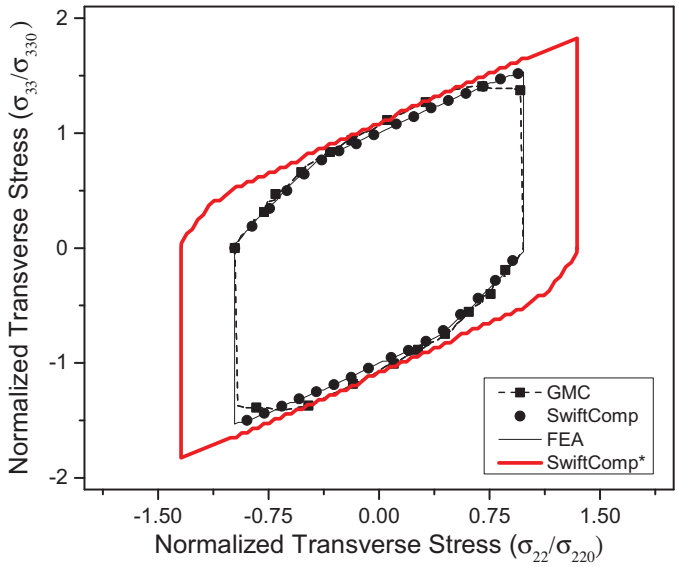

Figure 4.18. Initial failure envelope for transverse loading (Tsai-Hill vof 40%)

4.1.4 Woven Composite

A woven composite can be modeled as depicted in Figure 4.19. The ellipsoidal cross-section of major axis radius, c, and minor axis radius, $\frac{c}{4}$, elliptical curvature radius, $r = 2.5c$, and also matrix thickness of $\frac{c}{8}$ are assumed on the top and bottom of the side of the SG. The ellipsoidal cross-section center to center distance is $2c$. The overall SG length, width and height are $4c$, $4c$ and $\frac{5c}{4}$, respectively. In this failure analysis, the constant c is assumed to be 2. GMC uses the same shape of SG with a cuboidal meshing pattern. A single-step GMC approach is employed for this analysis. A 64 subcell grid is used for GMC. The basic type of woven microstructure is used from DIGIMAT for mean field approaches (MT and DI). The SG of 3D FEA/SwiftComp is meshed to have $18,432$ elements. It is obvious to see large element difference between the GMC and FEA/SwiftComp. This is because GMC inherently uses only cuboidal element type in the SG and further meshing of the subcell does not improve accuracy for the predicted values. The warp and weft are assumed to have the material

properties of the fibers listed in Table 4.1 under type 1 and type 2, respectively. The matrix of woven is assumed to have the matrix in type 2 of the material properties. The volumes of warp, weft and the matrix are obtained to be 25.95%, 25.95% and 48.10%, respectively.

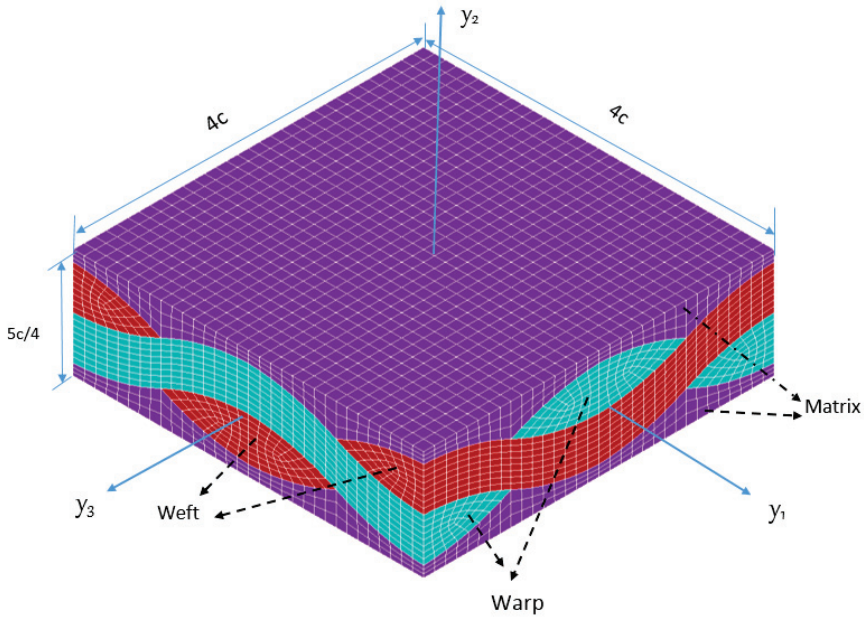

Figure 4.19. SG of woven composite)

Table 4.17 shows that the mean field approaches significantly overpredict the failure strength of the composite in directions 2 (σ_{22}) and 3 (σ_{33}) using maximum normal stress, Tsai-Hill and maximum normal strain failure criteria. Conversely, the mean field approaches, underpredict the failure strength in direction 1 (σ_{11}) for maximum normal stress and Tsai-Hill failure criteria. Similarly, GMC also significantly overestimates the failure strengths for all failure criteria except for the failure strength in direction 3 (σ_{33}), which shows close predictions for Tsai-Hill failure criterion compared with SwiftComp and 3D FEA. On the contrary, SwiftComp shows relatively good agreements for both Tsai-Hill and maximum normal strain failure criteria. The differences of SwiftComp and 3D FEA may be due to the failure evaluating method, where SwiftComp uses principal stress while 3D FEA adopts

maximum normal stress. SwiftComp can produce the failure normal strains of the woven composite that agree well with the predictions of 3D FEA, if the principal strain is used for evaluation of failure. However, as shown in Table 4.18, the predicted output using maximum strain is much lower than the predictions of principal strain using SwiftComp. The predictions of SwiftComp* are significantly greater than the predictions of SwiftComp and 3D FEA, which indicates higher local field gradient in the composite.

Table 4.17. Failure strength of woven composite

	Maximum normal stress failure criterion			Tsai-Hill failure criterion		
Approach	$\sigma_{11}(MPa)$	$\sigma_{22}(MPa)$	$\sigma_{33}(MPa)$	σ_{11} (MPa)	σ_{22} (MPa)	σ_{33} (MPa)
MT	465.41	103.57	465.41	554.01	162.35	592.52
DI	492.50	140.92	592.52	592.52	204.55	592.52
GMC	1046.64	83.30	1046.64	1094.40	159.60	194.40
SwiftComp*	867.17	60.10	285.60	827.22	98.5	268.19
SwiftComp	728.24	51.97	225.10	769.81	88.60	209.18
FEA	776.61	53.00	248.40	774.50	89.00	211.51

Table 4.18. Failure strain for woven composite

	Maximum normal strain failure criterion		
Approach	strain ϵ_{11}	strain ϵ_{22}	strain ϵ_{33}
MT	0.0131	0.0130	0.0131
DI	0.0133	0.0132	0.0133
GMC	0.0193	0.0101	0.0193
SwiftComp*	0.0125	0.0028	0.0036
SwiftComp	0.0115	0.0024	0.0028
FEA	0.0051	0.0024	0.0018

The initial failure envelope for transverse loading, i.e., σ_{22} and σ_{33}, as depicted in Figure 4.20, shows that GMC significantly overpredicts the initial failure envelope using maximum normal stress failure criterion approximately by more than 54%. Moreover, Figure 4.21 shows that the prediction of GMC overpredicts the initial failure envelope compared with 3D FEA and SwiftComp approximately by more than 10% for Tsai-Hill failure criterion.

This failure analysis shows significant deviations of mean field approaches and GMC from SwiftComp and 3D FEA compared to other examples. This indicates that the average local fields in the composite are not good enough to approximate the local field variations in a complex microstructure. The capability of local field prediction is once again found to be crucial for analyzing the initiation of failure at micro-scale level, particularly, for complex microstructures like a woven composite. The inability of GMC for prediction of failure strength may also be due to the cuboidal shape of the subcell as well as its inherent lack of axial-shear coupling effect. The cuboidal shape may also affect GMC not to accurately recover the local fields along the wave of the warp, the weft and the matrix of the composite. In general, it is noticeable that SwiftComp can predict the initial failure envelope of woven composites equivalent to 3D FEA.

The predictions of SwiftComp* are significantly greater than the predictions of SwiftComp and 3D FEA. This is mainly due to the complex geometry of the microstructures, the local fields are highly variable due to the interactions of constituents with different properties.

4.2 Imperfect Interface Analysis

A constitutive model that allows a linear traction-displacement model is incorporated into SwiftComp to analyze the effect of imperfect interface on the effective properties and initial failure strength of heterogeneous materials. This analysis is performed using several representative examples of heterogeneous

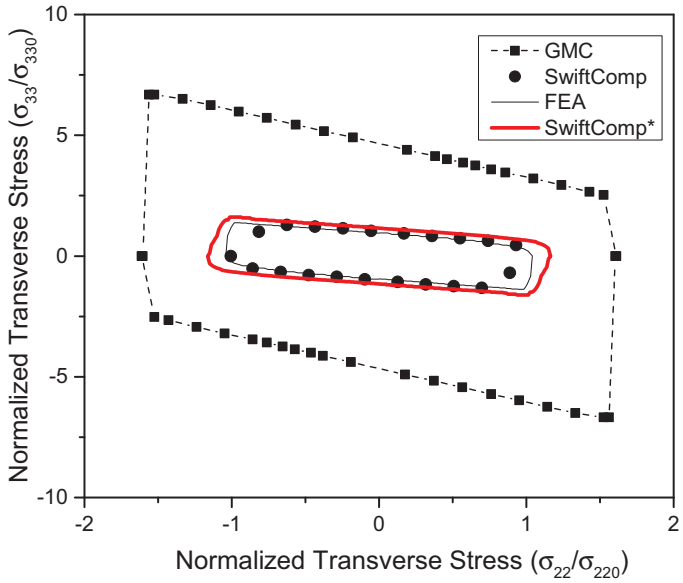

Figure 4.20. Initial failure envelope for σ_{22} and σ_{33} (maximum normal stress failure criterion)

materials. The predictions of SwiftComp are compared using exact solutions for binary/layered composite, the upper and lower bounds predictions in Ref. [147] for particle-reinforced composite, and 3D FEA for other examples. The results of 3D FEA are obtained using interface element (INTER204) in ANSYS 15.1 by employing periodic boundary conditions. The initial failure analyses are also performed using the material properties listed in Table 4.1 (type 2).

4.2.1 Binary Composite

In this section, let the properties of layer 1 and layer 2 be represented by the properties listed in Table 4.1 (type 2), respectively. For 3D FEA, the SG is meshed to have 6400 elements (ANSYS SOLID95). Let the tangential and normal interfacial stiffness be related as $\bar{D}_{II} = 8\ \bar{D}_I$ and $\bar{D}_{II} = \bar{D}_{III}$. Eq. (3.74) shows the prediction for the longitudinal elastic moduli, E_1 and E_2, are not affected by the interfacial

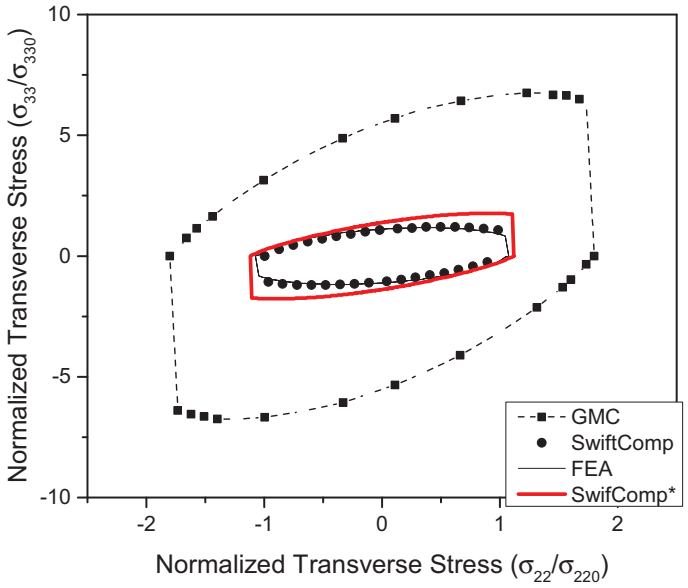

Figure 4.21. Initial failure envelope for σ_{22} and σ_{33} (Tsai-Hill failure criterion)

stiffness. Similarly, all Poisson's ratios $(\nu_{12}, \nu_{13}, \nu_{23})$ are not affected by interfacial stiffness, see Eqs. (3.78) and (3.79). Moreover, Eq. (3.75) indicates that G_{12} is independent of interfacial stiffness. The predictions of SwiftComp and 3D FEA, for E_1, E_2, G_{12} and all Poisson's ratios, are also consistent with the predictions of exact solution. However, in Figure 4.22, the predictions of transverse elastic modulus E_3 are significantly affected by the interfacial stiffness $\bar{D}_I$. As the interfacial stiffness increases, the prediction of imperfect interface converges to the predictions obtained using perfect interface assumption. It is also found that interfacial stiffness $\bar{D}_{II}$ and $\bar{D}_{III}$ do not affect the transverse elastic modulus E_3. The predictions of exact solution, SwiftComp and 3D FEA show excellent agreements.

Figure 4.23 shows that the prediction of elastic shear modulus G_{23} is significantly affected by the interfacial stiffness $\bar{D}_{III}$. It is also observed that as interfacial stiffness increases, the prediction of shear modulus G_{23} converges to the prediction of perfect interface. In this case, it is also noted that the interfacial stiffness $\bar{D}_I$ and $\bar{D}_{II}$ do not

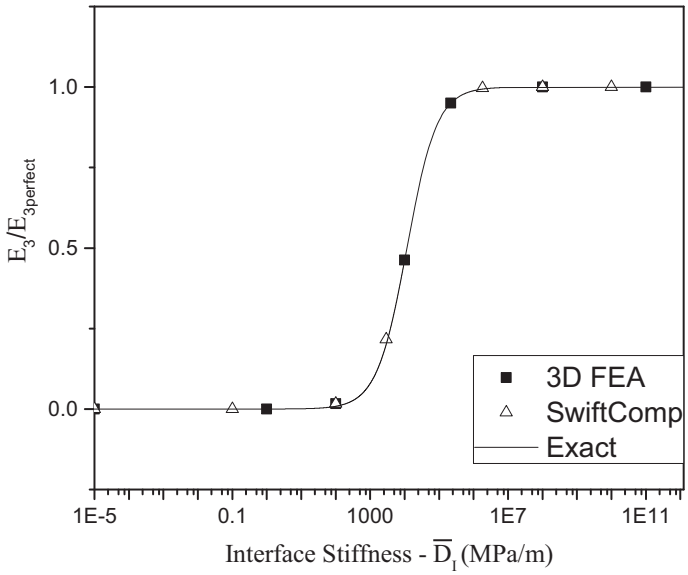

Figure 4.22. Prediction of transverse elastic modulus E_3

affect the prediction of the transverse shear modulus G_{23}. Similarly, in Eq. (3.76), the prediction of shear modulus G_{13} is found to be affected by interfacial stiffness $\bar{D}_{III}$. This prediction is similar to the one obtained for the shear modulus G_{23}. The main difference is that G_{13} is affected by $\bar{D}_{III}$ while G_{23} is by $\bar{D}_{II}$. For both cases, the predictions of exact solutions and 3D FEA show excellent agreement [160].

For more general cases, let the layers exhibit orthotropic or monoclinic properties, obtained by assigning different orientations for material properties listed in Table 4.19. First, let us assume the binary composite be made of two cross plies, [0/90] and also let $\bar{D}_I$ be equal to 0.1 GPa/m, and $\bar{D}_{II} = \bar{D}_{III}$ be equal to 0.8 GPa/m. Table 4.20 shows the predictions of exact solution obtained using Eq. (3.81) and 3D FEA. It shows that exact solution and 3D FEA are in an excellent agreement. Although all the components of effective stiffness matrix except C^*_{66} are affected by interfacial stiffness as shown in Eq. (3.81), the effective compliance matrix of [0/90] is not observed to be affected in a similar way as shown in Eq. (4.1)

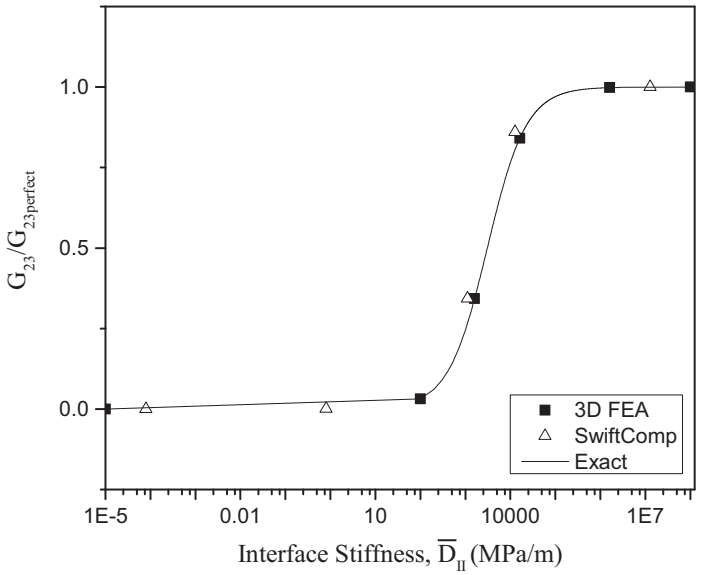

Figure 4.23. Prediction of elastic shear modulus G_{23}

E_1 (GPa)	$E_2 = E_3$ (GPa)	G_{23} (GPa)	$G_{12} = G_{13}$ (GPa)	$\nu_{12} = \nu_{13}$	ν_{23}
255	15	7	15	0.20	0.07

Table 4.19. List of material properties

$$\mathbf{S}^* = \begin{bmatrix} \frac{187}{22485} & -\frac{187}{899437} & \frac{757}{645750} & 0 & 0 & 0 \\ & \frac{187}{22485} & -\frac{757}{645750} & 0 & 0 & 0 \\ & & \frac{1201679}{18081000} + \frac{1}{D_I} & 0 & 0 & 0 \\ & SYMM & & \frac{11}{105} + \frac{10^9}{D_{II}} & 0 & 0 \\ & & & & \frac{11}{105} + \frac{10^9}{D_{III}} & 0 \\ & & & & & \frac{1}{15} \end{bmatrix} 10^{-9}. \tag{4.1}$$

Table 4.20. Effective properties for [0/90] and [±45] layers

Approach	$E_1 = E_2$ (GPa)	E_3 (GPa)	$G_{13} = G_{23}$ (GPa)	G_{12} (GPa)	ν_{12}	$\nu_{13} = \nu_{23}$
[0/90] Laminate						
Exact	120.46	0.09	0.73	15.00	0.025	0.140
3D FEA	120.22	0.08	0.72	15.00	0.025	0.140
3D FEA/Exact*	120.46	15.00	9.54	15.00	0.025	0.140
[±45] Laminate						
Exact	48.26	0.09	0.73	5.87	0.609	0.056
3D FEA	48.14	0.08	0.72	5.85	0.605	0.052
3D FEA/Exact*	48.26	15.00	9.45	5.87	0.609	0.052

* Perfect Interface.

The corresponding stiffness matrix can also be obtained by inverting the compliance matrix, where one can see C^*_{11}, C^*_{22}, C^*_{12}, C^*_{16} and C^*_{26} as function of interfacial stiffness. This is consistent with Eq. (3.81). Eq. (4.1) shows E_3, G_{23}, and G_{13} varies with the interface stiffness $\bar{D}_I$, $\bar{D}_{II}$ and G_{III}, respectively. Similarly, we can also obtain the prediction of [±45] laminate. Table 4.20 also shows the predictions of exact solution for [±45] are in an excellent agreement with the 3D FEA.

The effect of the interfacial stiffness on the failure strength of the binary composite is also analyzed using maximum normal stress and maximum shear stress failure criteria. As it can be seen from the Figures 4.24 and 4.25, it is clear to notice that the failure strength is considerably dependent on the interfacial strength of the composite. Both SwiftComp and 3D FEA show an excellent agreement with exact solutions. For this case, the normal interfacial strength is assumed to be equal to the strength of layer 1. The tangential interfacial strengths are approximated in a similar way that the interfacial stiffnesses are related. This failure analysis shows that the interfacial stiffness mainly controls the failure of the composite, i.e, failure usually initiates at the interface.

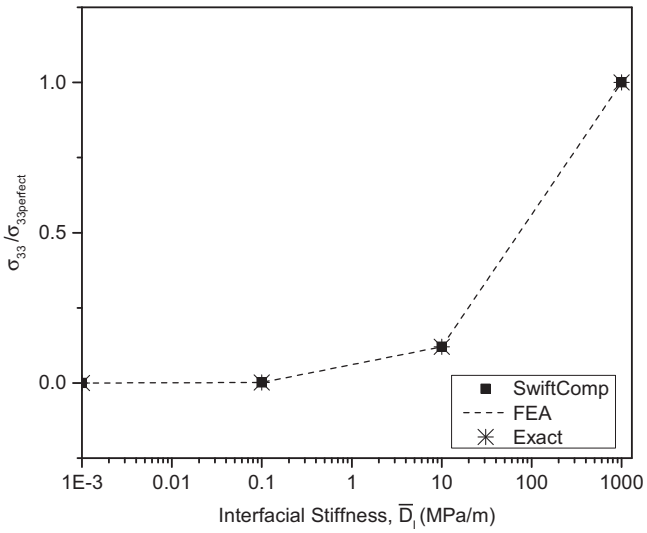

Figure 4.24. Predictions of failure strength σ_{33} using the maximum principal stress failure criterion.

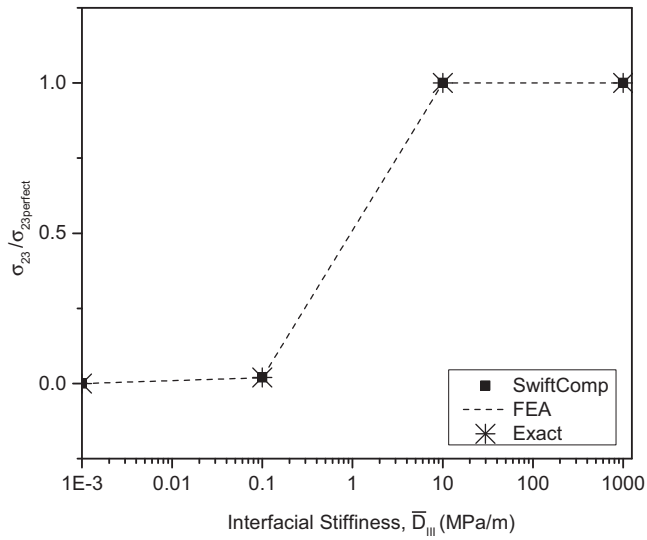

Figure 4.25. Predictions of failure strength σ_{23} using the maximum shear stress failure criterion

4.2.2 Continuous Fiber-Reinforced Composite

For this case, the SG, Figure 4.1, is used to analyze the effect of imperfect interface. The material properties of the fiber and matrix are listed in the Table 4.21. In this analysis, the fiber volume fraction is assumed to be 40%. The interfacial debonding

Table 4.21. Material properties for imperfect interface analysis.

Mat	E (GPa)	ν
Fiber	379.3	0.10
Matrix	68.3	0.30

can happen in three possible directions at fiber and matrix interface: 1) normal to the contacting surface that corresponds to mode I failure with the interface stiffness $\bar{D}_I$; 2) tangent to the interface parallel to the fiber direction which corresponds to the mode II failure with the interface stiffness $\bar{D}_{II}$; and 3) tangent to the interface and normal to the fiber directions that corresponds to mode III failure with the interface stiffness $\bar{D}_{III}$. These modes of failure are used to analyze the effect of imperfect interface on the elastic effective properties of the composite. Let the interface stiffness be related to each other as, i.e, $\bar{D}_{II} = 5\bar{D}_I$ and $\bar{D}_{II} = \bar{D}_{III}$.

The predictions of this analysis show that the axial effective elastic modulus E_1 is negligibly affected by the interfacial stiffness (not shown here), while the effective elastic modulus E_2 is significantly dependent on the normal interfacial stiffness $\bar{D}_I$ as depicted in Figure 4.26. It is also noticed that the interfacial stiffness $\bar{D}_{II}$ does not influence the predictions of transverse elastic modulus. However, Figure 4.27 shows that the prediction of effective transverse shear modulus G_{23} is found to be highly affected by the interfacial stiffness $\bar{D}_{III}$.

Moreover, it is found to be important to analyze the influence of the interfacial stiffness on the effective Poisson's ratio of the composite. In Figure 4.28, the effective Poisson's ratio ν_{12} is observed to be larger for imperfect interface with negligible interfacial stiffness. This shows that the weaker the interface is, the larger the

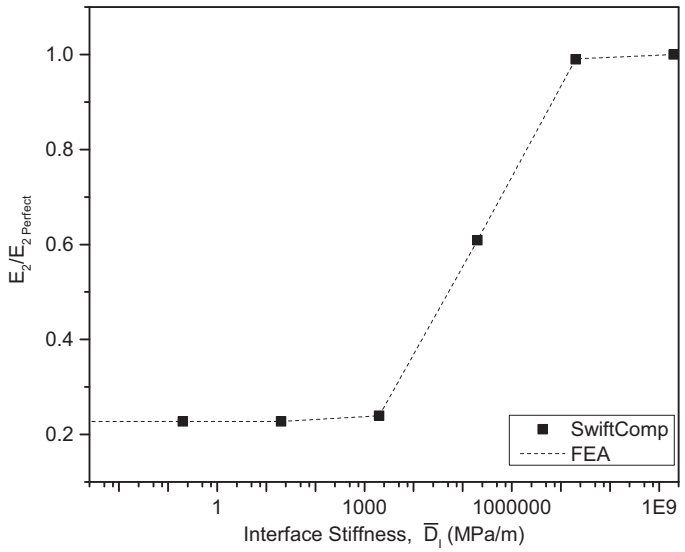

Figure 4.26. Predictions of effective modulus E_2.

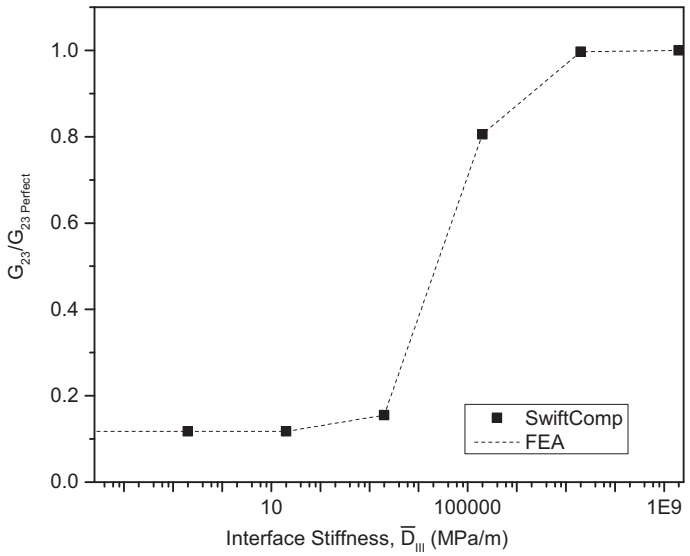

Figure 4.27. Predictions of effective shear modulus G_{23}.

global strain in the transverse direction. For instance, for longitudinal load along the fiber direction, both global axial strain ε_{11} and global transverse strain ε_{22} are slightly affected. This results in the larger Poisson's ratio ν_{12} $(-\frac{\varepsilon_{22}}{\varepsilon_{11}})$. However, as the interfacial stiffness increases, the effective Poisson's ratio ν_{12}, converges to the perfect interface predictions. Conversely, the transverse effective Poisson's ratio ν_{23} is highly influenced by the interfacial stiffness. For example, for lower interfacial stiffness, let a small transverse global load be applied on the SG. Then, the global strain ε_{22} is significantly affected, i.e., the strain increases, in the direction of the load while the strain in the unloaded direction ε_{33} is slightly affected. This results in reducing effective Poisson's ratio ν_{23}. As the interfacial stiffness increases, the ratio ε_{33} to ε_{22}, i.e., ν_{23}, further decreases. This is because the increase of the stiffness decreases the strains in both directions, but the extent of decrease in ε_{33} is much greater than that of ε_{22} which in turn leads to considerable decrease of effective transverse Poisson's ratio ν_{23} as depicted in Figure 4.28. Further increase in the interfacial stiffness negligibly affect ε_{33} while ε_{22} further decreases. Consequently, this results in increasing the effective transverse Poisson's ratio ν_{23} and finally it converges to the prediction of perfect interface. The predictions of SwiftComp and 3D FEA are in a perfect agreement for both axial and transverse Poisson's ratios.

Finally, the initial failure strength of the continuous fiber-reinforced composite is analyzed using the material properties listed in Table 4.1 (type 2). For all interfacial failure analysis, the normal interfacial strength is approximated to be the same as the strength of the matrix. The other interfacial strengths can be obtained using the normal interfacial strengths based on the interfacial stiffness relationship. It is learned that the failure strength in axial direction is negligibly affected due to interfacial stiffness, while the failure in the transverse direction is significantly dependent on the interfacial stiffness as depicted in Figures 4.29 and 4.30 for the maximum normal stress and Tsai-Hill failure criteria, respectively. In this case, the interface is assumed to undergo negligible damage. Figure 4.31 also shows that the transverse shear

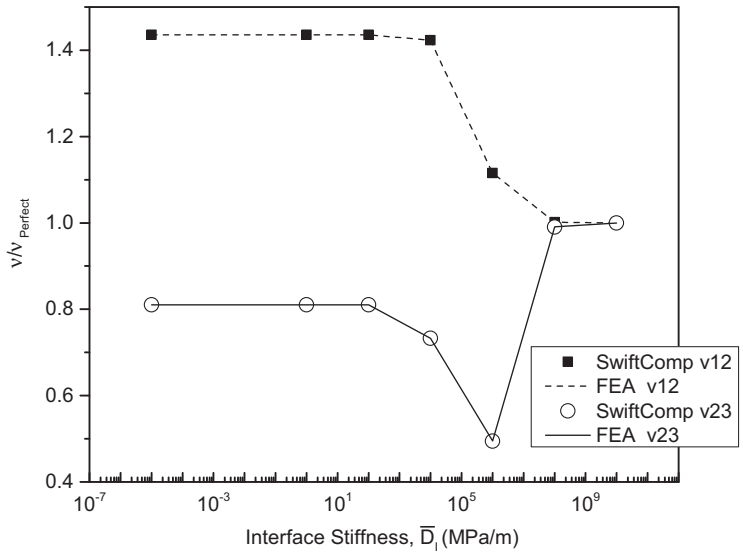

Figure 4.28. Predictions of effective Poisson's ratio ν_{12} and ν_{23}.

failure strength is dependent on the interfacial stiffness. This analysis shows that the interfacial stiffness can significantly affect the strength of the composite.

4.2.3 Particle-Reinforced Composite

The SG described for failure analysis of particle-reinforced composite is assumed for this case as well. The inclusion particle and the matrix are assumed to have an elastic modulus 703.45 GPa and 206.94 GPa, respectively. The corresponding Poisson's ratios are 0.2199 and 0.2999, respectively. The interface stiffness, in this case, is assumed to have a relation, $\bar{D}_I = 5\bar{D}_{II}$, and $\bar{D}_{II} = \bar{D}_{III}$, and $\frac{G_2}{a\bar{D}_{II}} = 10$, where G_2 is the shear modulus of the matrix, and a is the radius of the sphere. The elastic effective properties are predicted using upper and lower bounds in Ref. [147]. The upper and lower bounds for the effective elastic modulus, E, are found to be 187.86 GPa and 61.6 GPa, respectively. Similarly, for the effective shear modulus, G, the upper and the lower bounds are predicted to be 75.71 GPa and 22.50 GPa,

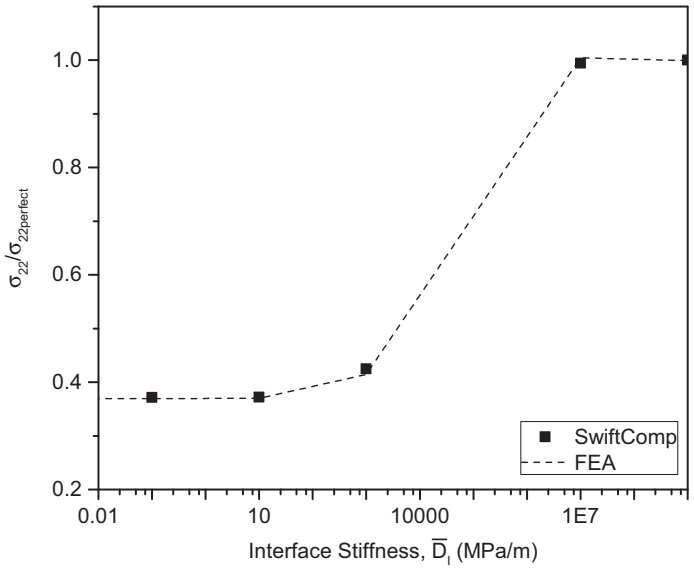

Figure 4.29. Predictions of failure strength for σ_{22} using the maximum normal stress failure criterion.

respectively. The current predictions using SwiftComp and 3D FEA are 140.85 GPa and 142.63 GPa for effective elastic modulus, respectively. SwiftComp and 3D FEA also predict the effective shear modulus to be 51.89 GPa and 55.61 GPa, respectively. The slight deviation of SwiftComp from 3D FEA is due to the limitation of the adopted interface element (INTER204) that can not properly capture the change in effective shear G_{12} due to imperfect interface. It appears that the prediction of SwiftComp and 3D FEA for both elastic and shear moduli are within the proposed upper and lower bound values. In general, the predictions of SwiftComp and 3D FEA compared with the upper and lower bounds of elastic moduli are analyzed for various interfacial stiffness. Figures 4.32 and 4.33 show that the prediction of both effective elastic and shear moduli are observed to be much closer to the upper bounds.

The lower bound predictions of Hashin in Ref. [147] are close to zero for small interfacial stiffness. This does not seem reasonable. For instance, for completely debonded case, which simulates no interfacial stiffness, the prediction of effective the

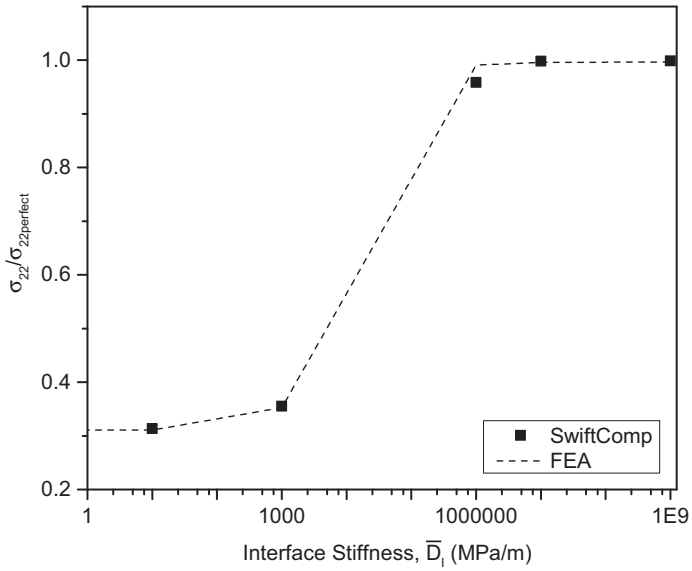

Figure 4.30. Predictions of failure strength for σ_{22} using the Tsai-Hill failure criterion.

longitudinal and shear moduli should be closer to the properties of cuboidal matrix with void, i.e., the void is equal to the volume of the particle.

The failure strength of the particle-reinforced composite is also analyzed for different interfacial stiffnesses. The interfacial strength is approximated in the same way as continuous fiber-reinforced composite. Figure 4.34 indicates that the predictions of failure strength using Tsai-Hill failure criterion show that the failure strength of the composite can be compromised due to the imperfect interface. It may lose up to 25% of its original strength with prefect interface. The deviations of the prediction of SwiftComp and 3D FEA for lower interface stiffness may be due to the effect of the interfacial stiffness, $\bar{D}_{II}$, that is not well captured using INTER204 elements in ANSYS.

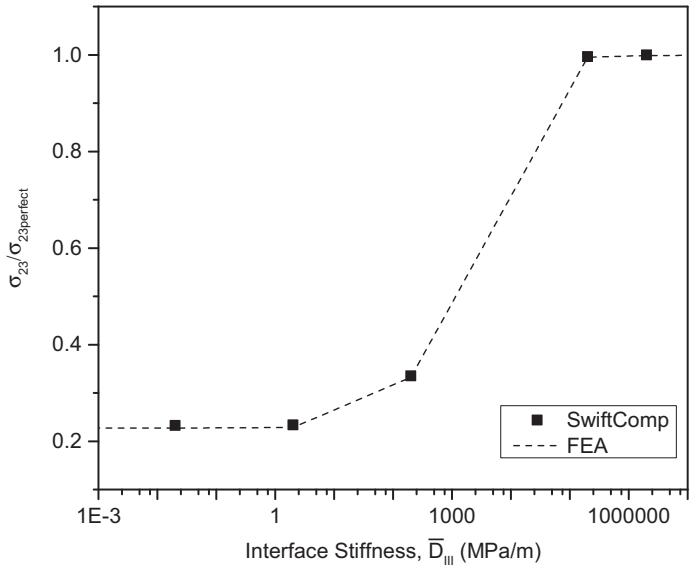

Figure 4.31. Predictions of failure strength for σ_{23} using the Tsai-Hill failure criterion.

4.2.4 Discontinuous Fiber-Reinforced Composite

The SG in Figures 4.13 and 4.16 will also be used for imperfect interface analysis. The material properties for both types of discontinuous fiber-reinforced composites are listed in Table 4.22. In both examples, it is assumed that the interface undergoes infinitesimal displacement jumps.

Table 4.22. Material property (Ref. [159]).

Mat	E (GPa)	ν
Fiber	300	0.17
Matrix	10	0.33

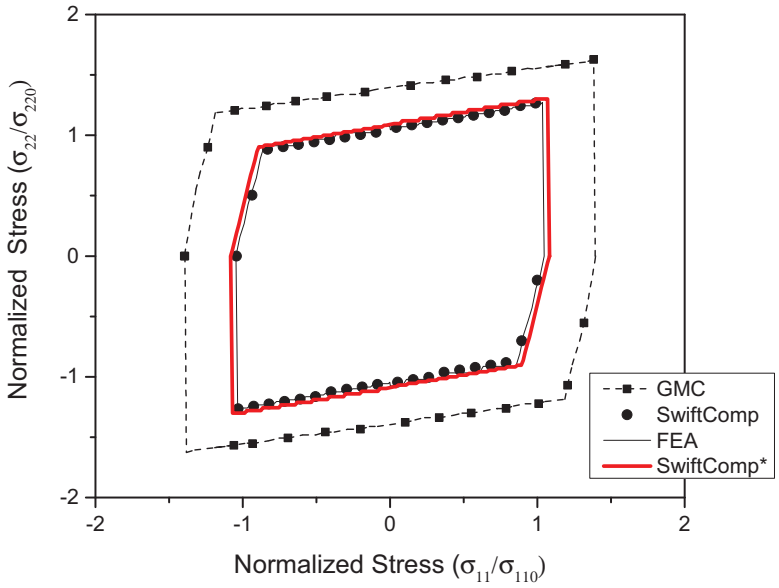

Figure 4.32. Predictions of effective elastic modulus E.

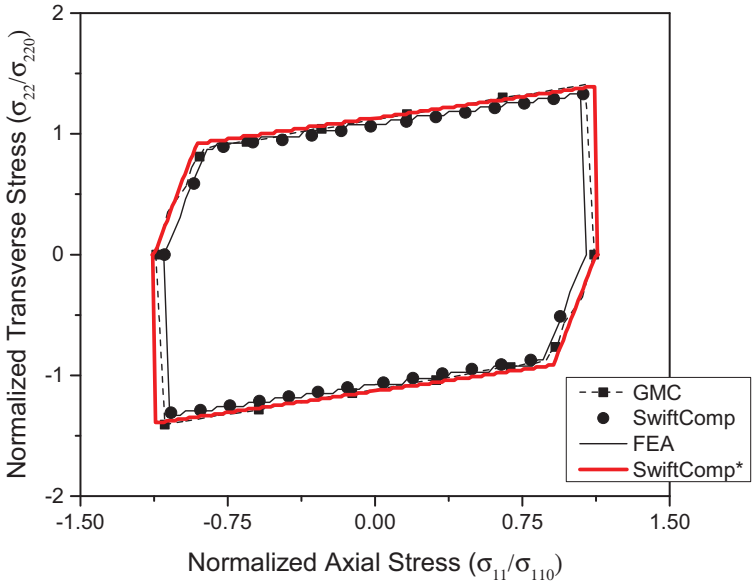

Figure 4.33. Predictions of effective shear modulus G.

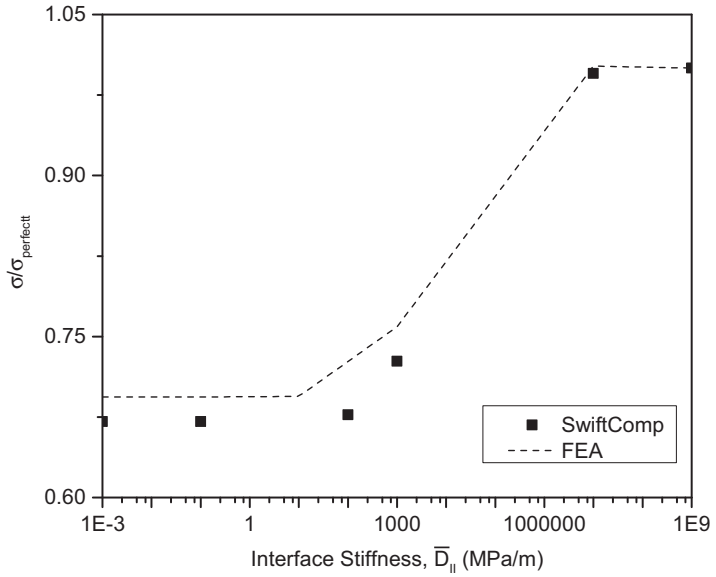

Figure 4.34. Predictions of failure strength of particle-reinforced composite σ using the Tsai-Hill failure criterion.

Aligned-Regular Array

The SG of SwiftComp and FEA is shown in Figure 4.13. In this analysis, 20-noded elements are used for SwiftComp and 3D FEA with 10,624 elements. Assume $\bar{D}_{II} = 5\bar{D}_I$ and $\bar{D}_{II} = \bar{D}_{III}$. The predictions of effective properties with various interfacial stiffnesses are performed using SwiftComp and 3D FEA. Figure 4.35 shows that the predictions of elastic modulus E_1 using SwiftComp show a slight deviation from 3D FEA. This deviation may be due to the interfacial stiffness in the model II direction, that the current interfacial element does not rigourously capture. In another analysis, Figures 4.36 and 4.37 indicate that SwiftComp and 3D FEA agree well in estimating the effects of interfacial stiffness on the effective elastic moduli E_2 and E_3.

The predictions of both effective axial and transverse shear moduli are also performed for different interfacial stiffnesses. Figure 4.38 shows that the axial shear modulus predictions of SwiftComp show slight deviation from 3D FEA. This deviation

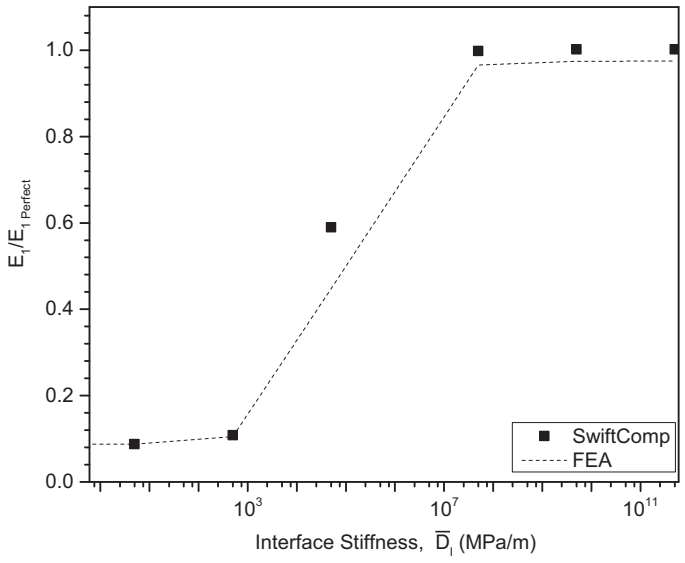

Figure 4.35. Predictions of effective elastic modulus E_1

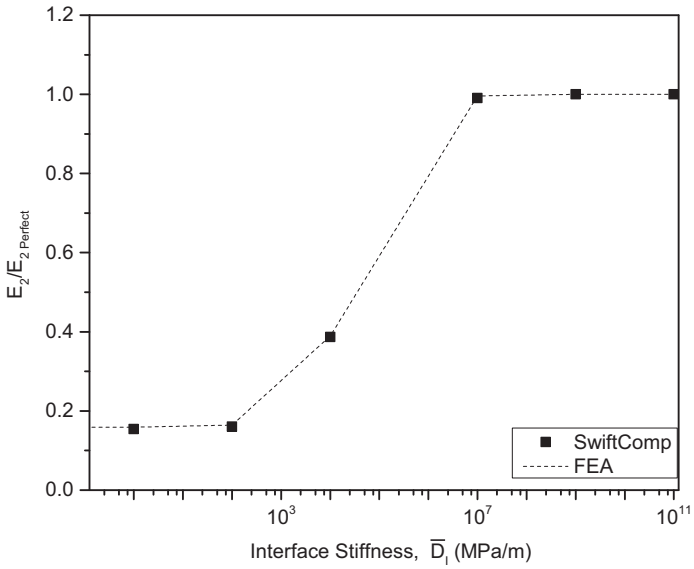

Figure 4.36. Predictions of effective elastic modulus E_2.

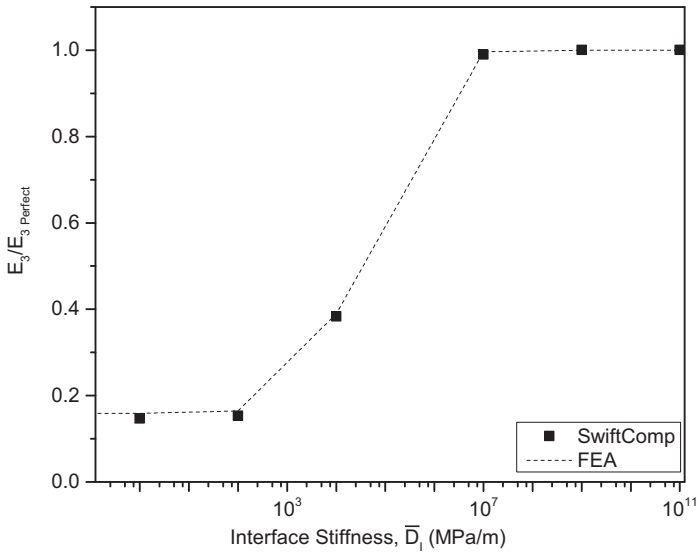

Figure 4.37. Predictions of effective elastic modulus E_3.

may be due to the contributions of interfacial stiffness in mode II direction that are not well predicted using INTER204 element. Figure 4.39 indicates that the predictions of SwiftComp for the effective transverse shear modulus agree well with the prediction of 3D FEA. In general, the imperfect interface analyses for discontinuous fiber-reinforced composite suggest that the stiffness in mode II direction does not affect the predictions of the transverse axial E_2 and transverse shear modulus G_{23}. However, it significantly affects axial elastic modulus E_1 and axial shear modulus G_{12}.

In Figure 4.40, the effects of interfacial stiffness on the effective Poisson's ratio are also analyzed. SwiftComp and 3D FEA show good agreement except for the small deviation for small interfacial stiffness. As described for the continuous fiber-reinforced composite, the effective axial Poisson's ratio is higher for lower interfacial stiffness due to difference in the global strains in the two directions, i.e., $\frac{\varepsilon_{22}}{\varepsilon_{11}}$, this ratio is higher for lower stiffness. As stiffness increases, both the global strains reduce and their overall ratio will go down as depicted in Figure 4.40. However as the stiffness keeps on increasing, it does not have significant effect on ε_{22} but ε_{11}

further reduces. This results in the increase of $\frac{\varepsilon_{22}}{\varepsilon_{11}}$ and finally converges to the perfect interface prediction. The same holds for transverse effective Poisson's ratio but in this case ν_{23} is relatively smaller for lower interfacial stiffness as discussed for continuous fiber-reinforced composite.

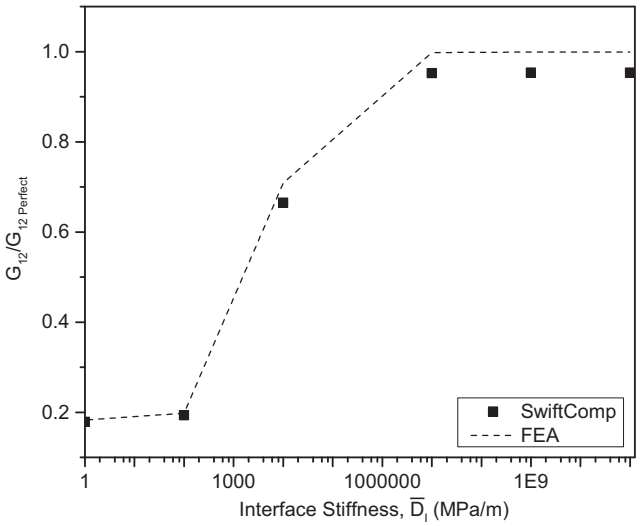

Figure 4.38. Predictions of effective axial shear modulus G_{12}.

The effect of imperfect interface on strength of the composite is also analyzed. Figure 4.41 shows that imperfect interface considerably affects the failure strength of discontinuous fiber-reinforced composite. It is also observed that the prediction of SwiftComp and 3D FEA has a slight difference which may be due to the effect of interfacial stiffness $\bar{D}_{II}$ that are not well predicted using INTER204 element.

Aligned-Staggered Array

The SG of SwiftComp and 3D FEA is shown in Figure 4.16 and it is meshed to have $9,120$ elements for SwiftComp and 3D FEA. In this case, it is assumed that the interfacial stiffness $\bar{D}_{II} = \bar{D}_{III} = 5\bar{D}_I$. From the analyses, it is observed that the

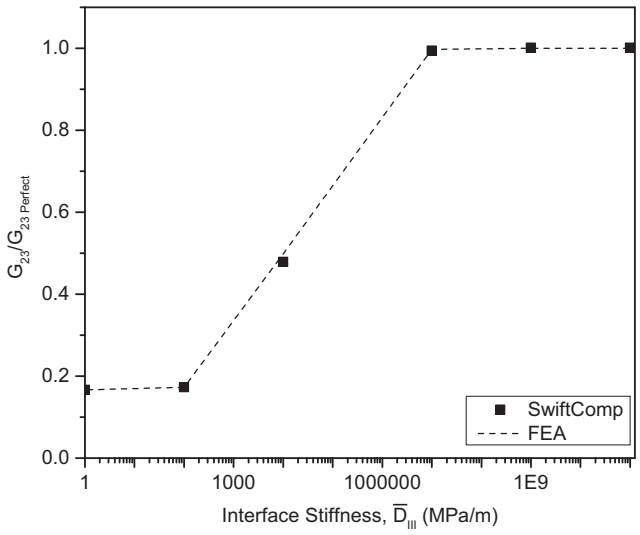

Figure 4.39. Predictions of effective transverse shear modulus G_{23}.

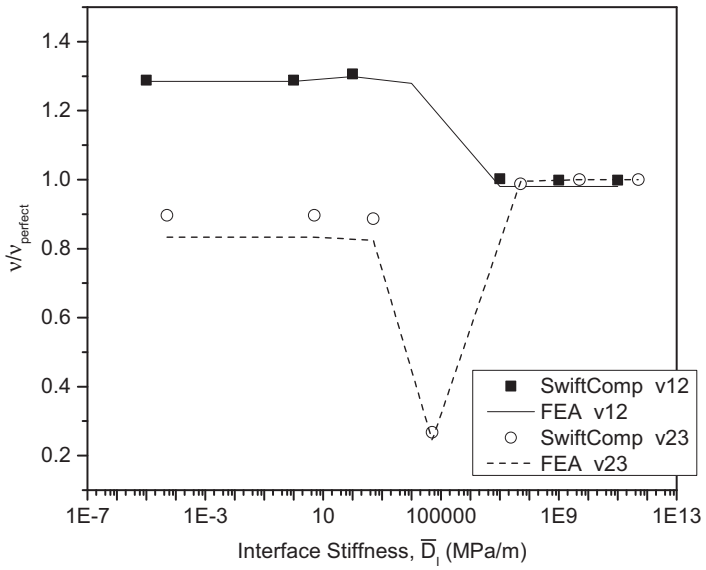

Figure 4.40. Predictions of effective Poisson's ratio ν_{23}.

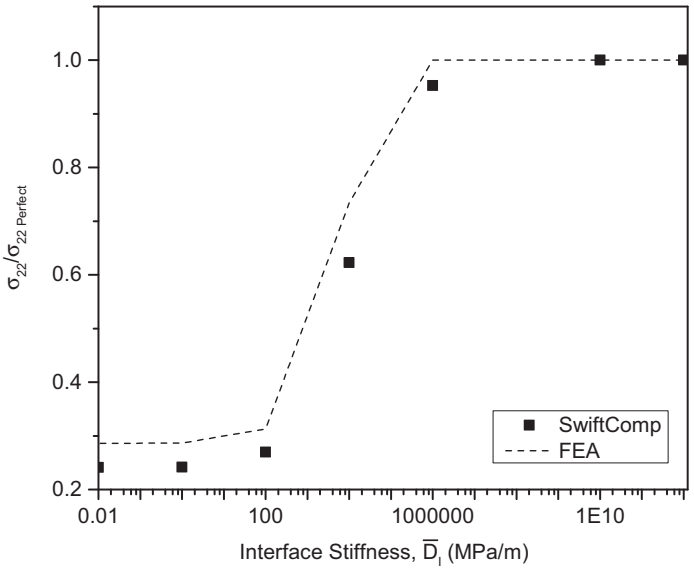

Figure 4.41. Predictions of failure strength, σ_{22}.

effective properties are significantly affected by imperfect interface. Figures 4.42, 4.43 and 4.44 show that the predictions of E_1, E_2 and E_3 are affected by interfacial stiffness. For all E_1, E_2 and E_3, SwiftComp and 3D FEA are in an excellent agreement. Figures 4.45 and 4.46 show that the axial and transverse shear moduli are also significantly dependent on the interfacial stiffness. The predictions of SwiftComp and 3D FEA show excellent agreement.

As described for the continuous fiber-reinforced composite, the effective axial Poisson's ratio is higher for smaller interfacial stiffness due to difference of global strains in the two directions, i.e., $\nu_{12} = \frac{\varepsilon_{22}}{\varepsilon_{11}}$. The up and downs of the effective Poisson's ratios are due to the relative changes of global strains in the corresponding directions as discussed for the continuous fiber-reinforced composite and the aligned regular array as well. Figure 4.47 shows that predictions of Poisson's ratios of SwiftComp is in a very good agreement with 3D FEA except slight deviation for

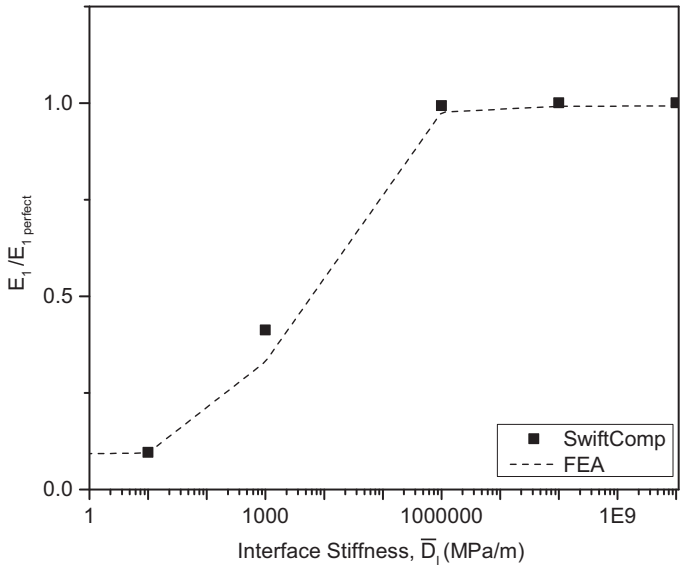

Figure 4.42. Predictions of effective elastic modulus E_1.

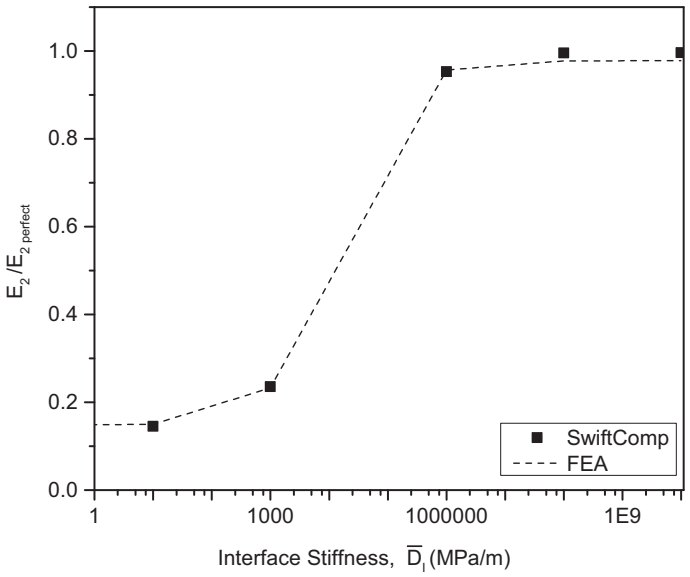

Figure 4.43. Predictions of effective elastic modulus E_2.

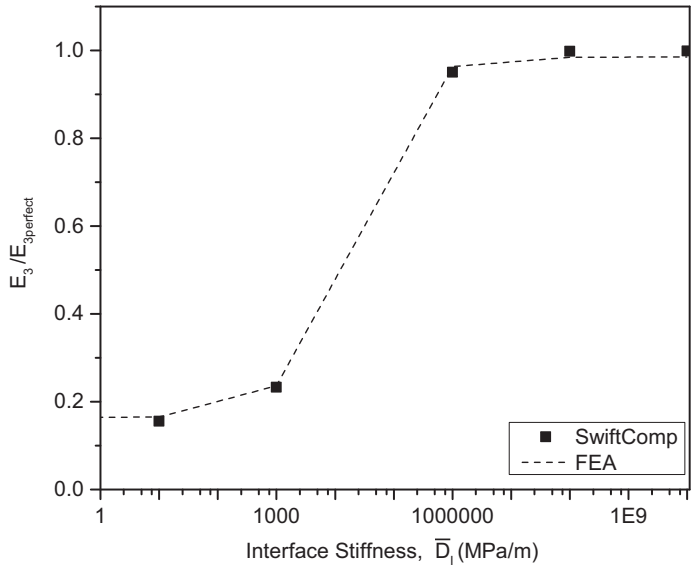

Figure 4.44. Predictions of effective elastic modulus E_3.

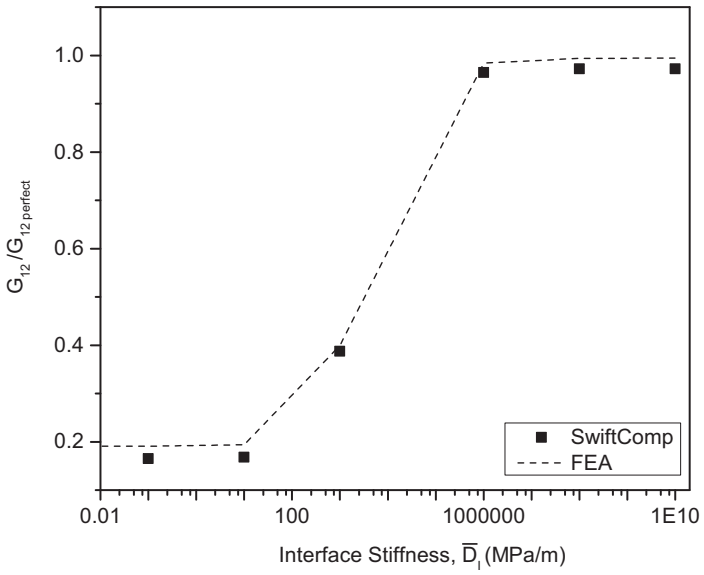

Figure 4.45. Predictions of effective axial shear modulus G_{12}.

ν_{23} for smaller interface stiffness. This deviation is due to the inability of INTER204 to capture the effects of $\bar{D}_{II}$.

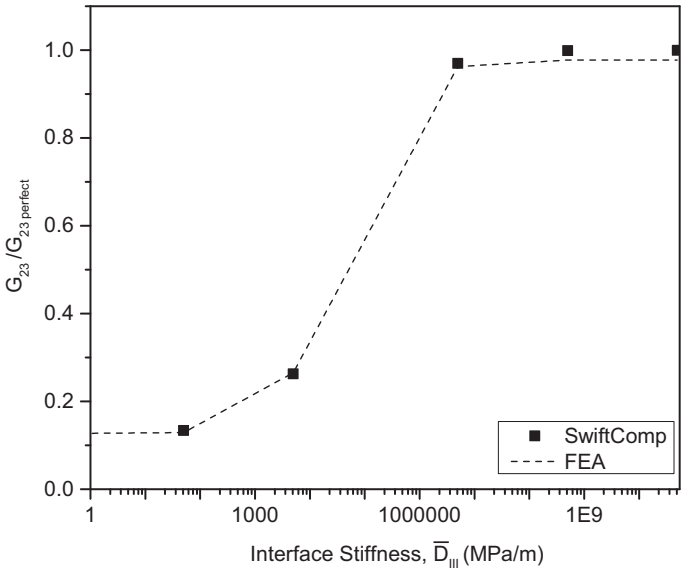

Figure 4.46. Predictions of effective transverse shear modulus G_{23}.

4.2.5 Woven Composite

The SG of woven composite used for failure analysis (Figure 4.19) is also used for analyzing imperfect interface. The SG of 3D FEA/SwiftComp is meshed to have 8,640 elements. The material properties and the corresponding volume of warp, weft and the matrix are listed in Table 4.23. The interfacial stiffness is related as $\bar{D}_{II} = 5\bar{D}_{11} = \bar{D}_{III}$ for this case. It is also assumed that the interfacial stiffness between different materials (warp, weft and matrix) are the same. The effects of interfacial stiffness on the effective properties of woven composite are analyzed for various interfacial stiffnesses.

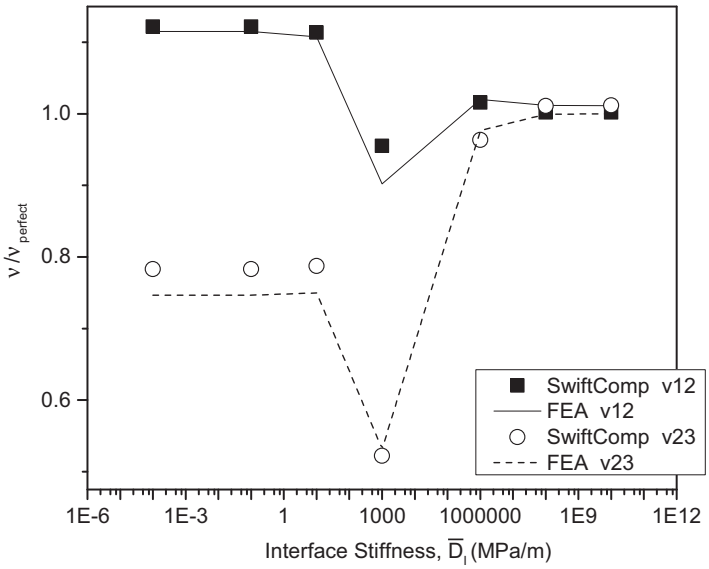

Figure 4.47. Predictions of effective Poisson's ratios ν_{12} and ν_{23}.

Table 4.23. Material property (Ref. [159])

Mat	E (GPa)	ν	vol(%)
Warp	130	0.30	25.95
Weft	86	0.22	25.95
Matrix	4.30	0.34	48.10

Figures 4.48,and 4.49 show that interfacial stiffness severely affects the effective properties of woven composite. The predictions of SwiftComp and 3D FEA show excellent agreements.

Figure 4.50 shows that the predictions of SwiftComp and 3D FEA are in good agreement for Poisson's ratio, ν_{13}, except a slight deviation for lower interfacial stiffness. This deviation could be due to the effect of the interface stiffness that corresponds to mode II failure that 3D FEA insufficiently predicts its effect as discussed for other examples. From the imperfect interface analysis of this composite,

it is also noticed that the introduction of imperfect interface with different material properties will make the woven composite to exhibit anisotropic material property, i.e, the stiffness matrix is fully populated for relativity smaller stiffness, however, as the interfacial stiffness increases orthotopic material property will be obtained.

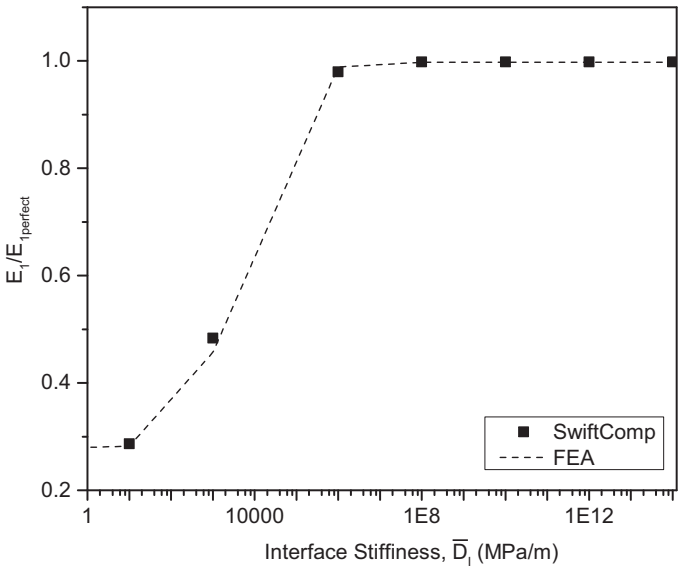

Figure 4.48. Prediction of E_1.

4.3 Progressive Failure Predictions

In progressive damage analysis, after each static or cyclic global loading, the homogenization and dehomogenization analyses are carried out. This is followed by evaluation of damage at each numerical integration point using the nonlocal approach based on Eq. (3.26). If $\bar{f}_{\boldsymbol{p}} > 0$, plasticity occurs, then the evolution of plastic strain is obtained by consistency equations, i.e., $\bar{f}_{\boldsymbol{p}} = 0$, $\dot{\bar{f}}_{\boldsymbol{p}} = 0$. Similarly, if $\bar{f}_{\boldsymbol{d}} > 0$, the damage evolution is estimated using incremental algorithm based on consistency conditions, i.e., $\bar{f}_{\boldsymbol{d}} = 0$, $\dot{\bar{f}}_{\boldsymbol{d}} = 0$. The stiffness matrix in Eq. (3.42) or Eq. (3.44) are

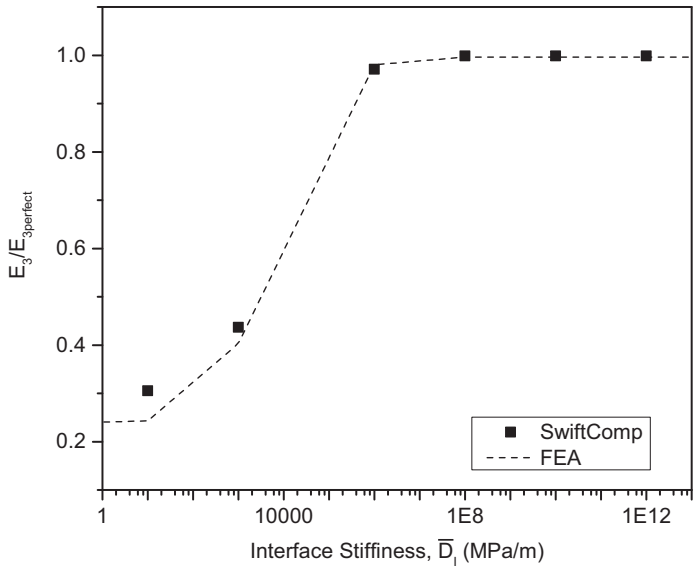

Figure 4.49. Prediction of E_3.

then updated for each loading. The proposed approach is summarized in the flow chart shown in Figure 4.51 and 4.52.

Material Constants

The material constants, σ_y, Q, and b in Eqs. (3.19) and (3.20) and also B_o, L, and o in Eqs. (3.26) and (3.30) are obtained by calibrating with experimental data for monotonic loading. Once the material constants are obtained. The prediction either for monotonic or fatigue loading of any heterogeneous materials with same constituents can be performed.

For example, let a cuboidal SG with 10% particle volume fraction be used. In this case, monotonic stress-strain experimental data of the composite are available [112]. Thus, the material constants both for plasticity σ_y, b, and Q, and also for damage analysis B_o, L, and o are calibrated by numerically simulations. Let the material

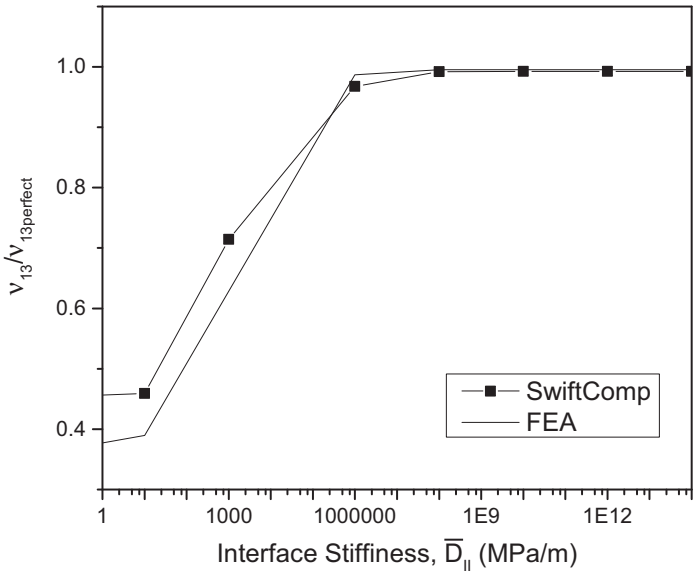

Figure 4.50. Prediction of ν_{13}.

constant in Eq. (3.27) c^d be equal to 0, and $\mathcal{H}$ in Eq. (3.19) is assumed to be diagonal fourth-order tensor with all its components equal to 1. Moreover, critical damage D_c is assumed to be 0.35 and 0.50 for the fiber and the matrix, respectively. And also, one can assume that both materials experience plasticity and damage. The yield limit of the particle is approximated, while the yield limit of the matrix is measured as shown in Table 4.24. Consequently, material constants for both plasticity and damage can be approximated using the yield and damage threshold limits of the constituents of the composite, respectively.

The calibration of the material constants can be performed as follows. The SG is loaded monotonically followed by evaluation of yielding at each integration point based on the yield limits of the constituents. Once yield is initiated, material constants σ_y, b, and Q iteratively calibrated based on the experimental data, i.e., various trial values are used to fit to the experimental data. In this case, i.e., particle

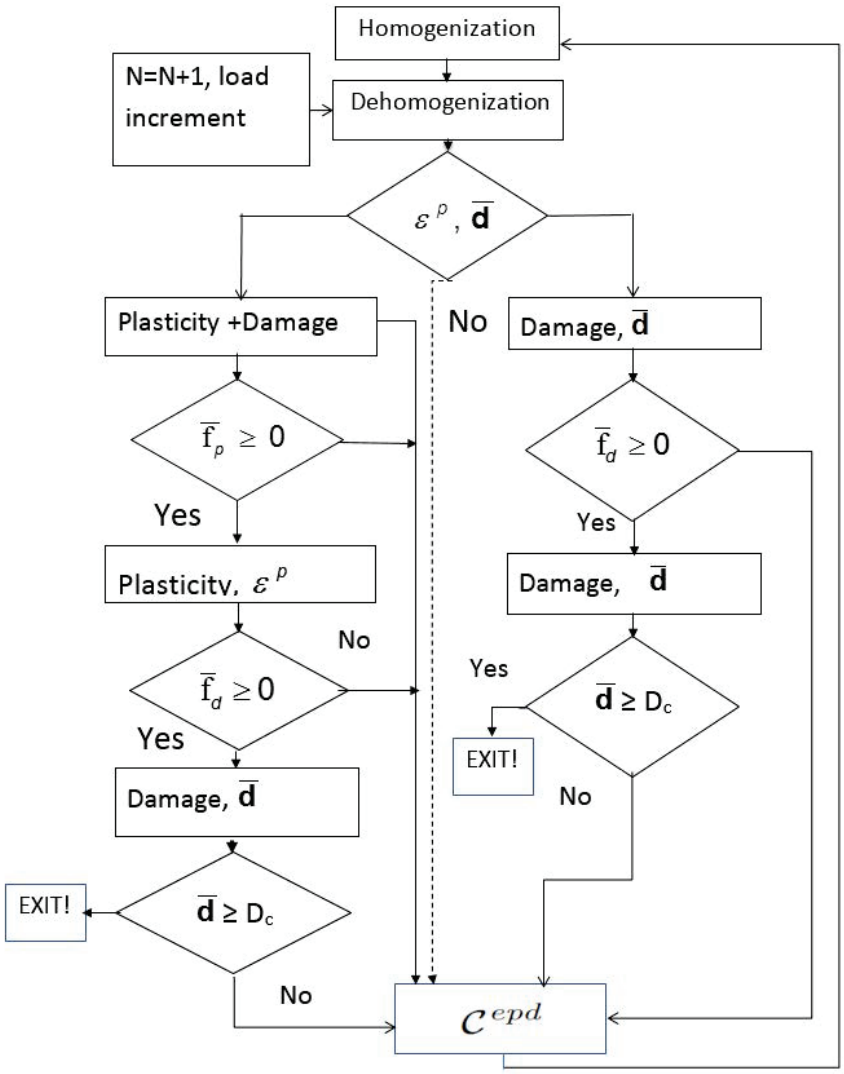

Figure 4.51. Summary of the proposed approach for progressive and fatigue failure predictions (DPA)

reinforced composite, it is reasonable to assume that the matrix control the failure of the composite. Following an intensive numerical simulation, σ_y, b, and Q can be obtained. To obtain other constants, we need to load the SG. As load increases, again, one should define maximum plastic strain beyond which the material experiences damage. Assume the strain is reached at a specific stress beyond the yield limit. Let the specified stresses be approximately 2869 MPa and 208 MPa for the fiber and the matrix, respectively. These specified stresses are used for obtaining the damage

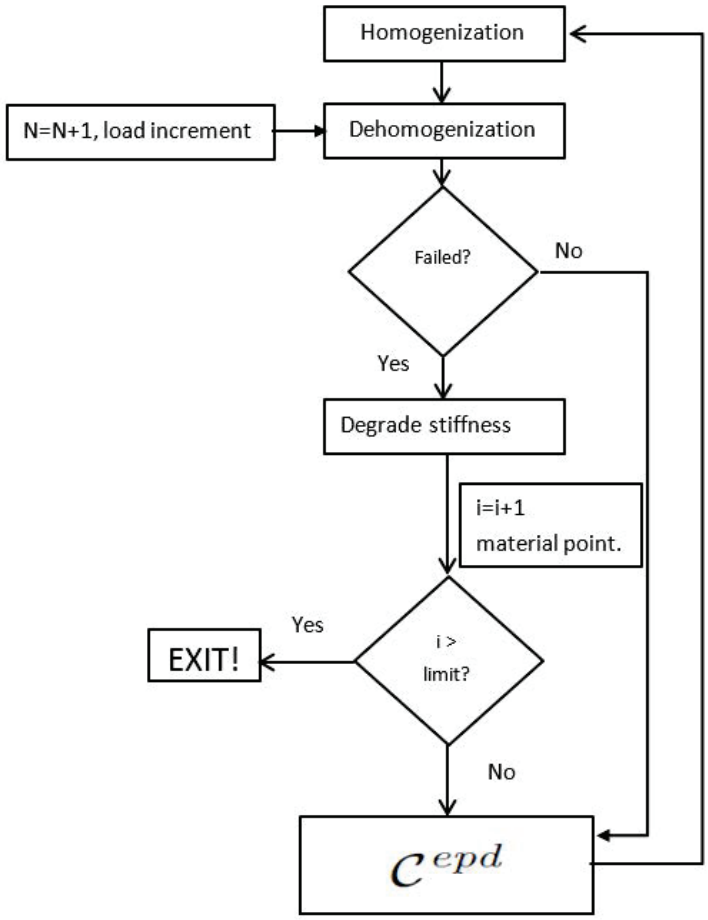

Figure 4.52. Summary of the proposed approach for progressive failure predictions FCA.

threshold level B_o for both particle and matrix using Eq. (3.26). If $\dot{f}_d < 0$, no damage. Thus, let the value of B_o be selected for infinitesimally small positive values of $\dot{f}_d < 0$ which results in infinitesimally small damage in each constituent. Please note that there is no further plasticity analysis at a material point once damage is initiated. Once the B_o of the particle and the matrix are estimated, L and o remain to be obtained. They are also iteratively obtained using numerical simulations by fitting the predicted value with experimental data for both constituents. The characteristic length l in Eq. (3.26) is assumed to be 0.1 for this example. The estimated material

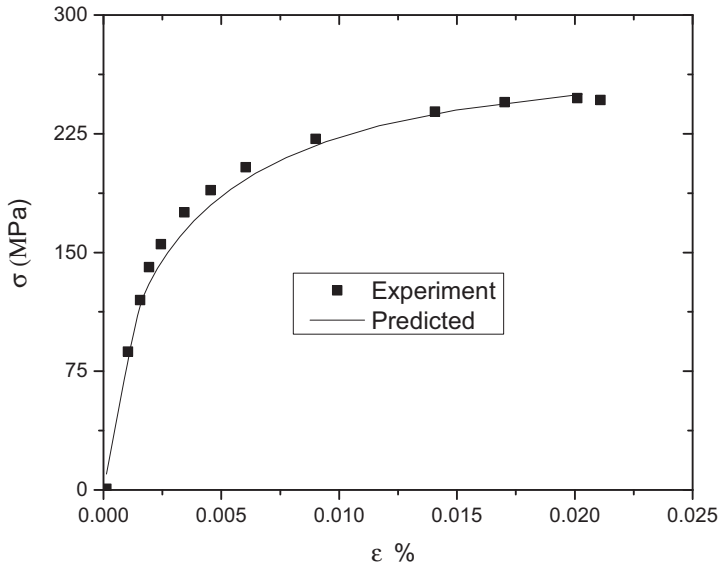

Figure 4.53. Stress-strain curve for particle-reinforced composite.

constants are shown in Table 4.24. These constants are then used to predict the stress-strain curve for the uniaxial loading. As shown in Figure 4.53, the predicted results show good agreement with the experimental data.

The calibrated data can also be used to estimate fatigue life of the composite

Table 4.24. Material constants for failure analysis (Ref. [112])

Materials	E (GPa)	ν	σ_y (GPa)	b	Q (GPa)	B_o(GPa)	L(GPa)	o
Particle	234.90	0.204	21	21*	2000*	8.2*	20*	10*
Matrix	69.90	0.330	0.135	12.5*	350*	0.8*	0.3*	5*

* estimated.

or the progressive damage in other type of heterogeneous materials with the same constituents.

Analysis of failure under presence of both plasticity and damage is very complex. And, the calibrations of material constants require numerous assumptions which may not be valid always. To simplify this problem, let damage be a major factor for the failure of the matrix and the particle. To analyze the predicting capability of this assumption, let the calibration of material constants be performed for 10% and 20% particle volume fractions using experimental data [112]. The calibration of the material constants, i.e., B_o, L, and o, is performed by assuming that the matrix controls the failure of the composite. These constants are calibrated by assuming a stress limit that initiates damage. Once the stress levels are set, the material constants are calibrated using numerical simulations by using various trial values that make the predicted stress-strain curve fit with the experimental data. Table 4.25 and 4.26 list the calibrated material constants for 10% and 20% particle volume fractions, respectively. The calibration of X_v, the ratio of failed material point to the total number of material points, is also performed along with characteristic length l to fit to experimental data, which helps estimate the failure strength of the composite using FCA (maximum principal stress criterion). The calibrated data obtained for 10% particle volume is used to estimate the failure strength of 20% and vise versa. The calibration is performed using DPA (anisotropic damage and isotopic damage, see Eq. (3.2) for isotropic damage) and FCA (maximum principal stress criterion).

Table 4.25. Calibrated material parameters for 10% particle volume fraction

Materials/damage	B_o (MPa)	o	L (GPa)	X_v	l
Anisotropic Damage					
Fiber	0.31	4.15	20.55	0.10	0.05
Matrix	7.7E-4	16.91	10.25	0.10	0.3
Isotropic Damage					
Fiber	0.31	6.150	20.60	0.10	0.05
Matrix	3.58E-6	1.59	35.25	0.10	0.30

Table 4.26. Calibrated material parameters for 20% particle volume fraction

Materials/damage	B_o (MPa)	o	L (GPa)	X_v	l
Anisotropic Damage					
Fiber	0.31	4.15	20.65	0.10	0.25
Matrix	3.5E-4	6.7	25.00	0.10	0.73
Isotropic Damage					
Fiber	0.31	4.00	20.60	0.10	0.25
Matrix	3.58E-6	21.7	2.52	0.10	0.73

Figure 4.54 and 4.55 show how the calibrated data fit to experiments for 10% and 20%, respectively. For both cases, the material constants are better calibrated for DPA approach (anisotropic and isotropic damage) compared with FCA using the maximum principal stress criterion. The deviations of calibrated and experimental data may be due to the current assumption of negligible plasticity. The fracture strains of the two experimental data, i.e., for 10% and 20%, are significantly different, approximately 2.2% and 0.4% for 10% and 20%, respectively, see Figure 4.54 and 4.55. As these differences do not seem reasonable for 10% difference of particle volume fraction, numerous factors can contribute for the differences including interfacial conditions and testing conditions. The differences may in turn affect the accuracy of the calibrated material constants to capture the physics of failure in the composite.

Figure 4.56 shows the prediction of the stress-strain curve of the particle-reinforced composite with 10% particle volume fraction using material constants calibrated using 20% particle volume fractions. It shows the experimental data are not well captured for this case particularly the failure strain, but the predictions of the failure stress are closer to experimental data. Figure 4.57 shows the prediction for 20% using material constants calibrated using 10% volume fraction of particle, this shows much better agreement with experiments for DPA except differences in failure strain. The predictions of FCA provide relatively good estimates for failure strain.

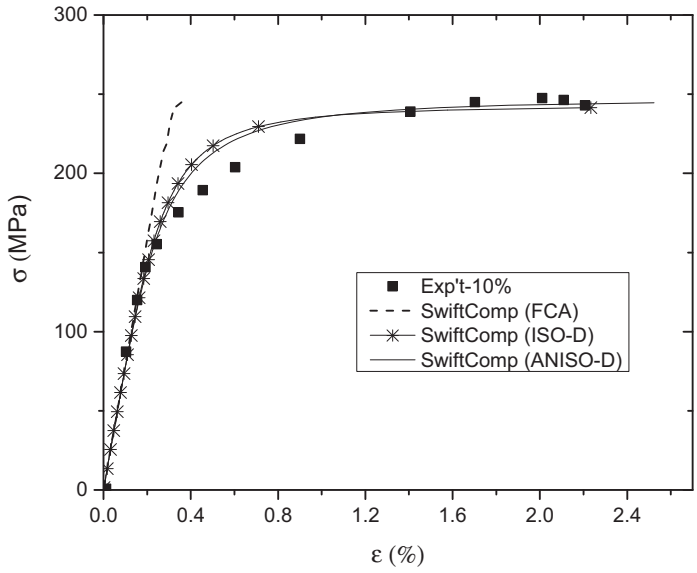

Figure 4.54. Prediction of stress-strain curve using a calibrated data for 10% particle volume fraction.

4.3.1 Failure Analysis of Composite Laminates

In this section, the two proposed approaches (DPA and FCA) are used for the progressive damage/failure analyses of composites. These analyses are performed using the nonlocal approach. The predictions of the progressive damage are performed mainly for composite laminate with different lay-up configurations. First, for both cases, i.e., DPA and FCA, the material parameters are calibrated based on the available experimental data [46]. The material properties of the fiber and matrix are listed in Table 4.27. Here, it should be noted that this study is performed using 3D micromechanics approach by adopting periodic boundary conditions in all boundary surfaces. This may slightly compromise the accuracy of the result as in actual condition the SG should be traction free both in the top and bottom surfaces.

In this study, the calibration of material parameters is performed for the fiber based on the unidirectional composite laminate while for the matrix, it is

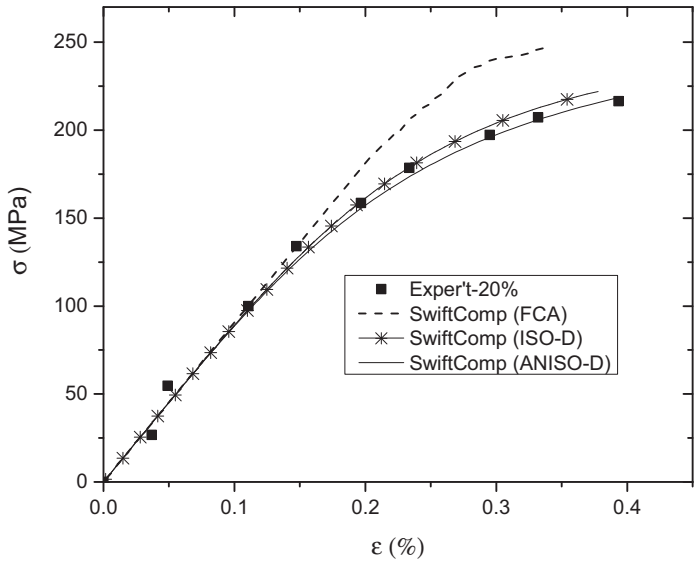

Figure 4.55. Prediction of stress-strain curve using calibrated data for 20% particle volume fraction.

Table 4.27. Material properties (Ref. [46]).

Material	E (GPa)	ν	σ_T (GPa)	σ_C (GPa)	ε_T %	ε_C %
Fiber	74	0.20	2.15	1.45	2.687	1.813
Matrix	3.35	0.35	0.08	0.15	0.05	-

performed using both unidirectional and $[0/90]_s$ laminates. The later one is adopted because the calibrated parameters obtained from unidirectional lamina show some inconsistencies. That is, as a common practice, the parameters of the fiber and matrix are independently calibrated for axial and transverse loading options, respectively. First, the fiber parameters are calibrated by assuming negligible damage in the matrix. Second, the matrix parameters are calibrated. Finally, the uniaxial predictions (in fiber direction) are performed using the calibrated parameters of both the fiber and

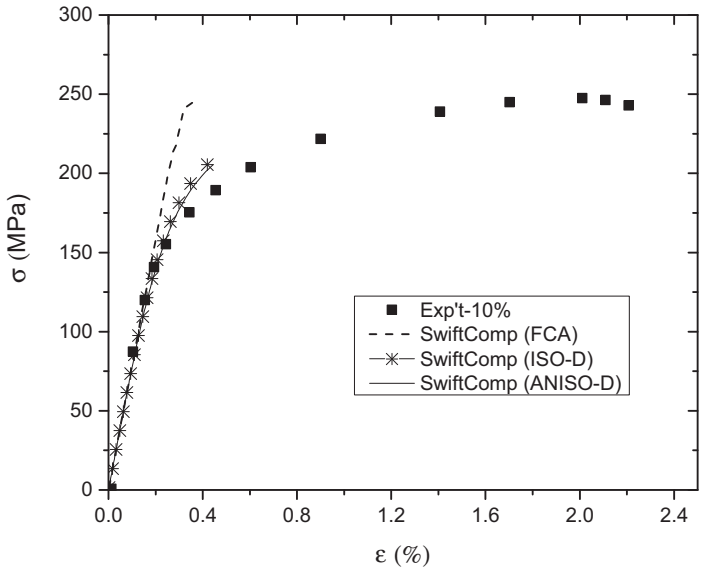

Figure 4.56. Prediction of stress-strain curve for 10% particle volume fraction.

matrix. For the current case, it shows that the matrix damage dominates the failure in unidirectional composite, which is inconsistent with the previous assumption of negligible damage in the matrix for axial loading. This inconsistency may contribute for poor predictions of failure strength of composite. For FCA, there is no much calibration of material parameters except failure strength and the corresponding volume of material failed (X_v). If the failure strengths of the fiber and matrix are available, the volume of material failed (the ratio of number of numerical integration points failed to total number of numerical integration points) are to be obtained. Thus, for each constituent, X_v and characteristic length l can be iteratively selected to fit the predicted values with experimental data. The material parameters calibrated using both unidirectional and $[0/90]_s$ composite laminates are shown in Table 4.28. All other material constants are assumed to be zero.

For this case, the SG of $[0/90]_s$ is meshed to have 6138 tetrahedron elements. The predicted stress-strain curve of the composite obtained using the calibrated

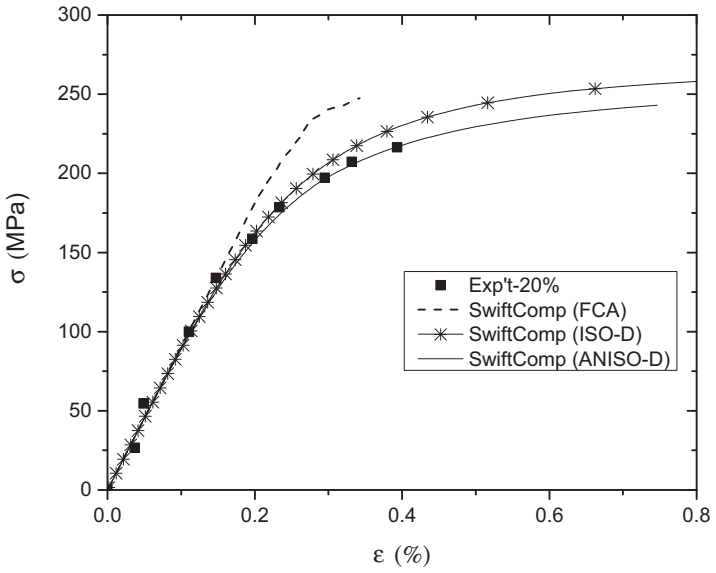

Figure 4.57. Prediction of stress-strain curve for 20% particle volume fraction.

Table 4.28. Calibrated material parameters

Materials	B_o (GPa)	o	L (GPa)	X_v	l
Fiber	31.00	15.15	205.50	0.100	0.2
Matrix	0.77	1.15	85.38	0.001	0.0015
Matrix $[0/90]_s$	0.77	7.15	118.20	0.50	0.50

parameters are compared with experimental data [46] as shown in Figure 4.58. As it can be seen from the figure, the stress-strain curve is fairly estimated except slight deviations for FCA-strain (maximum principal strain failure criterion) and DPA. The calibrated material parameters can also be used to predict other examples of composite lay-ups including $[\pm 45]_s$ and $[\pm 55]_s$. For the examples used here, the experimental data are obtained from Ref. [46].

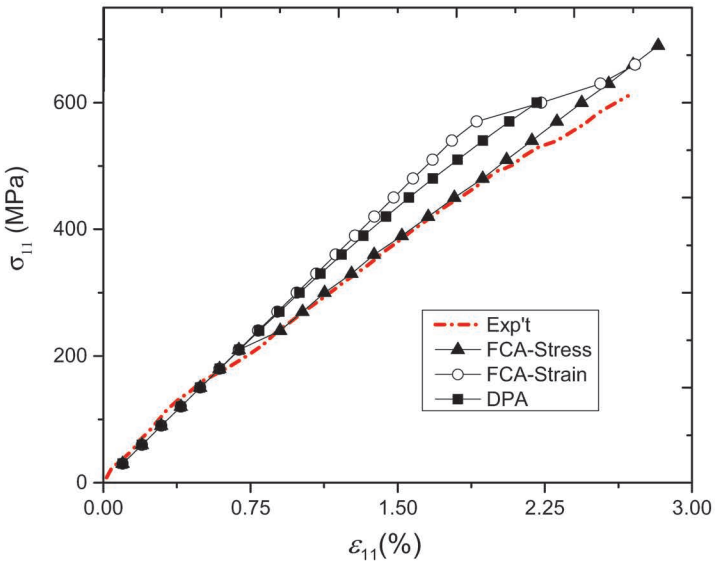

Figure 4.58. Predicted stress-strain curve of composite $[0/90]_s$

Composite laminate $[\pm 45]_s$

In this example, let the SG shown in Figure 4.59 be used and also let an equal bi-direction load in the direction of 1 and 2 be applied. The SG has $1.4142 \times 1.4142 \times 4$ size in direction 1, 2 and 3, respectively and is meshed to have 3295 tetrahedron elements. The prediction of stress-strain curve is performed by employing material parameters calibrated using both unidirectional and $[0/90]_s$ laminates. The predictions obtained using material parameters calibrated using unidirectional laminate significantly under predict the failure strength and stress-strain curve compared with the experimental data, indicated using arrow in Figure 4.60. These predictions are much lower than the predictions obtained for the material parameters calibrated using $[0/90]_s$. As it can be seen from Figure 4.60, FCA, using both the maximum principal stress and strain failure criteria, roughly estimates both the failure strength and stress-strain curve of the composite compared with experimental results. On the contrary, the predictions obtained from DPA better capture the stress-strain

curve and also closely estimates failure strength compared with the experimental data obtained using axial strain. The predictions using Puck failure criterion is found to be the best estimate from more than 12 failure criteria when it is compared to experimental data in Ref. [3]. As depicted in Figure 4.60, the current predictions of DPA are found to be better than the predictions obtained using Puck failure criterion.

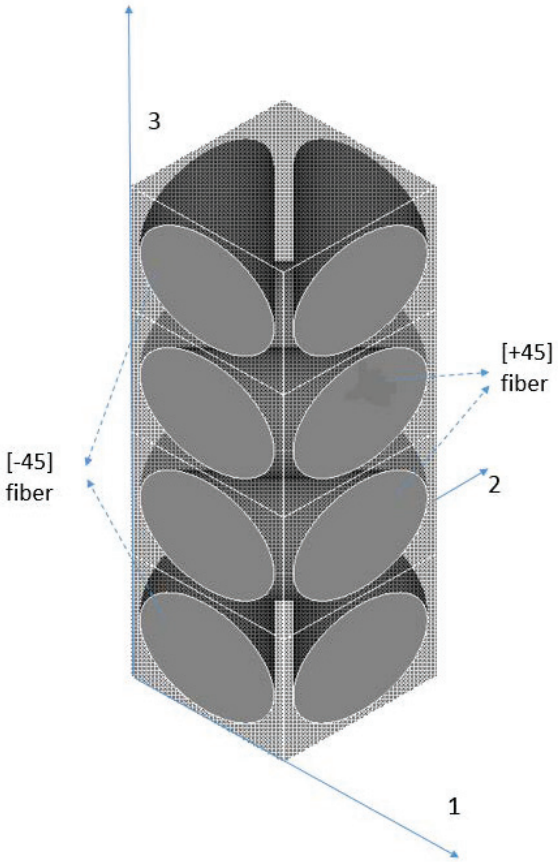

Figure 4.59. SG of $[\pm 45]_s$

Composite laminate $[\pm 55]_s$

The SG of $[\pm 55]_s$ is shown in Figure 4.61. It has $1.7343 \times 1.22078 \times 4$ size in direction 1, 2 and 3, respectively and the SG is meshed to have 6110 tetrahedron elements. For this example, the failure strength of $[\pm 55]_s$ is performed for matrix

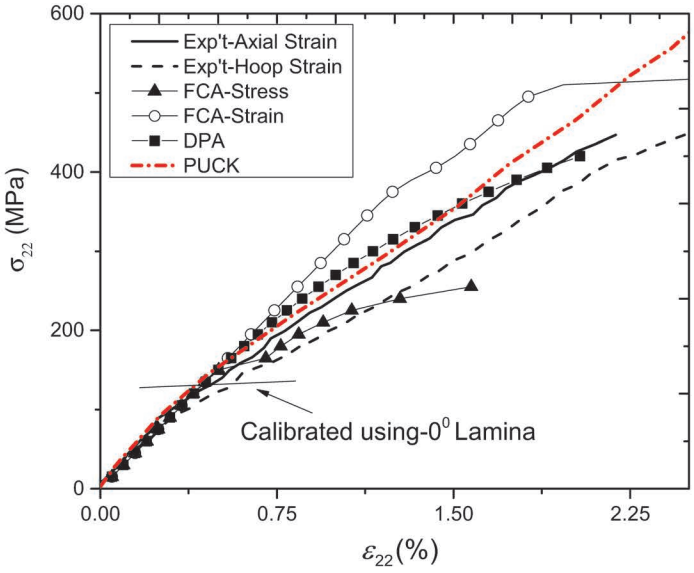

Figure 4.60. Prediction of stress-strain curve of $[\pm 45]_s$

parameters calibrated using $[0/90]_s$. The failure strength of the composite laminate is predicted using uniaxial loading in 2-direction. As shown in Figure 4.62, FCA, for both maximum principal stress and strain failure criteria, under predicts the failure strength of the composite but strain based criterion shows relatively better prediction. The prediction obtained using DPA is closer to experimental data except slight overprediction of the strength approximately by 12%. The predictions obtained using Eckold criterion, see [3], and the current predictions using DPA show similar estimate of the failure strength of the composite [3].

In this example, bidirectional loading options are also used to estimate the stress-strain curve of composite laminate. First, let the biaxial loads be in direction 1 and 2 with ratio of $\frac{\sigma_{22}}{\sigma_{11}} = \frac{2}{1}$. The predictions of failure strength of $[\pm 55]_s$ are shown in Figure 4.63. It is obvious to see that FCA using the maximum principal strain failure criterion overpredicts the stress-strain curve of the composite and also this approach does not predict well the stress-strain curve of the composite. On the

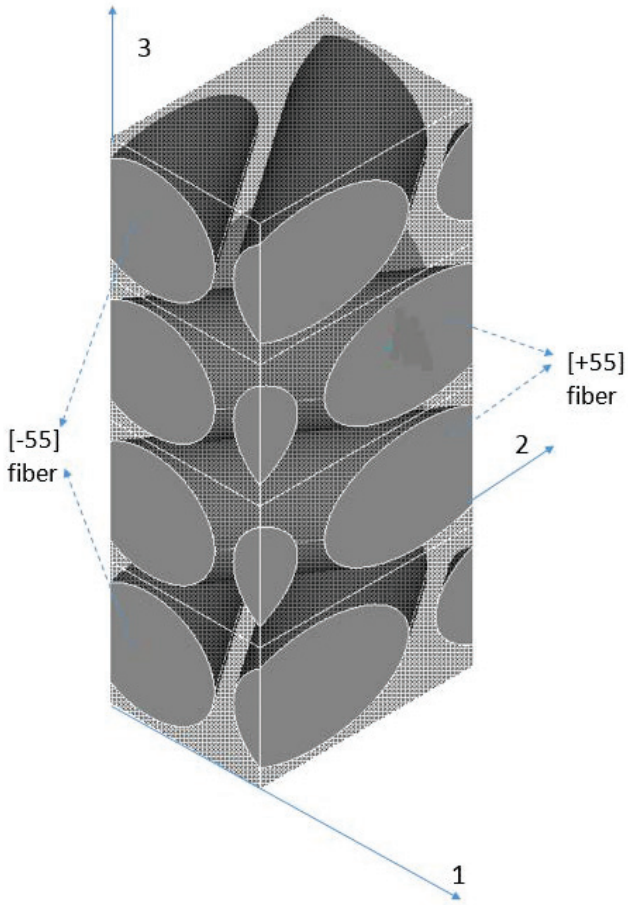

Figure 4.61. SG of $[\pm 55]_s$

contrary, FCA using the maximum principal stress criterion and DPA show relatively better for predicting stress-strain curve of the composite. The prediction of Tsai (see [3]) is the best one from 12 failure criteria. But the current predictions using FCA shows better estimate compared with the Tsai predictions.

4.4 Fatigue Failure and Life Predictions

The fatigue life prediction is computationally prohibitive if the analysis is allowed to run until the failure point is reached. Thus, for simplicity, the damage is assumed to be constant for each cycle throughout the whole analysis. During

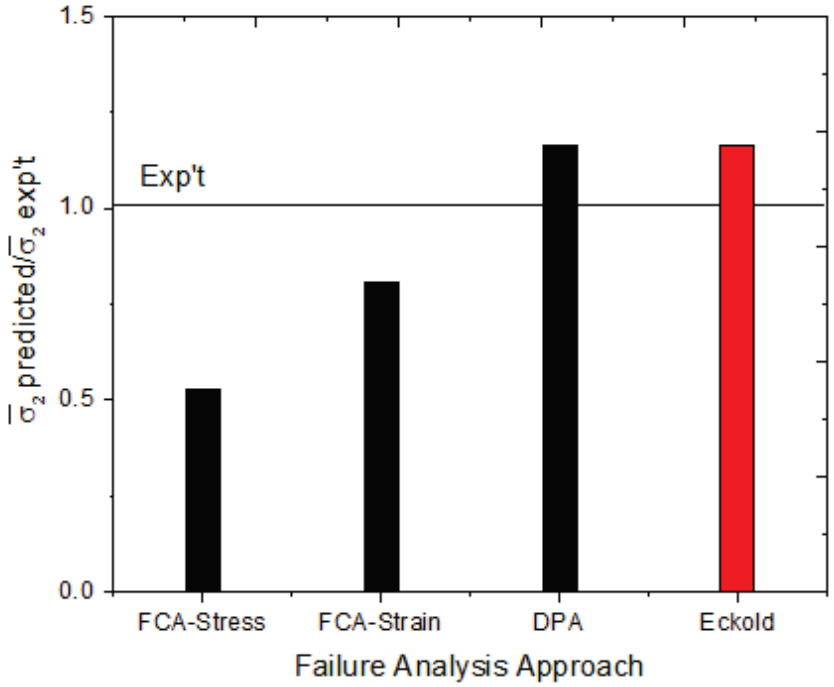

Figure 4.62. Prediction of failure strength of $[\pm 55]_s$

cyclic load, the growth of the damage remains to be constant for a ceratin loading period. Consequently, without affecting the anisotropic damage growth rate in each constituent of the composite, a reasonable number of cycle increment, for a specified damage amount, $\Delta\bar{d}$, is added to the cycle number. The cycle increment can be calculated as [13]

$$\Delta N_i = \frac{\Delta\bar{d}}{\left(\delta d/\delta N\right)}, \quad N_{i+1} = N_i + \Delta N_i, \quad d_{i+1} = d_i + (\delta d/\delta N)\Delta N_i \tag{4.2}$$

where $(\delta d/\delta N)$ denotes the rate of change of damage per cycle, it is assumed to be constant for a certain number of cycle N_i, $\Delta\bar{d}$ denotes the damage amount to be accounted during the cycle jump, it is usually approximated as $D_c/50$, D_c denotes critical damage level. For the current analysis, $\Delta\bar{d}$ is determined based on damage rate per cycle and it ranges from 10^{-3} to 10^{-5}. For a given global stress or strain loading, the maximum cycle number or fatigue life N is obtained based on the critical damage value D_c. The critical damage level is evaluated at each integration point. If

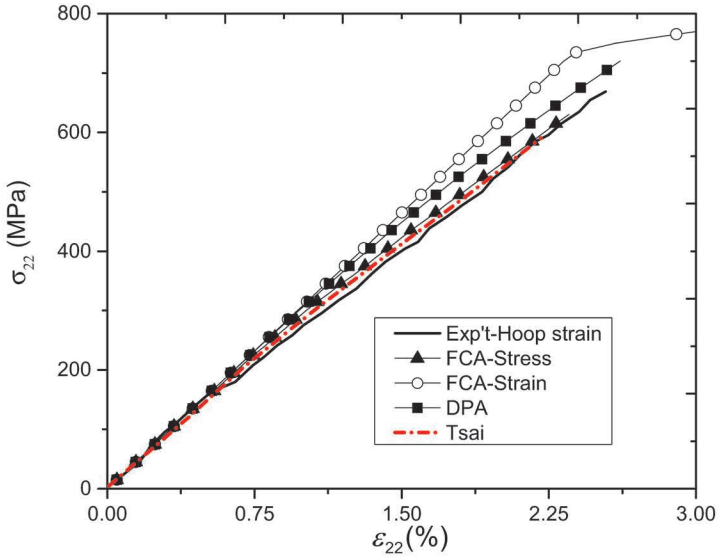

Figure 4.63. Prediction of stress-strain curve of $[\pm 55]_s$

damage at any given point reaches the critical damage level, then it is assumed that crack starts to propagate indefinitely resulting in the ultimate failure of the material.

4.4.1 Fatigue in Ductile Material

As seen from the predicted results for monotonic loading in progressive failure analysis discussed above. It is possible to use the estimated material constants to predict the fatigue life of the composite. In this case, let the stress ratio $R = \frac{\sigma_{min}}{\sigma_{max}}$ be 0.6. Since the failure is controlled by matrix, it can be treated as a ductile failure analysis. The fatigue life of the particle reinforced composite is estimated as it can be seen from Figure 4.64. No experimental data to compare with. The arrow in the figure shows stress below 80 MPa will not cause fatigue damage. For the current example, the fatigue life is dependent on the growth of local accumulated plastic strain and damage in the composite. To investigate this, let a cyclic load of 1.5 MPa be used. It is observed that the damage starts to propagate after excessive

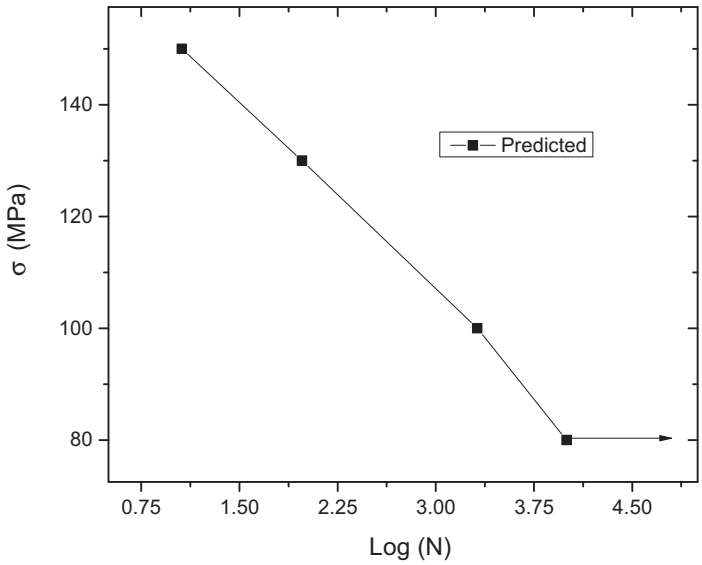

Figure 4.64. S-N curve for particle reinforced composite.

accumulated plastic strain. However, the growth of weighted averaged damage in the matrix is much greater than its accumulated plastic strain near the fracture point as shown in Figure 4.65. Moreover, it is also noticed that the progressive fatigue damage can significantly affect the effective properties of the composite as shown in Figure 4.66. E_{1n} and ν_{12n} are the effective stiffness and Poisson's ratio normalized with the undamaged effective stiffness and Poisson's ratio ratio of the the material, respectively. In this analysis, the shear moduli are observed to be negligibly affected.

4.4.2 Fatigue in Brittle Material

In this section, the proposed approach is partially validated using the predictions obtained from experimental data. The glass/epoxy composite is used for this prediction. The fiber and matrix are assumed to have an elastic modulus of 78.5

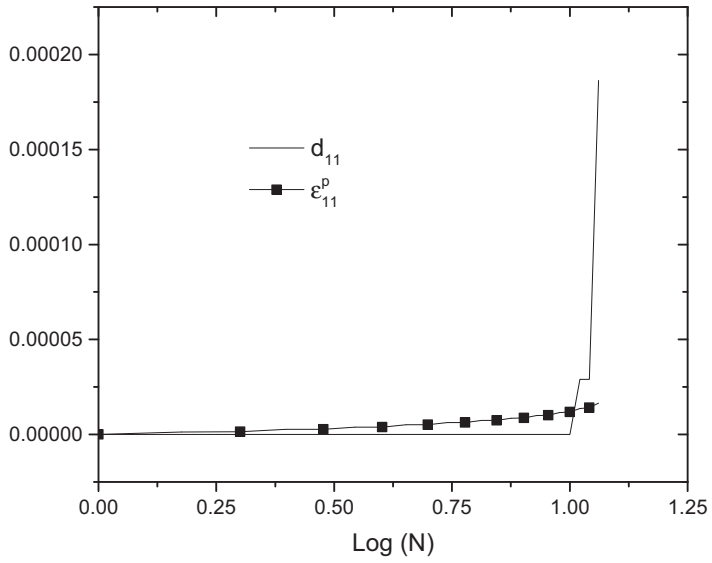

Figure 4.65. Weighted averaged accumulated plastic strain and damage in particle reinforced composite.

GPa and 3.45 GPa, respectively, and with the corresponding Poisson's ratios of 0.25 and 0.35, respectively. The fiber matrix volume ratio is 0.6. The stress ratio $R = \frac{\sigma_{min}}{\sigma_{max}}$ is 0.10. The experimental data are obtained from [161]. In the current prediction, it is assumed that the material constant in Eq. (3.27) $c^d = 0$. Since the monotonic loading data are not available, the calibration of the material constants, B_o, L and o are performed based on the fatigue data, i.e., minimum stress/endurance limit from experimental S-N curve and its corresponding fatigue life. Finally, the fatigue life of the composite for various loads is estimated based on the calibrated data.

It should be noted that since the current approach is entirely based on micromechanics analysis particularly on the local fields, the specified material constants for each constituent are required to sufficiently estimate the fatigue life of the composite. However, if these material constants are not available, it is suggested to assume the failure mode for each loading direction. For instance, for continuous

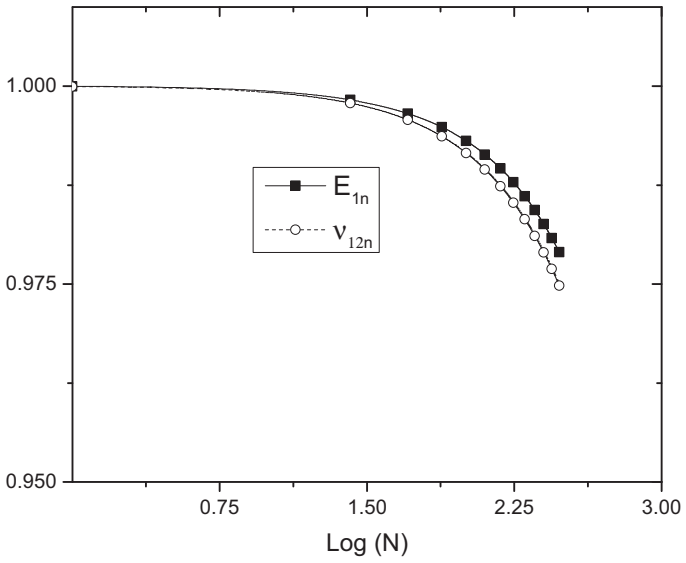

Figure 4.66. Degradation of effective properties of particle reinforced composite.

fiber reinforced composite, it may be reasonable to assume that the fiber controls the failure of the composite in the fiber direction while in the transverse direction the matrix controls the failure. Based on these assumptions, the specified material constants may be calibrated for each constituent of the composite.

The material constants B_o, L and o can easily be calibrated for fiber using uniaxial load. Let the average minimum stress at the specified fatigue life N, be approximately 0.7375 GPa as it can be seen from S-N curve depicted in the Figure 4.67. Then, one can calibrate the damage threshold B_o as follows. First, apply the global load equivalent to the minimum stress then evaluate the damage at each numerical integration points using Eq. (3.26). Second, it is known that the initial damage occurs whenever $Y_{EQ} = B_o$. Thus, we can freely select the value of B_o to have infinitesimally small damage for the given global load. For the current case, $B_o = 12.772$ MPa is selected for infinitesimally small damage. The material constants in Eq. (3.29), L

and o, are also obtained using the calibrated value of B_o and minimum stress with the corresponding fatigue life N.

In this case, the fatigue life N is iteratively simulated for different values of L and o by applying the global load equivalent to the minimum stress. The process is repeated until the predicted fatigue life is sufficiently equal to the fatigue life measured by experiment. If these two values are nearly equal, the values of L and o are then used as calibrated material constants. For the current case, the calibrated values of L and o are found to be 970 GPa and 8, respectively. These constants are in turn used to estimate the fatigue life of the composite. One should notice that critical damage D_c is also a material parameter. For this case, 0.35 and 0.55 are used for the fiber and matrix, respectively.

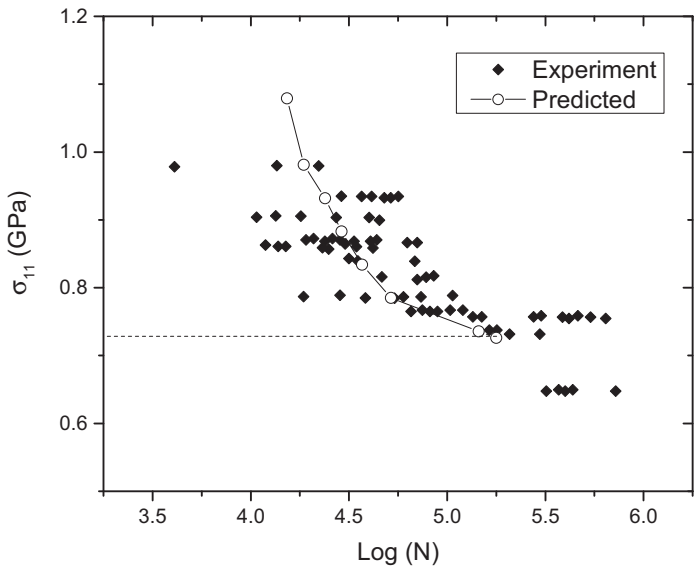

Figure 4.67. S-N for continuous fiber-reinforced composite.

Using the calibrated material constants, the fatigue life of the composite for various loads is generated as shown using the S-N curve in Figure 4.67. The prediction shows

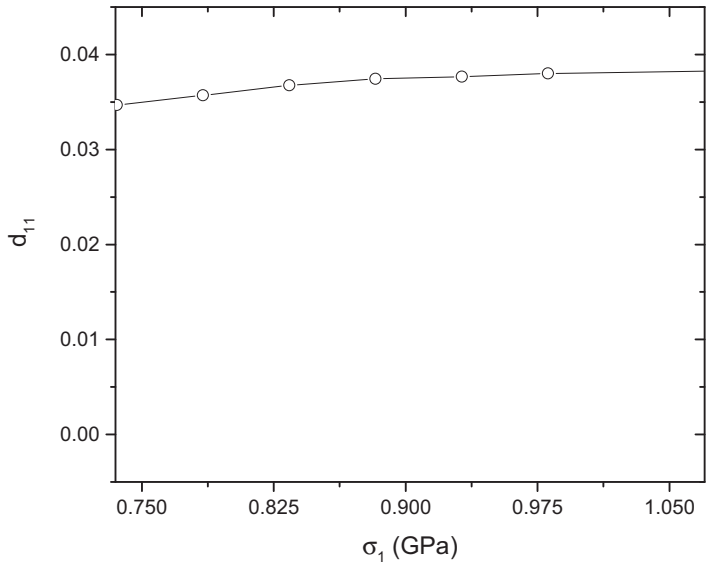

Figure 4.68. Weighted averaged damage at failure.

a good agreement with the experiment. It is also noticeable to see the variation of experimental data which precipitates from various contributing factors such as variability of manufacturing process, human error, etc. In these predictions, it is noticed that, at failure, the weighted average damage in the composite is not affected by the magnitude of the applied load as shown Figure 4.68. Similar predictions are also observed for other components of the damage tensor. It is clear that the progressive fatigue damage affects the effective stiffness of the composite. For instance, for global load, 1.079 GPA, it is observed that the progressive fatigue damage induced significant degradation of effective elastic modulus and also affect the Poisson's ratio of the composite as shown in Figure 4.69. However, the transverse shear moduli are insignificantly affected.

In another estimation of fatigue life of unidirectional continuous fiber-reinforced composite, the material properties listed in Table 4.29 are used. The fiber volume fraction is approximately 0.70. In this analysis, let the composite be loaded in

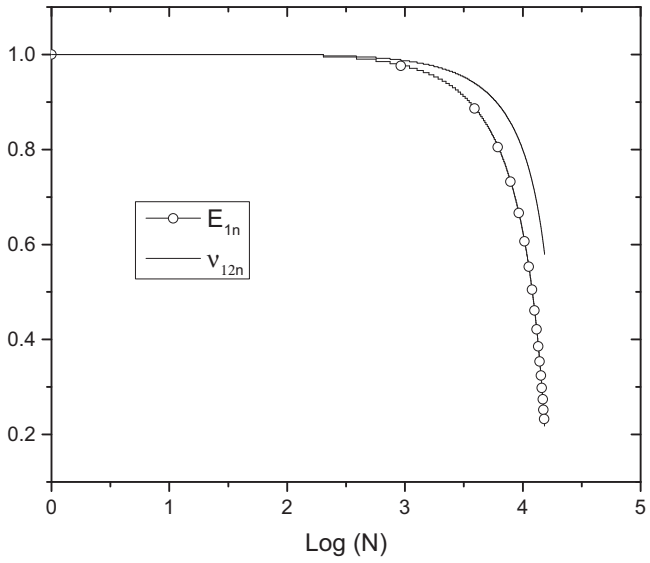

Figure 4.69. Degradation of effective stiffness and Poisson's ratio.

transverse direction. Thus, it is reasonable to assume that the matrix controls the failure of the composite. Consequently, the materials constants B_o, L, and o are calibrated as described for the first case based on the matrix and are approximately found to be 0.5588 MPa, 5 GPa and 6, respectively. In this case, we also assume $c^d = 0$. The critical damage values of D_c, 0.33 and 0.53, are used for the fiber and matrix, respectively. The fatigue life for transversely loaded composite is estimated based on the calibrated material. The prediction is in a fairly good agreement with the experiments as shown in Figure 4.70.

For transverse load, one can expect higher stress distribution in the fiber matrix interface due to the interaction between the two constituents with higher material property mismatch. This stress disturbance may result in significant material degradation locally. For instance, for 37 MPa transverse cyclic load, the effect of stress disturbance can be seen from the weighted averaged damage propagation in the matrix

Table 4.29. Material property for fatigue analysis (Ref. [162])

Material	E_1 GPa	E_2 GPa	G_{12} GPa	ν_{12}	ν_{23}
Fiber	194.30	15.00	18.10	0.275	0.275
Matrix	3.45	3.45	1.27	0.350	0.350

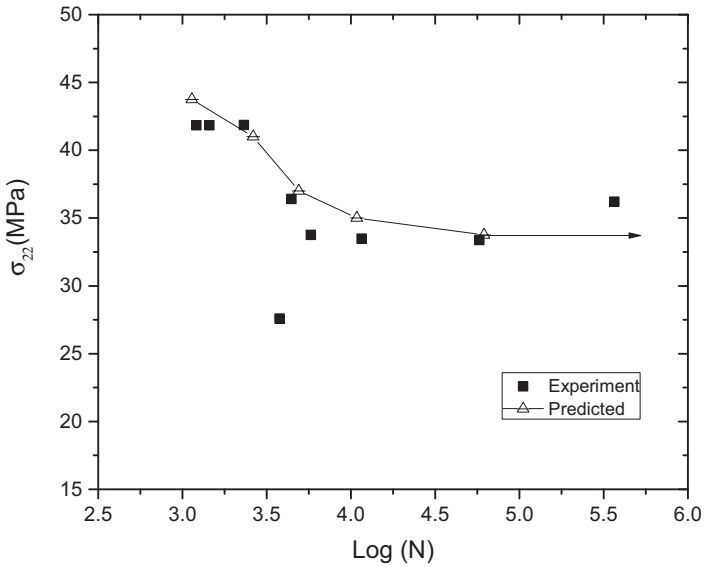

Figure 4.70. S-N for transversely loaded continuous fiber-reinforced composite.

as shown in the Figure 4.71. It can easily be noticed that the damage propagation in the transverse direction d_{22} is significantly larger than the other damage tensor components which results from the higher stress disturbance along the interface of the composite.

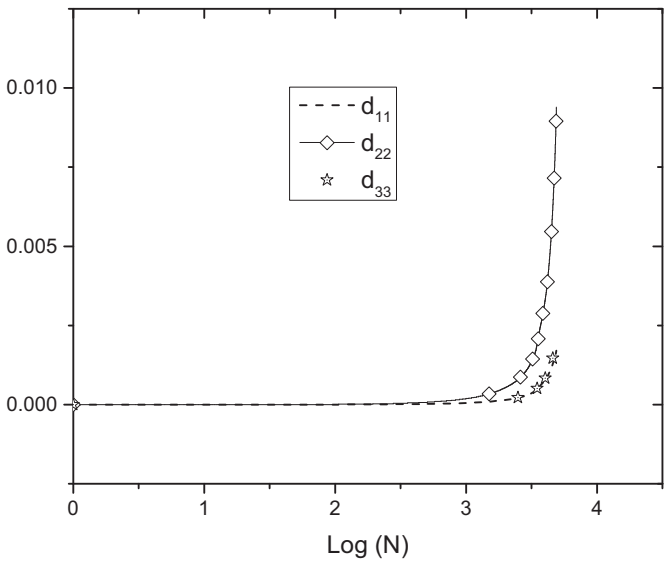

Figure 4.71. Weighted averaged damage propagation in the matrix.

5. CONCLUSION

Failure of heterogeneous materials is analyzed using pointwise local fields and a nonlocal approaches by employing micromechanics approach based on MSG. MSG helps to accurately and efficiently predict both effective properties and local fields in heterogenous materials. The predictions obtained from these analyses are compared with various micromechanics approaches including mean field approaches (MT and DI), GMC and HFGMC, and also 3D FEA. The static failure predictions of several examples of heterogeneous materials including continuous fiber-reinforced composite, particle-reinforced composite, discontinuous fiber-reinforced composite, and woven composite are analyzed by employing various failure criteria including maximum normal stress and strain maximum shear stress, Tsai-Hill and Tsai-Wu criteria.

From static failure analysis, it is learned that the mean field approaches (MT and DI) cannot accurately predict the initial failure strengths and initial failure envelopes of the heterogeneous materials due to their inability to accurately predict the local fields particularly for SG with complex microstructure. GMC and HFGMC predict better compared with the mean field approaches, however these approaches also poorly predict the static failure strengths for both uniaxial and biaxial loading conditions using maximum normal stress and strain failure criteria. The predictions of these approaches show relatively better agreement with 3D FEA for Tsai-Hill failure criterion. The predictions of MSG are in an excellent agreement with the predictions of 3D FEA for both uniaxial and biaxial loading conditions using all considered failure criteria. The nonlocal approach also estimates failure with much less mesh dependence compared with pointwise approach. It is also learned that the predictions of nonlocal and pointwise approaches show close prediction irrespective of the characteristic length for uniaxially loaded continuous fiber-reinforced composite,

while they show much variation for transversely loaded case. Generally, the two approaches exhibit significant variations if the microstructure experiences higher local field gradients. The predictions obtained using nonlocal approach is found to be more reasonable as it considers the effects of local field gradient near the point of failure.

Among failure criteria, the prediction obtained from maximum shear stress and Tsai-Hill criteria are in an excellent agreement. It is also noticed that the maximum normal stress failure criterion produces conservative predictions compared to all other failure criteria for most of the cases, and yet it lacks of including the interaction effect due to multiaxial stress states. It is also observed that, for continuous fiber-reinforced composites, the axial failure strain is independent of the volume fraction of the fiber for maximum strain failure criterion, while the transverse failure strain significantly varies with volume fraction of the fiber.

The effects of imperfect interface on the elastic properties and failure strength of heterogeneous materials are analyzed using linear traction-displacement interfacial model. The exact solutions of layered composites with imperfect interface are obtained using MSG. The predictions of the exact solution show that interfacial stiffness does not affect longitudinal elastic modulus, all Poisson's ratios and shear modulus G_{12}. However, it significantly affects transverse Young's and shear moduli. The predictions obtained using exact solutions show excellent agreement with the results of 3D FEA obtained by employing periodic boundary conditions. The interfacial analysis of layered composite shows that it is worthwhile to consider the effect of imperfect interface for structural design optimization, wave propagation and multiphysics properties of multifunctional materials.

The predictions of MSG, 3D FEA and Hashin's upper and lower bounds show that imperfect interface considerably affects both elastic effective properties and failure strength of heterogeneous materials. It is also noticed that the predictions

of MSG and 3D FEA show excellent agreement for all examples except that 3D FEA using INTER204 in ANSYS can not sufficiently predict the axial shear modulus. In 3D FEA, the application of external load or displacement boundary condition is mandatory to obtain effective properties, and also the results are obtained by using nonlinear analysis. The excessive external load applications may lead to interpenetration of constituents across the interface which affect the prediction of effective properties [82]. Moreover, for some cases, the output of analyses may not be easily obtained due to convergence problem. These problems are not encountered by using MSG. MSG does not use any external load or displacement boundary condition to predict the effective properties for both perfect and imperfect interface. A simple linear analysis leads to reasonable predictions of both effective properties and initial failure strength of heterogeneous materials.

The progressive damage and fatigue life of heterogeneous materials are analyzed using micromechanics approach. The proposed approaches (DPA and FCA) are incorporated into MSG to estimate the fatigue life and anisotropic damage evolution of the composite. The fatigue life is estimated and found to be good agreement with the experimental data. As the proposed approach is mainly based on micromechanics particularly on the local fields, it requires material properties specific to each constituent. The current prediction may be improved if all materials data are available. The current calibration approach is limited to unidirectional loading option. It is suggested to use non unidirectional laminate together with unidirectional laminate to avoid non-uniqueness of the material constants and also to make it more rigorous.

Among the proposed failure analysis approaches, DPA outperforms all in estimating the failure strength, although the number of material constants required is larger and also difficult to measure or calibrate them. FCA works relatively better for more brittle type of failure where the plasticity is negligible. The advantage of this approach is that it does not require many material constants and they are relatively easily quantifiable using experiments particularly for isotropic material.

Static failure analysis approach, when applied with nonlocal approach, can estimate the load carrying capacity of composite with brittle type failure.

Generally, the current study shows that micromechanics based failure analysis is more rigorous and also provide more reasonable predictions of failure strength and fatigue life of composites. This approach usually takes extended time compared with macromechanical approach. However, SwiftComp can be used to perform the required analysis as accurate as 3D FFA and yet much more efficient.

6. RECOMMENDATIONS

Although failure of homogeneous materials can be better predicted compared with heterogeneous materials, there are still challenges of predicting failure for homogeneous materials. This problem mainly is due to lack of fully developed failure constitutive models. Despite this fact, i.e., lack of fully developed model, most of the failure criteria used for analyzing failure in heterogenous materials are derived from failure model/criteria developed for homogeneous materials. This could potentially be one of the reason that failure are not adequately analyzed for heterogeneous materials. Moreover, as seen from the current study, macromechanical approach cannot rigorously predict failure in heterogeneous materials. This approach fails to consider the stress distribution in the microstructure that plays significant role for predicting failure. It is clear that unless failure is rigorously analyzed for each constituent independently, it is nearly impossible to effectively predict failure in heterogeneous materials. Based on this, it is recommended to perform failure analysis using micromechanics approach.

The idealization of microstructure of heterogeneous materials is a major problem and vital to obtain both the effective properties and failure strength of composite. However, it significantly affects the prediction of failure strength. For instance, continuous fiber-reinforced composite is modeled as a rectangular array with circular fiber in this study. This microstructure is highly idealized to present the actual microstructure of the composite, nevertheless it still provides a reasonable predictions of effective properties. But this does not hold true for prediction of failure or strength. Moreover, randomly generated microstructure is commonly used to analyse effective properties and failure. Although it better simulates the actual microstructure, it still requires a careful generation of microstructure to sufficiently predict failure strength. Moreover, although it is possible to incorporate cracks, voids and inclusion

of all defects including variable interfacial conditions, it is difficult to match with actual coupon. Thus, it is recommended to exhaustively simulate the microstructure as it is an important step toward achieving better predictions of failure strength of heterogeneous materials. Better microstructure can be simulated by effectively predicting manufacturing process. This is the most important step as all the results of the analyses are highly influenced by the microstructure used for predicting any desired parameters.

The other major problem in failure analysis is lack of accurate constitutive model. The first and the most important step is to develop better constitutive model that can sufficiently capture the physics of failure in homogeneous materials. The constitutive model should able to accommodate multiaxial state of local fields. The developed constituent model should be extensively validated with experiment for possible scenarios. After acquiring sufficient knowledge of the constituents, the failure analysis of heterogenous materials can be performed. This approach has a strong potential to provide a more reasonable prediction of failure. The challenge here could be the interfacial conditions which can possibly affect strength predictions, particularly for transversely loaded structures. Thus, the interfacial conditions should also be treated independently.

Failure/fracture is commonly analyzed using fracture mechanics and continuum damage mechanics (CDM). Fracture mechanics requires initial finite crack length, crack distributions, and specific locations. This makes it very subjective to assign the required crack inputs for a given microstructure. This approach is also ineffective, in particular, when applied for heterogenous materials with complex microstructure (for example short fiber composites) where the modes of failure are different from point to point based on the orientations of the fibers. Moreover, it cannot be applied for material with no initial crack. On the other hand, continuum damage mechanics is applicable for virgin material. This approach introduces strain localization and instability in numerical analysis for large damage variable, and it is also observed that energy release rate due to fracture approaches to zero as element size/mesh is refined.

Although nonlocal approach can potentially reduce the effect of the pathological mesh dependence of the results, the problem is still not fully resolved.

Both virgin material point (no crack point) and cracks are inevitable in a given material, thus the combined use of fracture mechanics and continuum damage mechanics is highly recommended to better handle failure in any type of heterogenous material and structures. The way forward is to solve the deficiencies of both fracture mechanics and CDM. The drawbacks of continuum damage mechanics can be partially handled by using nonlocal constitutive modeling. By setting a criterion for crack initiation, the initial crack length and its corresponding orientation are approximated based on the results of anisotropic damage variables obtained from CDM analysis. Then fracture mechanics will come to play to analyze the propagation of crack based on the local dominating modes of failure. The other challenge in CDM is to effectively characterize the damage potentials or damage function. This requires the development of a thermodynamically consistent constitutive model for failure.

The combined approach will create a synergetic effect to achieve the objective, i.e., accurate failure analysis, by employing local-global failure approaches, i.e., multiscale failure approach. For particular type of heterogenous materials, metal-matrix composite, crystal plasticity based failure analysis is recommended to more rigourously analyze failure and damage in heterogeneous materials.

Finally, it is not always easy to apply micromechanics based failure analysis for complex structural components, and it is not also convenient to apply constituent based failure analysis for plate/shell elements. In this case, it is recommended to enhance macromechanical failure analysis model by multiplying a coefficient with the stress ot strain field obtained using macromechanical approach. This coefficient can be estimated based on the orientations of fiber, material properties, fiber volume fraction and loading conditions. This could help to use more reasonable stress or strain field than using the one obtained from macromechanical analysis.

REFERENCES

REFERENCES

[1] F. Paris. A study of failure criteria of fibrous composite materials. *NASA/CR-2001-210661*, National Aeronautics and Space Agency, 2001.

[2] A.S. Kaddour, M.J. Hinton, P.A. Smith, and S. Li. A comparison between the predictive capability of matrix cracking, damage and failure criteria for fibre-reinforced composite laminates: Part A of the third world-wide failure exercise. *Journal of Composite Materials*, 47(20-21):2749–2779, 2013.

[3] P.D. Soden, A.S. Kaddour, and M.J. Hinton. Recommendations for designers and researchers resulting from world-wide failure exercise. *Journal of Composite Materials*, 64:589–604, 2004.

[4] W. Yu, T.O. Williams, B.A. Bednarcyk, J. Aboudi, and T. Tang. A critical evaluation of the predictive capabilities of various advanced micromechanics models. *Proceedings of the 48th Structures, Structural Dynamics and Materials Conference, AIAA SciTech, Honolulu, Hawaii*, April. 23-26 2007.

[5] H. Sertse, L. Zhang, W. Yu, and Z. Ye. A comprehensive evaluation of the predictive capabilities of several advanced micromechanics approaches. *Proceedings of the 48th Structures, Structural Dynamics and Materials Conference, , AIAA SciTech, National Harbor, Maryland*, Jan. 13-17, 2014.

[6] R.M. Christensen. *The Theory of Material Failure*. Oxford, 2013.

[7] J.R. Rice and D.M. Tracy. On ductile enlargement of voids in triaxial stress yields. *Journal of Mechanics and Physics of Solids*, 17:210–217, 1969.

[8] A. Needleman and V. Tvergaard. An analysis of ductile rupture in notched bars. *Journal of Mechanics and Physics of Solids*, 32:461–490, 1969.

[9] A.L. Gurson. Continuum theory of ductile rupture by void nucleation and growth: Part I- yield criteria and flow rules for porous ductile media. *Journal of Engineering Materials and Technology*, 99:2–15, 1977.

[10] V. Tvergaard and A. Needleman. Analysis of the cup-cone fracture in a round tensile bar. *Acta Metallurgica*, 32:157–169, 1984.

[11] J. Lemaitre, R. Desmorat, and M. Sauzay. Anisotropic damage law of evolution. *European Journal of Mechanics - A/Solids*, 19:187–208, 2000.

[12] J. Lemaitre and R. Desmorat. *Engineering Damage Mechanics*. Springer, 2005.

[13] J. Lemaitre. *A Course in Damage Mechanics*. Springer, 1996.

[14] J. Lemaitre and I. Doghri. Damage 90: A post processor for crack initiation. *Journal of Engineering Material and Technology*, 115(2):197–232, 1994.

[15] J. Lemaitre. A continuous damage mechanics model for ductile fracture. *Journal of Engineering Material and Technology*, 107:83–89, 1985.

[16] J. Dufailly and J. Lemaitre. Modeling very low cycle fatigue. *International Journal of Damage Mechanics*, 4(2):153–170, 1995.

[17] I.I. Goldenblat and V.A. Kopnov. Stregnth of glass-reinforced plastic in the complex stress state. *Polymer Mechanics*, 1(2):70–78, 1965.

[18] C.T. Sun and S.E. Yamada. Strength distribution of a unidirectional fiber composites. *Journal of Composite Materials*, 12:169–176, 1978.

[19] B.W. Rosen. Tensile failure of fiberuous composites. *AIAA Journal*, 2(11):185–191, 1964.

[20] J. Duva, J. Aboudi, and C.T. Herakovich. A probabilistic micromechanics model for damaged composites. *Journal of Engineering Materials and Technology*, 118(4):548–553, 1996.

[21] K.K. Chan and M.P Enright. A probabilistic micromechanical code for predicting fatigue life variability: Model development and application. *Journal of Engineering for Gas Turbines and Power*, 128(4):889–895, 2006.

[22] B. N. Cassenti. Probabilistic static failure of composite material. *AIAA Journal*, 22(1):103–110, 1984.

[23] R. Hill. A theory of yeilding and plastic flow of anisotropic metals. *Proceedings of the Royal Society of London: Series A, Mathematical and Physical Sciences, London*, 28:281–288, 1947.

[24] P.A. Boresi and J.R. Schidt. *Advanced Mechanics of Materials*. John Wiley and Sons, 2003.

[25] R. Talreja. Assessment of the fundamentals of failure theories for composite materials. *Composites Science and Technology*, 105:190–201, 2014.

[26] S.W. Tsai and M. Wu. A general theory of strength for ansiotropic materials. *Journal of Composite Materials*, 5:58–80, 1971.

[27] Y. Kwon and J. Berner. Micromechanics model for damage and failure analysis of laminated fibrous composites. *Engineering Fracture Mechanics*, 52(2):231–242, 1995.

[28] J. Mayes and A. Hansen. A comparion of multicontinuum theory based failure simulation with experimental results. *Composite Science and Technology*, 64(2):517–527, 2004.

[29] J.N. Reddy and A.K. Pandey. A first-ply failure analysis of composite laminates. *Computers & Structures*, 25(3):371–393, 1987.

[30] A. Puck and H. Schürmannb. Failure analysis of FRP laminates by means of physically based phenomenological models. *Composites Science and Technology*, 62:1633–1662, 2002.

[31] A. Puck and H. Schürmannb. Failure analysis of FRP laminates by means of physically based phenomenological models. *Composites Science and Technology*, 58:1045–1067, 1998.

[32] Z. Hashin. Failure criteria for unidirectional composite. *Journal of Applied Mechanics*, 47:329–334, 1980.

[33] S.M. Jeng, P. Alassoeur, and J.M. Yang. Fracture mechanisms of fiber-reinforced titanium alloy matrix composites Part IV: Low cycle fatigue. *Materials Sciene and Engineering*, A148:67–77, 1991.

[34] W. Wolfe and T. Butalia. A strain-energy based failure criterion for non-linear analysis of composite laminates subjected to biaxial loading. *Composites Science and Technology*, 58:1107–1124, 1998.

[35] M. Brocca, Z. Bažant, and I.M. Daniel. Microplane model for stiff foams and finite element analysis of sandwich failure by core indentation. *International Journal of Solids and Structures*, 38:8111–8132, 2001.

[36] R. Ali and J. Aboudi. Integrated microplane model with the HFGMC micromechanics for nonlinear analysis of composite materials with evolving damage. *International Journal of Solids and Structures*, 90:129–143, 2016.

[37] K. Kedar, M. Salviato, and Z. Bažant. Microplane triad model for simple and accurate prediction of orthotropic elastic constants of woven fabric composites. *Journal of Composite Materials*, 50(9):1247–1260, 2016.

[38] Z. Bažant and G. Lusio. Nonlocal microplane model with strain-softening yield limits. *International Journal of Solids and Structures*, 41:7209–7240, 2004.

[39] M.D. Sangid. The physics of fatigue crack initiation. *International Journal of Fatigue*, 57:58–72, 2012.

[40] J. Lin, Y. Liu, and T.A. Dean. Comparison of nonlocal approaches in continuum damage mechanics. *International Journal of Damage Mechanics*, 14(4):299–319, 2005.

[41] S. Mortazavian and A. Fatemi. Fatigue behavior and modeling of short fiber reinforced polymer composites: A literature review. *International Journal of Fatigue*, 70:297–321, 2015.

[42] L.J. Hart-Smith. Predictions of generalized maximum-shear-stress failure criterion for certain fiberuous composite lamaintes. *Composites Science and Technology*, 58:1179–1208, 1998.

[43] D.L. McDanels. Analysis of stress-strain, fracture, and ductility behavior of aluminum matrix composites containing discontinuus silicon carbide reinforcement. *Metallurgical Transactions A*, 16:1105–115, 1985.

[44] J.C. Halpin and J.L. Kardos. Strength of discointinuous reinforced composite: I fiber reinforced composite. *Journal of Polymer Engineering and Science*, 18(6):496–504, 1978.

[45] J. Wang, P. Callus, and M. Bannister. Experimental and numerical investigation of the tension and compression strength of un-notched and notched quasi-isotropic laminates. *Composite Structures*, 64(2):297–306, 2004.

[46] M.J. Hinton, A.S. Kaddour, and P.D. Soden. A comparison of the predictive capabilities of current failure theories for composite laminates, judged against experimental evidence. *Composites Science and Technology*, 62:1725–1797, 2002.

[47] P.D. Soden, M.J. Hinton, and A.S. Kaddour. A comparison of the predictive capabilities of current failure theories for composite laminates. *Composites Science and Technology*, 58:1225–1254, 1998.

[48] D.B. Gundel and F.E. Wawner. Experimenal and thoeretical assesment of longutidinal tensial stregnth of unidirectional sic-fiber/titanium matrix. *Composites Science and Technology*, 57(4):471–481, 1997.

[49] B.A. Bednarcyk and S.M. Arnold. Micromechanics based deformation and failure prediction for longitudinally reinforced titanium composites. *Composite Science and Technology*, 61:705–729, 2001.

[50] G.J. Dvorak, M.S. Rao, and J.Q. Tran. Yielding in unidirectional composites under external loads and temperature change. *Journal of Composite Materials*, 7:194–216, 1973.

[51] Z.M. Huang. Micromechanical modeling of fatigue strength of unidirectional fibrous composites. *International Journal of Solids and Structures*, 24:659–670, 2001.

[52] B. N. Cox, M. S. Dadkhah, W. L. Morris, and J. G. Flintoff. Failure mechanisms of 3D woven composites in tension, compression, and bending. *Acta Metallurgica et Materialia*, 42:3967–3984, 2001.

[53] K. Wakashima, Y. Suzuki, and S. Umekawa. A micromechanical prediction of initial yield surfaces of unidirectional composites. *Journal of Composite Materials*, 13:288–302, 1979.

[54] K. Tanaka, K. Wakashima, and T. Moiu. Plastic deformation anisotropy and workhardening of composite materials. *Journal of Mechanics and Physics of Solids*, 21:207–214, 1973.

[55] P.K. Gotsis, C.C. Chamis, and L. Minnetyan. Predictions of composite laminate fracture: micromechanics and progressive fracture. *Composites Science and Technology*, 58:1137–1149, 1998.

[56] M.J. Pindera and J. Aboudi. Micromechanical analysis of yeilding of metal matric composites. *International Journal of Plasticity*, 4:195–214, 1988.

[57] J. Aboudi. Micromechanical prediction of initial and subsequent yield surfaces of metal matrix composites. *International Journal of Plasticity*, 6:471–484, 1990.

[58] D. Scida, Z. Abouraa, M.L. Benzeggagh, and E. Bocherens. A micromechanics model for 3D elasticity and failure of woven-fibre composite materials. *Composites Science and Technology*, 59:505–517, 1999.

[59] J. Choi and K.K. Tamma. Woven fabric composites-Part I: Predictions of homogenized elastic properties and micromechanical damage analysis. *International Journal for Numerical Methods in Engineering*, 50:2285–2298, 2001.

[60] H. Zhu and B.V. Sankar. Evaluation of failure criteria for fiber composites using finite element micromechanics. *Journal of Composite Materials*, 32(8):766–782, 1998.

[61] J.S. Mayes and A.C. Hansenb. Composite laminate failure analysis using multicontinuum theory. *Composites Science and Technology*, 64:379–394, 2004.

[62] M.J. Hinton, A.S. Kaddour, and P.D. Soden, editors. *Failure Criteria in Fibre Reinforced Polymer Composites: The world-wide failure exercise*. Amsterdam, Elsevier Ltd, 2004.

[63] S.P. Engelstad, R.J. Stover, and J.E. Action. Assesment, quantification, and benefits of applying damage tolerance design principles to advanced composite aircraft structure. AFRL-RQ-WP-TR-2015-0068. Lockheed Matrin Aeronautics Company, 2015.

[64] D. Zhang and A. Waas. A micromechanics based multiscale model for nonlinear composites. *Acta Mechanica*, 225(4):1391–1417, 2014.

[65] J.P. Jone and J.S. Whittier. Waves at a flexible bonded interface. *Journal of Applied Mechanics*, 28:103–128, 1967.

[66] J. Aboudi. Damage in composite-modeling of imperfect bonding. *Composite Science and Technology*, 28:103–128, 1987.

[67] H.L. Quang and Q.C. He. Variational principles and bounds for elastic inhomogeneous materials with coherent imperfect interfaces. *Mechanics of Materials*, 40:865–884, 2008.

[68] M.E. Gurtin. A theory of grain boundaries that accounts automatically for grain misorientation and grain-boundary orientation. *Journal of the Mechanics and Physics of Solids*, 56:640–662, 2008.

[69] P.R. Beers, G.J. McShane, V.G. Kouznetsova, and M.G. Geers. Grain boundary interface mechanics in strain gradient crystal plasticity. *Journal of the Mechanics and Physics of Solids*, 61:2659–2679, 2013.

[70] A. Needleman. Micromechanical modelling of intefacial decohesion. *Ultramicroscopy*, 40:203–214, 1992.

[71] X.P. Xu and A. Needleman. Void nucleation by inclusion debonding in a crystal matrix. *Modelling and Simulation in Materials Science and Engineering*, 1:111–132, 1993.

[72] A. Needleman. An analysis of tensile decohesion along an interface. *Journal of the Mechanics and Physics of Solids*, 38(3):289–324, 1990.

[73] C.J. Lissenden. Fiber-matrix interfacial constitutive relations for metal matrix composites. *Journal of Composite: Part B Engineering*, 30:267–278, 1999.

[74] S.H. Warrier, P. Rangaswamy, M.A. Bourke, and S. Krishnamurthy. Assessment of the fiber/ matrix interface bond strength in SiC/Ti-6Al-4V composites. *Journal of Materials Science and Engineering*, 259A:220–227, 1999.

[75] N.J. Pagano and G.P. Tandon. Modeling of imperfect bonding in fiber reinforced brittle matrix composites. *Mechanics of Materials*, 9:49–64, 1990.

[76] Z. Hashin. Thin interphase imperfect interface in elasticity with application to coated fiber composites. *Journal of the Mechanics and Physics of Solids*, 36(6):2509–2537, 1991.

[77] Z. Hashin. Thermoelastic properties of particulate composites with imperfect interface. *Journal of the Mechanics and Physics of Solids*, 36(6):745–762, 1991.

[78] I.V. Andrianova, V. Bolshakovb, V.V. Danishevs, and D. Weichert. Asymptotic simulation of imperfect bonding in periodic fibre-reinforced composite materials under axial shear. *International Journal of Mechanical Sciences*, 49:1344–1354, 2007.

[79] H.T. Liu and L.Z. Sun. An interfacial debonding model for particle-reinforced composites. *International Journal of Damage Mechanics*, 13(2):163–185, 2004.

[80] V. Tvergaard. Fiber debonding and breakage in a whisker-reinforced metal. *Journal of Material Science and Engineering*, 190A:215–222, 1995.

[81] F. Lene and D. Leguillon. Homogenized constitutive law for a partially cohesive composite material. *International Journal of Solids and Structures*, 18(5):443–458, 1982.

[82] A. Caporale, R. Luciano, and E. Sacco. Micromechanical analysis of interfacial debonding in unidirectional fiber-reinforced composites. *Computers & Structures*, 84:2200–2211, 2006.

[83] N. Bonora and A. Ruggiero. Micromechanical modeling of composites with mechanical interface Part II: Damage mechanics assessment. *Composites Science and Technology*, 9:49–64, 1990.

[84] P. Ladeveze. A damage computational approach for composites: Basic aspects and micromechanical relations. *Computational Mechanics*, 17:142–150, 1995.

[85] P. Ladeveze, O. Allix, J.F. Deü, and D. Lévêque. A mesomodel for localisation and damage computation in laminates. *Computer Methods in Applied Mechanics and Engineering*, 183:105–112, 2000.

[86] P. Ladeveze and L. Dantec. Damage modelling of the elementary ply for laminated composites. *Composites Science and Technology*, 43:257–267, 1992.

[87] O. Allix, P. Ladeveze, and A. Corigliano. Damage analysis of interlaminar fracture specimens. *Composite Structures*, 61-74:31, 1995.

[88] A. Turon, J. Costa, P. P. Maimi, D. Trias, and J.A. Mayugo. A progressive damage model for unidirectional fibre-reinforced composites based on fibre fragmentation. Part I: Formulation. *Composites Science and Technology*, 65:2039–2048, 2005.

[89] J. Costa, A. Turon, P. P. Maimi, D. Trias, and J.A. Mayugo. A progressive damage model for unidirectional fibre-reinforced composites based on fibre fragmentation. Part II: Stiffness reduction in environment sensitive fibres under fatigue. *Composites Science and Technology*, 65:22692275, 2005.

[90] T.E. Tay, S.H. Tan, V.B. Tan, and J.H. Gosse. Damage progression by the element-failure method (EFM) and strain invariant failure theory (SIFT). *Composites Science and Technology*, 65:935–944, 2005.

[91] H. Kang, Z. Shan, Zang. Y., and F. Liu. Progressive damage analysis and strength properties of fiber-bar composites reinforced by three-dimensional weaving under uniaxial tension. *Composite Structures*, 141:264–281, 2016.

[92] S. Suresh. *Fatigue of Materials*. Cambridge University Press, 1998.

[93] A.F. Grandt. *Fundamentals of Structural Integrity: Damage Tolerant Design and Nondestructive Evaluation*. John Wiley and Sons, 2004.

[94] A. Farahani, H. Haftchenari, and M. Panbechi. An energy-based fatigue damage parameter for off-axis unidirectional FRP composites. *Composites & Structures*, 79:381–389, 2007.

[95] H. Jahed, A. Farahani, M. Noban, and I. Khalaji. An energy-based fatigue life assessment model for various metallic materials under proportional and non-proportional loading conditions. *International Journal of Fatigue*, 29:647–655, 2007.

[96] J. Degrieck and W.V. Paepegem. Fatigue damage modelling of fiber reinforced composite materials: Review. *Applied Mechanics Reviews*, 54(4):279–300, 2001.

[97] A. Fatemi and L. Yang. Cumulative fatigue damage and life prediction theories: A survey of the state of the art for homogeneous materials. *International Journal of Fatigue*, 20:9–34, 1998.

[98] M. Kawai. A phenomenological model for off-axis fatigue behavior of unidirectional polymer matrix composites under different stress ratios. *Composites: Part A*, 35:955–963, 2004.

[99] J.L. Chaboche and J.F. Maire. A new micromechanics based CDM model and its application to CMCs. *Aerospace Science and Technology*, 6:131–145, 2002.

[100] P. Maimi, P.P. Camanho, J.A. Mayugo, and C.G. Davila. A continuum damage model for composite laminates: Part I constitutive model. *Mechanics of Materials*, 39:897–908, 2007.

[101] P. Maimi, P.P. Camanho, J.A. Mayugo, and C.G. Davila. A continuum damage model for composite laminates: Part II computational implementation and validation. *Mechanics of Materials*, 39:909–919, 2007.

[102] H. Mao and S. Mahadevan. Fatigue damage modelling of composite materials. *Composite Structures*, 58:405–410, 2002.

[103] J.A. Mohandesi and B. Majidi. Fatigue damage accumulation in carbon/epoxy laminated composites. *Materials and Design*, 30:1950–1956, 2009.

[104] E.J. Barbero, G.F. Abdelal, and A. Caceres. A micromechanics approach for damage modeling of polymer matrix composites. *Composite Structures*, 67:413–422, 2004.

[105] G.F. Abdelal, A. Caceres, and E.J. Barbero. A micro-mechanics damage approach for fatigue of composite materials. *Composite Structures*, 56:413–422, 2002.

[106] G.Z. Voyiadjis and B. Deliktas. A coupled anisotropic damage model for inelastic response of composite materials. *Computer Methods in Applied Mechanics and Engineering*, 183:159–199, 2000.

[107] J.F. Maire and J.L. Chaboche. A new formulation of continuum damage mechanics (CDM) for composite materials. *Aerospace Science and Technology*, 4(4-5):247–257, 1997.

[108] J. Fish and C. Oskay. A nonlocal multiscale fatigue model. *Mechanics of Advanced Materials and Structures*, 12:485–500, 2005.

[109] J.L. Chaboche, S. Kruch, J.F. Maire, and T. Pottier. Towards a micromechanics based ineleastic and damage modeling of composites. *Internaltional Journal of Plasticity*, 17:411–439, 2001.

[110] A. Pirondi and N. Bonora. Modeling ductile damage under fully reversed cycling. *Internaltional Journal of Plasticity*, 17:411–439, 2001.

[111] J.H. Pang, B.C. Xiong, and T.H. Low. Low cycle fatigue models for lead-free solders. *Internaltional Journal of Plasticity*, 17:411–439, 2001.

[112] S.K. Koh, S.J. Oh, C. Li, and F. Ellyin. Low-cycle fatigue life of SiC-particulate-reinforced Al-Si cast alloy composites with tensile mean strain effects. *International Journal of Fatigue*, 21:1019–1032, 1999.

[113] T.S. Srivatsan. The low-cycle fatigue behaviour of an Aluminium-Alloy-Ceramic-particle composite. *International Journal of Fatigue*, 3:173–182, 1992.

[114] V.M. Harik, J.R. Klinger, and T.A. Bogetti. Low-cycle fatigue of unidirectional composites: Bi-linear SN curves. *International Journal of Fatigue*, 24:455–462, 2002.

[115] Y.C. Xiao, S. Li, and Z . Gao. A continuum damage mechanics model for high cycle fatigue. *Smart Materials and Structures*, 20:503–508, 1998.

[116] M. Paas, P.J. Schreurs, and W.A. Brekelmans. A continuum approach to brittle and fatigue damage: Theory and numerical procedures. *International Journal of Solids and Structures*, 30:579–599, 1993.

[117] S. Murakami and K. Kamiya. Constitutive and damage evolution equations of elastic-brittle materials based on irreversible thermodynamics. *International Journal of Mechanical Sciences*, 39(4):473–486, 1996.

[118] J. Lemaiter, J.P. Sermage, and R. Desmorat. A two scale damage concept applied to fatigue. *International Journal of Fracture*, 97:67–81, 1999.

[119] R. Desmorat, A. Kane, M. Seyedi, and J.P. Sermage. Two scale damage model and related numerical issues for thermo-mechanical high cycle fatigue. *European Journal of Mechanics A/Solids*, 26:909–935, 2007.

[120] C. Doudard, S. Calloch, A. Cugy, A . Galtier, and F. Hild. A probabilistic two-scale model for high-cycle fatigue life predictions. *Fatigue and Fracture of Engineering Materials and Structures*, 28(3):279288, 2005.

[121] R. Desmorat, F. Pauget, J. Aboudi, and J.P. Sermage, editors. *Damage-2005: A Post-Processor for High Cycle Fatigue Undex Complex Thermomechanical Loading*. ASME Pressure Vessels and Piping Division Conference, July 23-27 2006.

[122] T.K O′Brien and K.L. Reifsnider. Fatigue damage: Stiffness/strength comparisons for composite materials. *Journal of Testing and Evaluation*, 5:384–393, 1977.

[123] H.A. Whitworth. Evaluation of the residual strength degradation in composite laminates under fatigue loading. *Composite Structures*, 48:261–364, 2000.

[124] J.M. Appuhamy, T. Kaita, M. Ohga, and K. Fujii. Prediction of residual strength of corroded tensile steel plates. *International Journal of Steel Structures*, 11(11):65–79, 2011.

[125] J.N. Yang and M.D. Liu. Residual strength degradation model and theory of periodic proof tests for graphite/epoxy laminates. *Composite Materials*, 11:176–203, 1976.

[126] L.M. Kachanov. On rupture time under condition of creep. *Izvestia Akademi Nauk SSSR*, 8(8):26–31, 1958.

[127] J.W. Ju. On energy-based coupled elastoplastic damage theories: Constitutive modeling and computational aspects. *International Journal of Solids and Structures*, 25(7):803–833, 1989.

[128] A. Cauvin and R.B. Testa. Damage mechanics: Basic variables in continuum theories. *International Journal of Solids and Structures*, 36:747–761, 1999.

[129] M. Sumio. *Continuum Damage Mechanics: A Continuum Mechanics Approach to the Analysis of Damage and Fracture*. Springer, 2012.

[130] J.H. Vree, W.A. Brekelmans, and M.A. Gils. Comparison of nonlocal approaches in continuum damage mechanics. *Computers & Strucutres*, 45(4):581–588, 1995.

[131] R.D. Borst, L.J. Sluys, H.B. Muhlhaus, and A.J. Pamin. Fundamental issues in finite element analyses of localization of deformation. *Engineering Computations*, 26(1):43–62, 1997.

[132] P. Pegon and A. Anthoine. Numerical strategies for solving continuum damage problems with softening: Application to the homogenization of masonry. *Computers & Structcures*, 64(1-4):623–642, 1997.

[133] Z. Bažant. Why continuum damage is nonlocal: Micromechanics arguments. *Journal of Engineering Mechanics*, 117(5):1070–1087, 1991.

[134] Z. Bažant and G. Pijaudier-Cabot. Nonlocal continuum damage, localization instability and convergence. *Journal of Applied Mechanics*, 55(2):287–293, 1988.

[135] R.H. Peerlings, R.D. Borst, W.A. Bekelmans, and J.H. De Vree. Gradient enhanced damage for quasi-brittle materials. *International Journal for Numerical Methods in Engineering*, 39:3391– 3403, 1996.

[136] R. Masson, W.A. Bekelmans, R.D. Borst, and M.G. Geers. Gradient enhanced damage for quasi-brittle materials. *International Journal for Numerical Methods in Engineering*, 49:1547–1569, 2000.

[137] Y. Liu, V. Filonova, N. Hu, Z. Yuan, J. Fish, Z. Yuan, and T. Belytschko. A regularized phenomenological multiscale damage model. *International Journal for Numerical Methods in Engineering*, 99:867–887, 2014.

[138] T. Tang and W. Yu. A variational asymptotic micromechanics model for predicting conductivity of composite materials. *Journal of Mechanics of Materials and Structures*, 2:1813–1830, 2007.

[139] R. Hill. Elastic properties of reinforced solids: some theoretical principles. *Journal of the Mechanics and Physics of Solids*, 11:357–372, 1963.

[140] J. Aboudi. Elastoplasticity theory for composite materials. *Solid Mechanics Archives*, 11:141–183, 1986.

[141] J. Aboudi. Micromechanical analysis of composites by the method of cells. *Applied Mechanics Reviews*, 42:193–221, 1989.

[142] J. Adoudi. The generalized method of cells and high-fidelity generalized method of cells micromechanical models-a review. *Mechanics of Advanced Materials and Structures*, 11(4-5):329–366, 2004.

[143] H. Sertse, J. Goodsell, J. Ritchey, and and Yu W. Pipes, R. Challenge problems for the benchmarking of micromechanics analysis: Level I initial results. *Journal of Composite Materials*, (DOI: 10.1177/0021998317702437, 2017.

[144] C.L. Tucker and E. Liang. Stiffness predictions for unidirectional short-fiber composites: Review and evaluation. *Composites Science and Technology*, 59:655–671, 1999.

[145] J. Besson, G. Cailletaud, J.L. Chaboche, and S. Forest. *Non-Linear Mechanics of Materials, Solid Mechanics and Its Applications*, volume 167. Springer, 2012.

[146] K. Hayakawa, S. Murakami, and Y. Liu. An irreversible thermodynamic theory for elastic-plastic damage materials. *European Journal of Mechanics-A/Solids*, 17(2):13–32, 1998.

[147] Z. Hashin. Extremum principles for elastic heterogeneous media with imperfect interfaces and their application to bounding of effective moduli. *Journal of the Mechanics and Physics of Solids*, 40(4):767–781, 1991.

[148] W. Yu and T. Tang. A variational asymptotic micromechanics model for predicting thermoelastic properties of heterogeneous materials. *International Journal of Solids and Structures*, 44(22-23):7510–7525, 2007.

[149] W. Yu. An exact solution for micromechanical analysis of periodically layered composites. *Mechanics Research Communications*, 46:71–75, 2012.

[150] W. Yu. A variational-asymptotic cell method for periodically heterogeneous materials. In *2005 ASME International Mechanical Engineering Congress and Exposition, Orlando, Florida.*, Nov. 5-11 2005.

[151] W. Yu. A unified theory for constitutive modeling of composites. *Journal of Mechanics of Materials and Structures*, 11(4):379411, 2016.

[152] W. Yu. Structure genome: Fill the gap between materials genome and structural analysis. *Proceedings of the 56th Structures, Structural Dynamics and Materials Conference, AIAA SciTech, Kissimmee, Florida*, Jan. 5-9 , 2015.

[153] W. Yu. A variational-asymptotic cell method for periodically heterogeneous materials. *Proceedings of the 2005 ASME International Mechanical Engineering Congress and Exposition, Orlando, Florida.*, pages 5–11, 2005.

[154] T. Mori and T. Tanaka. Average stress in matrix and average elastic energy of materials with misfitting inclusions. *Acta Metallurgica*, 21(5):571–574, 1973.

[155] S. Nemat-Nasser and M. Hori. *Micromechanics: Overall Properties of Heterogeneous Solids*. Elsevier Science, 1993.

[156] J. Aboudi, S.M. Arnold, and B.A. Bednarcyk. *Micromechanics of Composite Materials: a generalized multiscale analysis approach*. Butterworth-Heinemann, 2012.

[157] B.A. Bednarcyk and S.M. Arnold. *MAC/GMC 4.0 Users Manual: Keywords Manual, TM 2002-212077*. NASA, 2002.

[158] D.F Adams and D.A Crane. Combined loading of micromechanical analysis of unidirectional composite. *Composites*, 15:181–192, 1984.

[159] D. Pahr and S.M. Arnold. The applicability of the generalized method of cells for analyzing discontinuously reinforced composite. *International Journal of Solids and Structures*, 33:153–170, 2002.

[160] H. Sertse and W. Yu. Three-dimensional effective properties of layered composites with imperfect interfaces. *Advances in Aircraft and Spacecraft Science*, 4(6):613–624, 2017.

[161] Z. Hashin and A. Rotem. A fatigue failure criterion for fiber reinforced materials. *Journal of Composite Material*, 7:448–464, 1973.

[162] Z. Huang. Micromechanical prediction of ultimate strength of transversely isotropic fibrous composite. *International Journal of Solids and Structures*, 38:4147–4172, 2001.